UNIVERSITY OF LJUBLJANA
Faculty of Mechanical Engineering

in association with

TECHNISCHE
UNIVERSITÄT
WIEN

Finite Element Method Simulations of the Delamination in Laminated Composite Structures

A Master's thesis of the second-cycle master's study programme in MECHANICAL ENGINEERING – a research and development programme

Tilen Ceglar

Advisor: Assist. Prof. Dr. Miha Brojan,
Co-adviser: Associate Prof. Dr. Heinz Pettermann, TU Wien

Ljubljana, February 2017

Acknowledgements

First and foremost I would like to thank Professor Heinz Pettermann and the Institute of Lightweight Design and Structural Biomechanics, TU Wien, for giving me the opportunity to expand my knowledge in composite materials outside the frame of my home University. Besides him, without the help and support of Dr. Martin Schwab I would not have finished this work. For that I'm very thankful to him. This also goes to the rest of the ILSB team. Additionally, Professor Pettermann enabled me new challenges in my life, for which I'm very honoured and grateful.

I would also like to thank Professor Miha Brojan for all of the support and guidance during this time.

Last but not least, I have to thank my family and my partner Manca for all of their support and motivation.

Declaration

1. I, the undersigned Tilen Ceglar, born 25 April 1990 in Trbovlje, a student at the Faculty of Mechanical Engineering at the University of Ljubljana, hereby declare that this final master's thesis titled Finite Element Method Simulations of the Delamination in Laminated Composite Structures is my own original work created under the supervision of my advisor Assist. Prof. PhD. Miha Brojan and co-adviser Associate Prof. PhD. Heinz Pettermann.

2. I hereby declare that the submitted electronic copy of this master's thesis is identical to the printed copy.

3. Pursuant to the provisions of the Copyright and Related Rights Act (Official Gazette of the Republic of Slovenia, No. 21/1995 as amended), I hereby expressly give my permission for this master's thesis to be published on the websites of the Faculty of Mechanical Engineering and the University of Ljubljana.

4. By signing this Declaration, I grant my permission for this master's thesis to be made publicly accessible on-line via the Repository of the University of Ljubljana.

By signing this document, I certify that:

- the presented text is the product of my own original research in its entirety;
- the presented text adheres to linguistic and stylistic conventions and the technical requirements of the Guidelines for Composing Final Theses, meaning that:
  - the works and opinions of other authors used in this master's thesis are appropriately cited or acknowledged pursuant to the Guidelines for Composing Final Theses, and
  - I have obtained the permission for the use of any data and original work reproduced in the text in full (either as text or as a graphic) from their respective authors and duly noted that in the text itself;
- I am aware that plagiarism, i.e. the misrepresentation of someone else's work (be it text or graphics) as my own, is a crime under the Criminal Code of the Republic of Slovenia (Official Gazette of the Republic of Slovenia, No. 55/2008 as amended);
- I am aware of the potential repercussions concerning my status at the Faculty of Mechanical Engineering at the University of Ljubljana as per the applicable Rules should plagiarism be proven in connection to the submitted master's thesis.

Ljubljana, 15.2.2017 Signature of the author: ____________________

Abstract

UDC [ ]
No.: MAG II/324

Finite Element Method Simulations of the Delamination in Laminated Composite Structures

Tilen Ceglar

Key words: Finite Element Method
laminated composite structure
delamination
embedding approach
cohesive zone
shell elements

Finite Element Method (FEM) simulations of the delamination in fabric laminates with complex topology require considerable computational power, in particular when material and interface nonlinearities are taken into account. A multi-scale embedding approach is presented which is capable to capture the nonlinear mechanisms inside textile plies while the computational effort is kept relative low. The approach is used to simulate the response of Double Cantilever Beam (DCB) tests and three point End Notch Flexure (ENF) tests. Delamination is evaluated in terms of nonlinear load displacement curves, critical energy release rates and dissipated energy. Besides the global response, local effects are investigated and the localized patterns of the various nonlinear mechanisms are predicted. This way, detailed insight to the global delamination behaviour as well as the locally involved mechanics is obtained quantitatively.

Izvleček

UDK [ ]

Tek. štev.: MAG II/324

Simulacije delaminacije v laminiranih kompozitnih strukturah z metodo končnih elementov

Tilen Ceglar

Ključne besede:
metoda končnih elementov
laminirana kompozitna struktura
delaminacija
integracija podstrukture
kohezivna cona
lupinski končni elementi

Simuliranje delaminacije z metodo končnih elementov v laminiranih pletenih kompozitih z podrobno topologijo, še posebaj kadar simulacija vsebuje nelinearne materialne modele, zahteva precejšno računsko moč. Predlagana rešitev temelji na integraciji podrobne pletene kompozitne strukture v bolj osnovni model. Takšen pristop omogoča opis nelinearnih procesov znotraj podstrukture med simulacijo standardnih testov za delaminacijo, pri tem pa računski napor ostaja razmeroma nizek. Delaminacija je ovrednotena s krivuljo razmerja med obremenitvijo in deformacijo, sproščanjem energije ter disipacijsko energijo pri simulirani poškodbi znoraj numeričnega modela. Poleg globalnega odziva so predvideni tudi lokalni pojavi, ki so rezultat lokaliziranih nelinearnih mehanizmov znotraj kompozitne podstrukture. Na ta način pridobimo podroben vpogled v delaminacijo tako na globalni ravni kot znotraj pletene strukture laminata.

Table of Contents

List of Figures xv

List of Tables xvii

List of symbols used xix

List of acronyms used xxi

1 Introduction 1

1.1 Background 1

1.1.1 Laminated Composite Structures 2

1.1.2 Failure Modes of Laminated Composite 3

1.2 Scope of the Present Work 3

1.3 Literature Overview 5

2 Delamination in Laminated Composite Structures 7

2.1 Mode I Delamination 11

2.2 Mode II Delamination 15

3 Modelling Approach 19

3.1 Ply Modelling 20

3.1.1 Shell Composite Section in ABAQUS 20

3.1.2 Ply Interaction 21

3.2 Interface Modelling 22

3.2.1 Cohesive Zone Method 23

3.3 Embedded Domain Coupling 26

4 Laminate Geometry, Properties and Numerical Models 29

4.1 Reference Model 30

4.1.1 Material Properties 30

4.1.2 Mesh Definition 30

4.1.3 Section Definition 31

4.1.4 Boundary and Loading Conditions 32

4.2 Models with an embedded textile domain 35

4.2.1 ILSB Textile Unit Cell 35
4.2.2 Material Properties 38
4.2.3 Model Input Structure 38
4.2.4 Model Assembly and Mesh Definition 39
4.3 Analysis Control 44

5 Computational Results 45

5.1 Double Cantilever Beam Simulations 45
5.1.1 Crack Front Propagation Evaluation 46
5.1.2 Fracture Resistance Curve (R-Curve) 53
5.1.3 Energy Balance Analysis 54
5.2 Three Point End Notched Flexure Simulations 57
5.2.1 Crack Front Propagation Evaluation 58
5.2.1.1 EMB2 model 59
5.2.1.2 EMB4 model 62
5.2.2 Fracture Resistance Curve (R-Curve) 66
5.2.3 Energy Balance Analysis 67

6 Conclusions 73

7 Bibliography 75

8 Annex A 79

8.1 Energy Release Rate $\mathcal{G}_\mathrm{I}$ Evaluation 79

List of Figures

Figure 1.1: Evolution of composite application at Airbus [1]. 2

Figure 2.1: Three modes of fracture 8

Figure 2.2: Experimental setup for mode I Double Cantilever Beam (DCB) test. [2, 3] 8

Figure 2.3: Experimental setup for mode II 3 point End Notched Flexure (ENF) test. [2, 4] 8

Figure 2.4: Load-displacement dependency during crack propagation 9

Figure 2.5: Delamination model in laminated composite. [2] 10

Figure 2.6: Double Cantilever Beam test method. 12

Figure 2.7: Analytical load displacement curve for DCB test 13

Figure 2.8: Crack length in relation to tip displacement for the DCB test. . . 14

Figure 2.9: Fracture resistance curve (R-curve) for mode I delamination. . . . 14

Figure 2.10: Three point End Notch Flexure test method. 15

Figure 2.11: Analytical load-displacement curve for the 3 point ENF test. . . . 17

Figure 2.12: Crack length in relation to central displacement for 3 point ENF test. 17

Figure 3.1: Modelling approach in laminated composites. 19

Figure 3.2: Hard contact and penalty method 21

Figure 3.3: Cohesive element attached with two shells elements 23

Figure 3.4: Bi-linear traction-separation law. 24

Figure 3.5: Bi-linear mixed-mode traction-separation law. [5] 25

Figure 3.6: Surface based tie constrains 27

Figure 4.1: Model baseline geometry. 29

Figure 4.2: Mesh discretization of the reference model. 32

Figure 4.3: Shell composite section in Abaqus with three layers of homogenized textile composite material. 32

Figure 4.4: DCB homogenized model with geometry, boundary and loading conditions. 33

Figure 4.5: ENF homogenized model with geometry, boundary and loading conditions. 34

Figure 4.6: Symmetry boundary conditions at the reference model 34

Figure 4.7: Cross section of a 2/2 twill weave indicating the shell reference planes, shell offset, and shell thickness. 36

Figure 4.8: Cross section of a 2/2 twill weave indicating tie constrains between the matrix and tows. 36

Figure 4.9: Cross section of the 2/2 twill weave showing the piecewise linear ondulation path and rectangular tow cross sections. 37

Figure 4.10: Shell element based unit cell assembled and disassembled into tow reference planes and matrix reference planes. 37

Figure 4.11: Inter-tow cohesive elements for 2/2 twill weave unit cell. 37

Figure 4.12: Abaqus master input file structure of the models with an embedded domain. 39

Figure 4.13: Double Cantilever Beam embedded domain model geometry, boundary and loading conditions (not to scale). 40

Figure 4.14: Three point End Notch Flexure embedded domain model geometry, boundary and loading conditions (not to scale). 40

Figure 4.15: Cross section of a EMB2 and EMB4 model showing the shell reference plane layout and their thicknesses. 42

Figure 4.16: Upper half of the cross section of a EMB4 model showing the embedding approach. 42

Figure 4.17: Mesh discretization of the EMB2 model. 43

Figure 5.1: Load-displacement curves for the DCB simulation. 46

Figure 5.2: Damage criterion for the reference model in the DCB simulation. 47

Figure 5.3: Load versus crack length relation in the DCB simulation. 48

Figure 5.4: Crack propagation in relation to the tip displacement in the DCB simulation. 48

Figure 5.5: Area definition in the EMB2 model. 49

Figure 5.6: Delamination progress during the DCB simulation in the interface of the EMB2 model. 50

Figure 5.7: Mode mix ratio during the delamination in DCB simulation of the EMB2 model. 52

Figure 5.8: Fracture resistance curve (R-curve) for mode I delamination. . . . 53

Figure 5.9: Energy balance of the DCB simulation for the EMB2 model. . . . 55

Figure 5.10: Comparison between the damage dissipation energy from the EMB2 model and the damage dissipation energy evaluated by experimental data reduction techniques in the DCB simulation. 56

Figure 5.11: Load-displacement curves for the ENF simulation. 57

Figure 5.12: Load versus crack length relation in mode II delamination for the reference, EMB2 and EMB4 model. 58

Figure 5.13: Crack propagation in relation to central displacement for mode II delamination. The reference, EMB2 and EMB4 models are compared. 59

Figure 5.14: Delamination sequence during the ENF simulation in the interface of the EMB2 model. 60

Figure 5.15: Mode mix ratio in the ENF simulation of the EMB2 model 61

Figure 5.16: Delamination progress during the ENF simulation in the middle interface of the EMB4 model. 63

Figure 5.17: Damage initiation and evolution in the bottom and top interface at central displacement $\delta_{\mathrm{II}} = 17.07\,mm$ of the EMB4 model. . . . 65

Figure 5.18: Fracture resistance curves (R-curves) for mode II delamination. . 66

Figure 5.19: Energy balance of the EMB2 model during the mode II simulation. 68

Figure 5.20: Energy balance of the EMB4 model during the mode II simulation. 69

Figure 5.21: Comparison between the damage dissipation energy from the EMB2 model and the damage dissipation energy evaluated by corrected beam theory in the ENF simulation. 70

Figure 5.22: Comparison between the damage dissipation energy from the EMB4 model and the damage dissipation energy evaluated by corrected beam theory in the ENF simulation. 70

Figure 5.23: Comparison between the damage dissipation energy output variable and the dissipation energy evaluated with the CBT for the EMB2 and EMB4 model in the ENF simulation. 71

Figure 8.1: Continuous area method for crack growth fracture curve [6] 80

Figure 8.2: Comparison of energy release rate evaluation approaches for mode I of model with a 2 layer embedded domain. 81

List of Tables

Table 4.1: Material properties of homogenized carbon/epoxy 2 × 2 twill weave composite material. 30

Table 4.2: Material properties of carbon/epoxy 2x2 twill weave composite material 38

Table 4.3: Mesh size comparison - ENF simulation 41

List of symbols used

Symbol	Unit	Meaning
a	mm	crack length
B	mm	width
C	MPa^{-1}	compliance
E	MPa	Young's modulus
G	MPa	shear modulus
$\mathcal{G}$	$\mathrm{N\,mm}^{-1}$	strain energy release rate
h	mm	height
I	mm^4	second moment of area
l	mm	specimen length
L	mm	length
K	$\mathrm{N/mm}^3$	stiffness
M	$N\,mm$	moment
N	/	number
P	N	reaction force
U	mJ	energy
u	/	translational degree of freedom
t	MPa	traction
α	/	mixmode parameter
Γ	/	correction factor
δ	mm	displacement
η	/	cohesive parameter
ξ	/	width ratio
σ	MPa	stress
υ	/	Poisson's ratio
ϕ	/	rotational degree of freedom
χ	/	correction factor

Indices	Meaning
0	initial value
c	critical value
e	external
el	element
f	failure
i	internal
m	mixmode
max	maximum value
n	normal
p	propagation

s	shear traction component 1
S	total shear traction component
t	shear traction component 2
T	total traction component

List of acronyms used

Acronym	Meaning
I	mode I fracture
II	mode II fracture
III	mode III fracture
ALLCD	creep dissipation energy output
ALLDMD	damage dissipation energy output
ALLSE	internal strain energy output
ALLWK	external work
CBT	corrected beam theory
CZ	cohesive zone
EMB2	two layer embedded domain model
EMB4	four layer embedded domain model
SDEG	stiffness degradation
MMIXDME	mixmode damage evolution criterion
MMIXDMI	mixmode damage initiation criterion
QUADSCRT	quadratic nominal stress criterion

1 Introduction

1.1 Background

Nowadays, lightweight structures are being widely used not only in aerospace, but also in industries such as automotive, sports and others due to their weight saving potential and accessible price. Laminated composite structures are the most common choice when high stiffness-to-weight and strength-to-weight ratios are pursued. The development of composite materials in terms of design, manufacturing and numerical modelling has been on the rise for the past couple of decades to meet the demands of the industries.

Composite materials represent superior alternative to more conventional materials, such as steel or aluminum, in application where light weight combined with load carrying capacity is the main criterion. Additionally, composite materials can be tailored to specific load scenarios in terms of their mechanical behaviour, making them even more efficient and useful in lightweight structures. However, their downside is a significantly higher price compared to conventional metals. It is clear to see, why composite materials are being widely used in aerospace industry. Due to fuel efficiency of commercial flights, the share of composite materials in total airplane structural weight is exceeding 50% in the newest generation of civil aeroplanes, which is quite remarkable considering their total dry weight (several hundred tons). An evolution of composite application at Airbus is illustrated on Fig. 1.1 showing a progressive composite application in civil airplanes throughout the past years.

The full potential of composite materials is yet to be exploited. A key aspect of it is predicting their mechanical behaviour under various load cases. In order to do so, it is necessary to develop new modelling approaches and computational methods. This is where the motivation for this thesis comes from. Numerical simulations of the mechanical response of laminated composite structures with detailed topology, performed for the purposes of this work, are aiming to contribute in further development of such structures. For this reason, a modelling approach with embedded domains of detailed composite structures is presented in the following chapters, but first some basics of composite structures are covered.

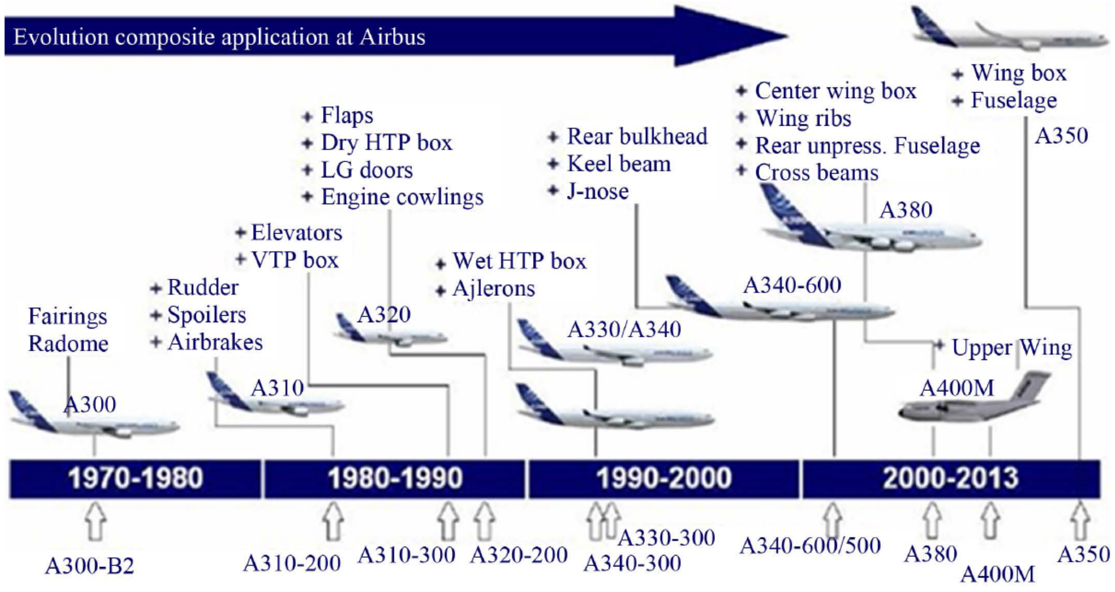
Evolution composite application at Airbus
Fairings
Radome
A300
Rudder
Spoilers
Airbrakes
A310
Elevators
VTP box
Flaps
Dry HTP box
LG doors
Engine cowlings
A320
Wet HTP box
Ajlerons
Rear bulkhead
Keel beam
J-nose
A330/A340
A340-600
Center wing box
Wing ribs
Rear unpress. Fuselage
Cross beams
A380
Wing box
Fuselage
A350
Upper Wing
A400M
1970-1980
1980-1990
1990-2000
2000-2013
A300-B2
A310-200
A310-300
A320-200
A330-300
A340-300
A340-600/500
A380
A400M
A350

Figure 1.1: Evolution of composite application at Airbus [1].

1.1.1 Laminated Composite Structures

In general, a composite material consist of two or more components (also called phases), with different material properties, combined in such a way that they have better engineering properties for a specific load case than conventional materials.

The most common composite materials are fibre reinforced polymers (FRP). They consist of two phases. One is called the reinforcing phase and the one in which it is embedded in is called the matrix phase. The reinforcing phase material may be in the form of particles, flakes or continuous fibres, which can be uni-directional (UD), braided, woven or knitted. Common fibre materials used in composites are glass, carbon and aramid fibres, while for the matrix, polymers such as epoxy and polyester are normally found in composites. Matrix, which has good adhesive properties and brittle crack behaviour, is reinforced with fibres, which have higher strength and stiffness compared to it.

Structures made of composite material, e.g. carbon fibre/epoxy, are usually formed by layered laminates, that consist of multiple layers bonded together as a laminate. A single layer is called a ply or lamina and the number of layers and their orientation governs the laminate's response on external loads. The laminate's strength and stiffness can be tailored to a specific load scenario by configuring the number and orientation of plies, which additionally sets it apart from conventional materials.

While the characteristics of UD laminated composites have been investigated in greater detail, which in recent years also led to standardization of several test methods for their behaviour, fabric or woven composites have not been researched yet in the same scale due to its more complex structure. The aim of this thesis is to investigate laminated woven or textile composite structures to one of the most common failure modes in composites, named delamination, which characterizes interlaminar damage when two adjacent layers of a laminate separate, resulting in crack propagation in the structure.

1.1.2 Failure Modes of Laminated Composite

There are two main failure mechanisms in laminated composites, one being the failure of the plies themselves, which can be caused by the failure of fibre, matrix or fibre/matrix interface, and the other is the failure of interface between adjacent plies, which is governed by matrix failure but it is still affected by the fibre topology in plies.

Composite laminates containing layers of UD fibres have excellent in-plane properties but suffer from interlaminar characteristics as there is no reinforcement through the thickness of the laminate. Such structures have a low impact resistance and are prone to delaminations. This can be improved by placing woven or braided fabrics in plies instead of UD ones. The interwoven topology improves the fracture toughness, the damage tolerance and the through-the-thickness properties [7], although they do not include any reinforcement in the thickness direction. However, the in-plane stiffness and strength of the textile laminates is lower compared to the laminates comprising UD plies only [8].

In any case, delamination or interlaminar damage is a predominant failure mode in all laminated composites without any reinforcement in the thickness direction [2, 9–12]. It occurs as a separation of ply layer or groups of layers from the adjacent ones, thus acting as a crack propagation mechanism and resulting in significant reduction in transverse shear stiffness and mainly compressive in-plane strength. The interlaminar plane, which is most influenced by the matrix's properties, has one of the lowest resistance to failure in a composite, therefore the delamination onset and growth is governed by interlaminar fracture toughness of the composite material [10]. Delamination may be induced by external loading via the free edge, e.g. static bending, compression and tension, or by cyclic fatigue, impacts of low-to-medium energy, during manufacture, or during their usage [12]. These scenarios can result in opening or sliding of the adjacent plies in a laminate, which represent different modes of delamination. The present work focuses only on individual modes of delamination, although a brief disscussion about mixed mode delamination is presented in Chapter 3.

Within the plies of laminated composite the type of failure (matrix or fibre) is governed by the stress state of the plies. The failure is normally fibre dominated when the ply is loaded with tensile stresses in the direction of fibres (causing fibre rupture), where as in the case of stresses transverse to the fibre in-plane are likely to cause matrix damage within the ply, separating fibres one from another. In woven fabrics usually both modes contribute to ply failure, as sets of fibres have different orientation within the ply. The present work does not include ply damage as the focus is on delamination between the plies, although some additional work including ply damage has been done outside the frame of this thesis.

1.2 Scope of the Present Work

The objective of this thesis is predicting the non-linear behaviour that a laminated composite structure exhibits during delamination by means of numerical calculations with the Finite Element Method (FEM). The emphasis is on the delamination process in woven composites and correlating the results to the fibre topology in the model. All FEM simulations are conducted with a general purpose FEM processor ABAQUS/Standard 6.14 *(Dassault Systèmes Simulia Corp., Providence, RI, USA).* Finite Element models with detailed representation of woven topology are set-up with the help of a special shell-based textile unit cell, developed at the Institute of Lightweight Design and Structural Biomechanics, TU Wien. The tow discretization is based on shell elements and the interface is represented by cohesive elements incorporating the delamination like damage behaviour. Laminates are simulated in two different load cases, both of them being standard test methods for delamination in UD laminated composites, and compared to a reference model with homogeneous shell discretization.

Following the introductory chapter, analytical determination of delamination in laminated composite structures is reviewed in Chapter 2, where the load-displacement and fracture resistance curves for each test method are derived from the linear elastic fracture mechanics theory.

Chapter 3 covers the modelling approach when setting up numerical models of laminated composite structures. A brief discussion about the ply modelling and ply interaction, i.e. the contact, is presented. As mentioned, the delamination process is governed by interface properties. The cohesive zone method is used for damage modelling of the interface, where the cohesive elements are placed and coupled to the surrounding shell elements which are representing plies in the laminate. For the purposes of embedding a detailed textile structure within the models, additional coupling approaches of the elements are discussed in this chapter. Such an approach is necessary to ensure numerical efficiency of the present models.

In Chapter 4 the laminate's geometry, material properties and Finite Element models considering the modelling approach from Chapter 3 are discussed. Three FEM models are prepared: a reference model, a model with two layer embedded domain of textile unit cells, and a model with four layer embedded domain. Mesh refinements and boundary conditions are reviewed on all models. A brief overview of the textile unit cell, with mesh arrangement, internal constraints and embedded coupling is also presented in this chapter. Before moving on to the results of the analysis performed on this models, analysis controls, which help in achieving a converging solution, are reviewed.

The computational results are shown and discussed in Chapter 5, where all of the concepts described until this point are used. The results are presented and discussed in two main sections, one for each of the delamination test methods described in Chapter 2. In each section, all models are compared in terms of the load-displacement response, energy release rate and damage dissipated energy during delamination. Additionally, different energy evaluation techniques are compared and reviewed alongside with numerical determination of the crack front and propagation throughout the interface, which has a significant influence on indirect results, such as the energy release rate. The computational results are discussed in detail and correlated to the model's properties and topology.

Finally, a summary of the present work is given in Chapter 6, where the contribution of this thesis and ideas for further work in this field are also presented.

1.3 Literature Overview

A brief review of the literature relevant to this thesis is presented here. For understanding the mechanics of composite materials the reader may refer to the textbook by Jones [13], which covers the topics of laminate's properties and mechanical behaviour.

Initially, the delamination studies were performed on natural laminates, such as wood or body muscles. They served as a starting point for the first studies of delamination in composites back in 1980's. Williams and Hashemi in 1988 and 1989 [14, 15] derived a general analysis for the determination of delamination called the Corrected Beam Theory (CBT), which is still one of the most accurate predictions and is widely used in the recent relevant publications. The article by Hashemi in 1990 [2] covers the analysis of interlaminar fracture of laminates in greater detail and serves as a reference for the analytical approach of non-linear behaviour caused by delamination in this work. The characterization of delamination is based on the energy approach from the linear elastic fracture mechanics theory. Several studies have also been done about the fracture behaviour of composite laminates containing woven fabrics using the established test methods during that era [12, 16, 17]. Recently, the development of composite materials led to a standardization of test methods for delamination in UD laminates [18, 19].

Parallel with the development of Finite Element Method, numerical simulations of delamination in laminates have been done with several different approaches. Most common ones are the Virtual Crack Closure Technique, first introduced by Rybicki and Kanninen [20], and the Cohesive Zone Method, proposed by Camanho and Davilla [9]. The latter is used in this work and it's based on the traction-separation approach which requires special purpose finite elements called cohesive elements [21]. Studies about delamination in recent years have been focused mostly on how to efficiently predict the laminate's response to external loads by means of FEM simulations. Amongst others, Harper [5] investigates the influence of a number of elements in the cohesive zone length, which has a big influence on predicting interlaminar damage onset and propagation. The methodology for predicting the propagation of delamination with cohesive elements is reviewed in [22]. Damage evolution under mixed mode conditions based on the energy approach is defined in the criterion by Benzeggagh and Kenane [23] and is useful for the interfaces whose critical energy release rate is the same along all shear directions. It is used for the purposes of this work. A shell element based unit cell approach for modelling and simulating fibre reinforced textile composites is proposed by Gager and Pettermann [8] which enables numerically efficient multi-scale predictions of the textile composite behaviour both on macro (laminate size) and meso-structural (fiber tow size) level. Simulations done in this thesis are based on this approach.

Measuring crack length in delamination experiments can be quite challenging, thus many studies are proposing new approaches to evaluate the critical energy release rate, especially for delamination under transverse shear stresses in the interface [6, 10, 24–27]. A brief comparison between some of them are presented in Appendix 8.

2 Delamination in Laminated Composite Structures

In this chapter we discuss the analytical characterization of delamination in laminated composites. The main focus is on the determination of the load-displacement curve and fracture resistance curve, i.e. the R-curve, from test methods for each mode of delamination (see Fig. 2.1). The analysis is based on Linear Elastic-Fracture Mechanics (LEFM).

Delamination in laminated composites may be considered as crack propagation, which is characterized via the energy dissipated per unit area of growth, also named the critical energy release rate, $\mathcal{G}_{\rfloor}$, in fracture mechanics [2,24]. Since the delamination in laminated composites is usually interlaminar, there are different modes of delamination under different loading conditions. In general we consider three different modes of fracture proposed by Irwin [28], which are shown in Fig. 2.1. In the mode I, or opening mode, the structure is loaded with tensile forces in such a way that the crack faces separate in a direction normal to the plane of the crack. Mode II, or in-plane sliding mode, corresponds to the shear forces being loaded parallel to the crack surfaces, resulting in sliding of the crack faces over each other in the direction perpendicular to the crack front. Mode III, or tearing mode, the structure is loaded by shear forces parallel to the crack front, and the crack surfaces slide over each other in the direction parallel to the crack front. The emphasis in this thesis is only on mode I and II delamination. Often opening and shear mode can occur simultaneously during certain loading conditions which lead to the mixed-mode failure, which can be characterized for each ratio of mode I to mode II loading. More about mixed-mode will be discussed later in Section 3.2.1

Several test methods have been developed in order to characterize the laminate's resistance to delamination in terms of interlaminar fracture toughness. Figure 2.2 shows the test method for mode I delamination called the Double Cantilever Beam (DCB) test and the Fig. 2.3 shows one of the test methods for measuring mode II delamination named the 3 point End Notched Flexure (ENF) test. Note that for mode II there are many test methods proposed by different authors, e.g the 4 point ENF test and the End Loaded Split (ELS) test, however both the DCB and the ENF test have become standardized test methods (for DCB and ENF test see DIN EN 6033 and DIN EN 6034, respectively) for uni-directional (UD) laminates made of carbon fibre reinforced plastic materials. For the purposes of this thesis only these two test methods are considered.

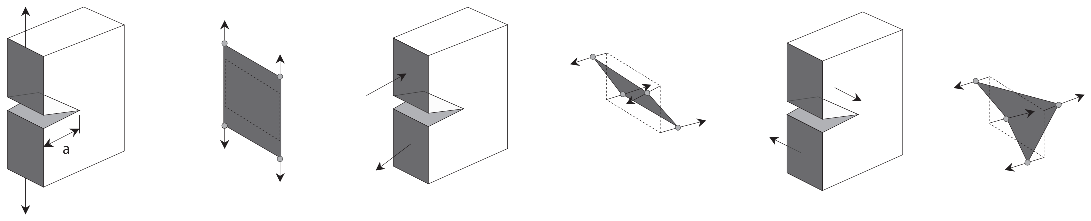

(a) Mode I: Opening (b) Mode II: In-plane sliding (c) Mode III: Tearing

Figure 2.1: Three modes of fracture. The figures on the right indicate displacements on a plane normal to the crack near the crack tip. [29]

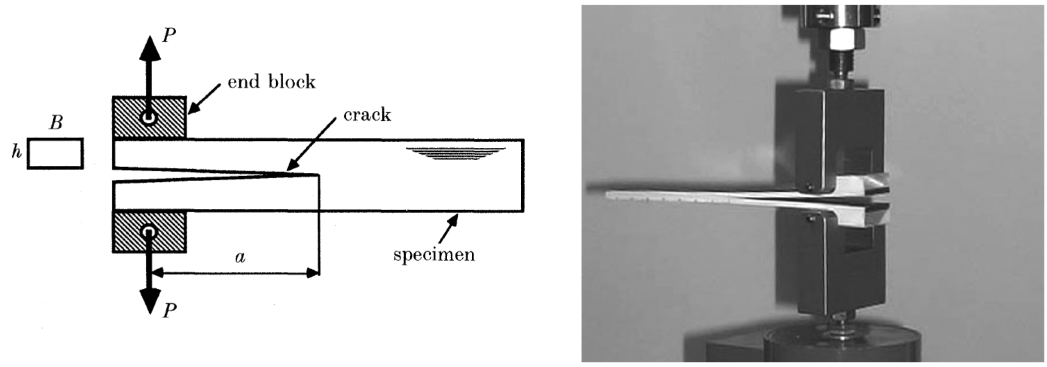

(a) (b)

Figure 2.2: Experimental setup for mode I Double Cantilever Beam (DCB) test. [2,3]

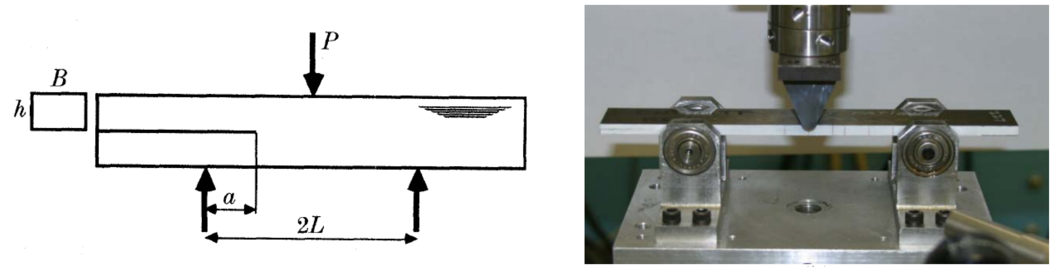

(a) (b)

Figure 2.3: Experimental setup for mode II 3 point End Notched Flexure (ENF) test. [2,4]

Typical DCB or ENF test configurations contain a universal test machine with crosshead displacement control and a load cell linked to a data acquisition system for measuring the reaction force. Crack propagation is usually measured with a high-resolution camera synchronised with the loading. Results are usually presented in terms of a load-displacement curve which corresponds to the reaction forces on loading arms (load cell) in relation to their displacement.

The analytical determination of the load-displacement curve is based on the beam theory. The initial linear elastic response prior to any damage is straightforward. However, when the internal strain energy, entered via the external load, is high enough the crack begins to propagate, which results in a non-linear response due to the growing

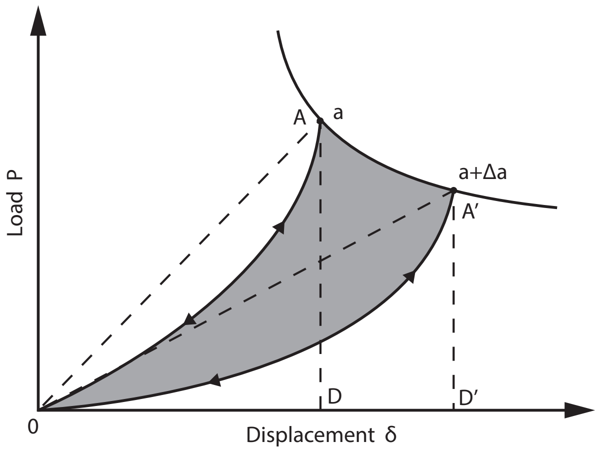

Figure 2.4: Load-displacement dependency during crack propagation. Grey area defines the energy release rate $\mathcal{G}$. [2]

crack in the laminate. The prediction of crack growth can be based on energy balance. The Griffith criterion states that "crack growth will occur, when there is enough energy available to generate new crack surface" [2]. The critical energy release rate $\mathcal{G}_c$ is then the work needed to create a unit area of fully developed crack. It has the dimensions of J/m^2 and for a crack of length a and width B is defined as [2]

$$\mathcal{G}_c = [(\Delta U_e/\Delta a) - (\Delta U_s/\Delta a)]/B \quad , \tag{2.1}$$

where U_e is the external work, U_s the strain energy and Δa the associated increment of crack growth. This definition is true for any form of linear and non-linear elastic behaviour. Figure 2.4 illustrates load, P, versus displacement, δ, from where we can define that

$$\Delta U_e = \mathrm{ADD'A'} \quad , \tag{2.2}$$

$$\Delta U_s = \mathrm{0A'D'} - \mathrm{0AD} \quad , \tag{2.3}$$

therefore the change in energy is $\mathrm{0AA'0}$ (shaded area), which with the change in crack surface $B\Delta a$ determines $\mathcal{G}_c$ [2]. The arrows on lines in Fig. 2.4 indicate elastic behaviour in loading and unloading (for simplicity they have an identical curve, although they can differ due to the hysteresis and zero offset effect [2]).

$$\mathcal{G}_c = \frac{area\, 0AA'}{B\,\Delta a} = \frac{\Delta U}{B\,\Delta a} \tag{2.4}$$

If the deformation behaviour is assumed to be linear and the point A has the coordinates (P_1, δ_1) and point A' (P_2, δ_2) then the change in energy can be written as

$$\Delta U = \frac{1}{2}(P_1\,\delta_2 - P_2\,\delta_1) \quad . \tag{2.5}$$

The area methods suffer from the disadvantage that they determine an average value of $\mathcal{G}$ over some discrete Δa which makes them inaccurate. The analysis can be modified by invoking a function of specimen compliance, which can be measured as a function of crack length

$$C(a) = \delta / P \quad . \tag{2.6}$$

From the Fig. 2.4 and Eq. (2.5) we can write that $P_2 = P_1 + \Delta P$ and $\delta_2 = \delta_1 + \Delta\delta$ therefore we can deduce from Eq. (2.6) that $\Delta\delta = P\,\Delta C + C\,\Delta P$ and

$$\mathcal{G} = \frac{1}{2}B^{-1}\,P_1^2\,\Delta C/\Delta a = \frac{1}{2}\,B^{-1}\,P^2\,\mathrm{d}C/\mathrm{d}a \quad . \tag{2.7}$$

Therefore a point value of $\mathcal{G}$ can be found from the measured force P, if $C(a)$ is determined experimentally and the curve fitted so that dC/da can be found for a given a. Although area definition of the energy release rate yields a good physical representation of it, it is more convenient for purposes of this thesis that we use the beam theory to analyse the results.

A general analysis for determination of the energy release rate of a laminated structure or beam is shown on Fig. 2.5. Crack propagation from point O to O$_1$ on Fig. 2.5b may be formulated in terms of the applied moments at the ends of the crack. M_1 and M_2 are the upper and lower bending moments over the crack at the section OB and OA, respectively. At the crack tip (section CD) the bending moment is a sum of $M_1 + M_2$.

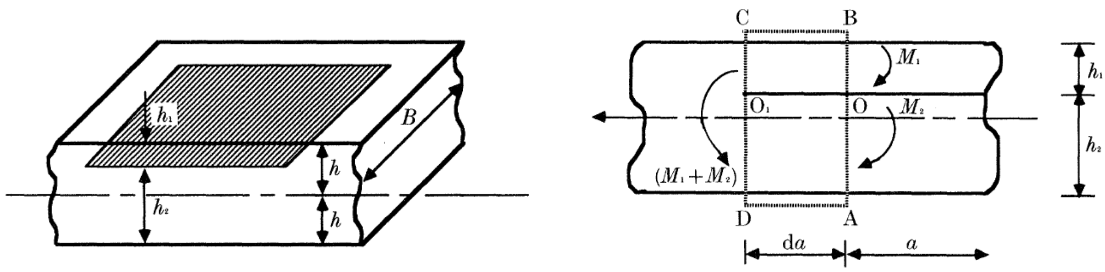

(a) (b)

Figure 2.5: Delamination model in laminated composite. [2]

The total energy release rate over crack length da, propagating from O to O$_1$, can be written as [2]

$$\mathcal{G} = \frac{3}{4B^2\, h^3\, E_{11}} \left[\frac{M_1^2}{\xi^3} + \frac{M_2^2}{(1-\xi)^3} - (M_1 + M_2)^2 \right] \quad \texttt{with} \quad \xi = \frac{h_1}{2h} \quad , \tag{2.8}$$

where E_{11} is the axial Young's modulus of the laminate. Equation (2.8) can be partitioned into mode I and II components [2] as

$$\mathcal{G}_{\mathrm{I}} = \frac{6h_1^3}{B^2\, E_{11}\, h_2^3\, (h_1^3 + h_2^3)} \left[M_2 - \left(\frac{h_2}{h_1} \right)^2 M_1 \right]^2 \quad , \tag{2.9}$$

$$\mathcal{G}_{\mathrm{II}} = \frac{18 h_1\, h_2}{B^2\, E_{11} (h_1 + h_2)^2 (h_1^3 + h_2^3)} (M_2 + M_1)^2 \quad . \tag{2.10}$$

2.1 Mode I Delamination

The DCB test specimen has an initial crack length of a_0 which is usually produced by inserting a thin layer of Teflon (PTFE) between the laminates during manufacturing. Each cantilever has a thickness of h, length of L and width of B as shown on Fig. 2.6a. Boundary conditions at the edge with the initial crack are applied in such a way that the tips of the cantilevers have only one translational degree of freedom, that is in the direction 3, where the tip displacement, δ_{I}, is introduced. Rotational degrees of freedom are unconstrained. Figure 2.6b shows the deformed specimen during the DCB test. Tip displacement is measured as the distance between the cantilever beam tips.

The test specimen can be considered as two single cantilever beams of length equal to the crack, a, where a simple beam theory can be used to give [5]

$$\delta_{\mathrm{I}} = \frac{2\, P\, a^3}{3\, E_{11}\, I} \quad , \tag{2.11}$$

where I is the second moment of area for each cantilever along its length

$$I = \frac{B\, h^3}{12} \tag{2.12}$$

and E_{11} the Young's modulus of each cantilever along its length.

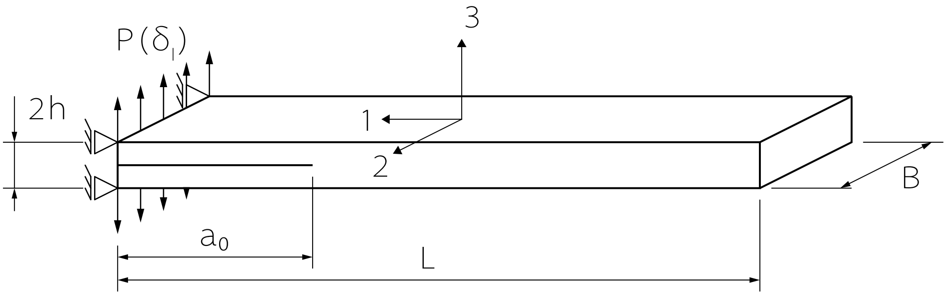

(a)

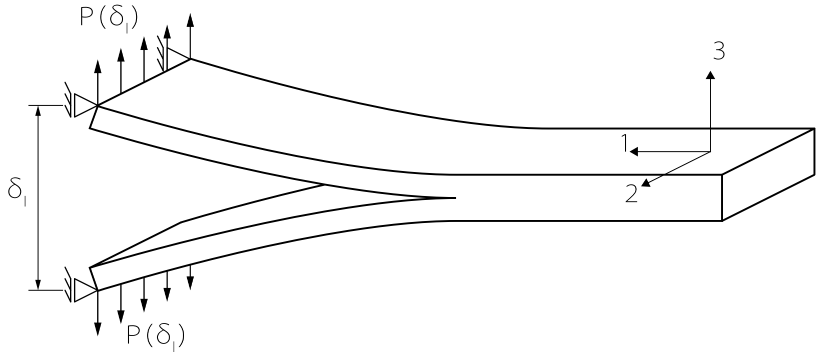

(b)

Figure 2.6: Double Cantilever Beam test method.

In reality there are some deflections and rotations at the crack tip which results in shear and local deformations. These effects can be modelled by adding an artificial length $\chi\, h$ to the real crack length a [2]. Therefore Eq. (2.11) can be written as

$$\delta_{\mathrm{I}} = \frac{2\,P\,(a+\chi\,h)^3}{3\,E_{11}\,I} \quad , \tag{2.13}$$

where χ is the correction parameter and h the cantilever thickness. An analytical value of χ is used [2], with

$$\chi = \sqrt{\frac{E_{11}}{11\,G_{13}}\left[3-2\left(\frac{\Gamma}{1+\Gamma}\right)^2\right]} \quad \texttt{with} \quad \Gamma = 1.18\frac{\sqrt{E_{11}\,E_{22}}}{G_{13}} \quad . \tag{2.14}$$

E_{22} and G_{13} are transverse Young's and transverse shear modulus, respectively.

The energy release rate for the DCB test can be acquired from Eq. (2.9) where we have $M_2 = -M_1 = P\,a$, $h_1 = h_2$ and the correction length of, $\chi\, h$, which gives us the mode I energy release rate [30] as

$$\mathcal{G}_{\mathrm{I}} = \frac{P^2(a+\chi\,h)^2}{B\,E_{11}\,I} \quad . \tag{2.15}$$

Under a linearly increasing tip displacement, the point load P increases until the point when the strain energy release rate reaches the critical value of G_{I_c} and the crack begins to propagate through the interface. This is represented with a dashed line in Fig. 2.7. The load-displacement response for each increment of crack extension can be found by combining the Eq. (2.13) and Eq. (2.15) set to G_{I_c} [5] where the crack length is no longer the initial value but it can be evaluated from Eq. (2.13). The crack length, a, is included in Eq. (2.15) which give us the response for crack propagation as

$$P_p = \sqrt{\frac{2}{3}} \left(\frac{B^3 \, \mathcal{G}_{\mathrm{I}_c}^3 \, E_{11} \, I_a}{\delta_{\mathrm{I}}^2} \right)^{1/4} \qquad . \tag{2.16}$$

The crack length during delamination propagation can be evaluated from Eq. (2.13), where the point load force is taken from Eq. (2.16), as

$$a = \sqrt[3]{\frac{3\delta_{\mathrm{I}} \, E_{11} \, I}{2P_p}} - \chi \, h \qquad . \tag{2.17}$$

Figure 2.8 shows the relation between the crack length and tip displacement. Again, it is shown that the crack propagation is triggered at the critical value of tip displacement, that is when the critical energy release rate is reached.

Using the conventional beam theory at the DCB test, the energy release rate reaches the critical value at the critical displacement and stays constant throughout the crack propagation, since there cannot be a higher rate than the critical one. With the corrected beam theory we invoke a certain artificial crack length which results in the fracture resistance curve as a transition phase to that critical value, as seen on the Fig. 2.9. In any case, the initial crack length a_0 must be taken into account when configuring the fracture resistance or R-curve.

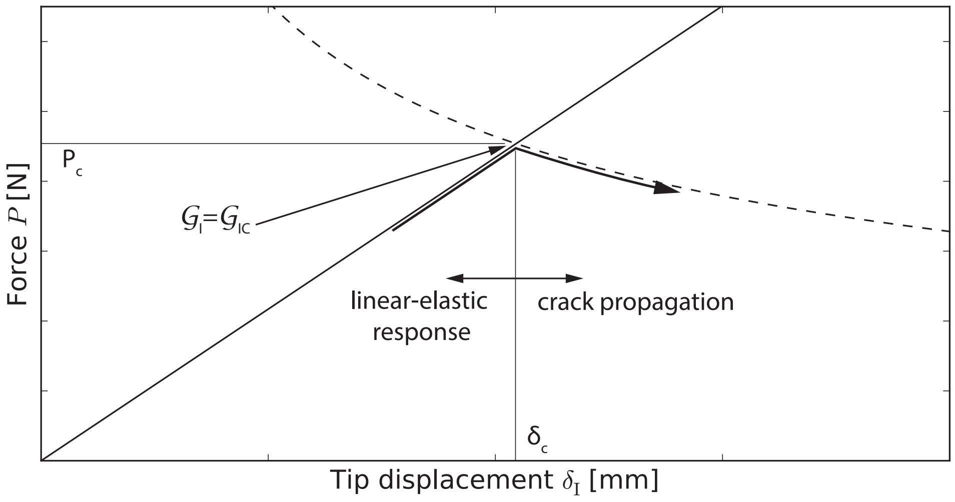

Figure 2.7: Analytical load displacement curve for DCB test

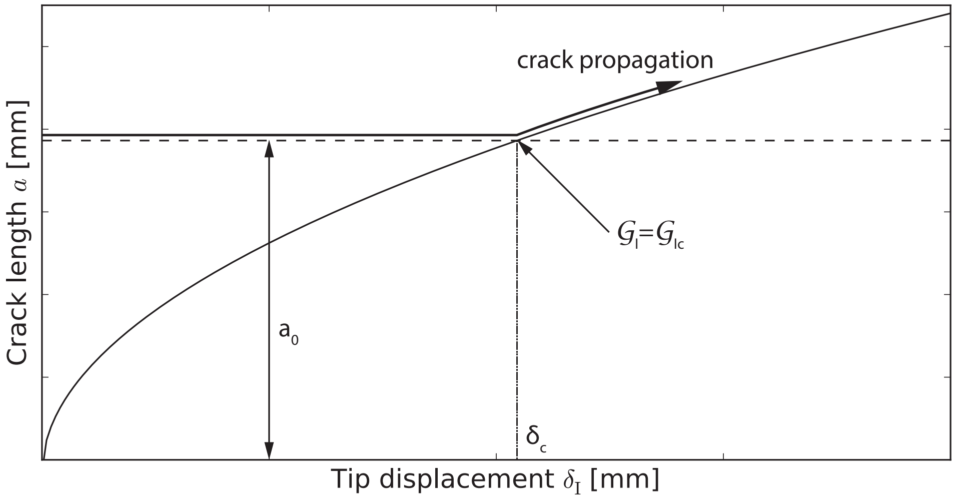

Figure 2.8: Crack length in relation to tip displacement for the DCB test.

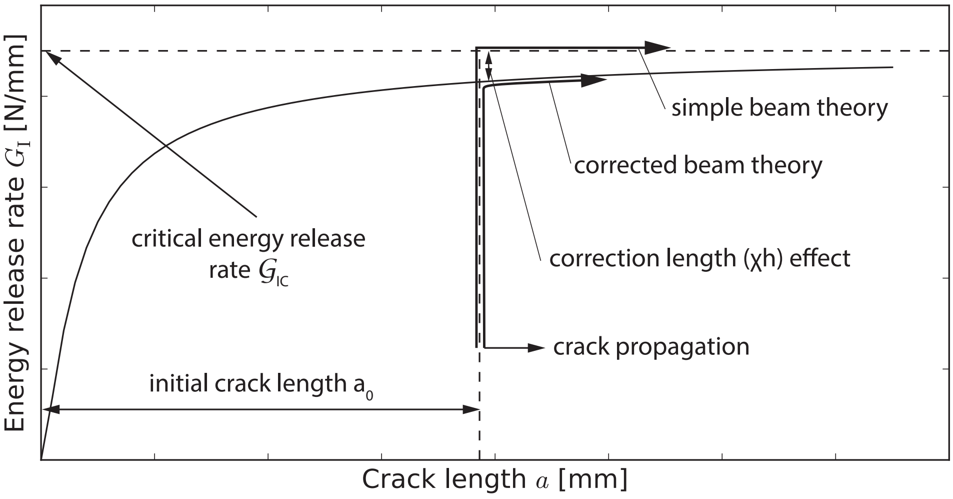

Figure 2.9: Fracture resistance curve (R-curve) for mode I delamination.

2.2 Mode II Delamination

The three point End Notch Flexure (ENF) test has been widely used to measure the mode II interlaminar fracture toughness of laminated composites. Similar as with the DCB test, a specimen with initial crack is used as shown in Fig. 2.10. It is effectively carried out with a three point bending test of the laminate, where the initial crack length a_0 should be at least 0.7 times the half span length L in order for the crack propagation being stable [31, 32].

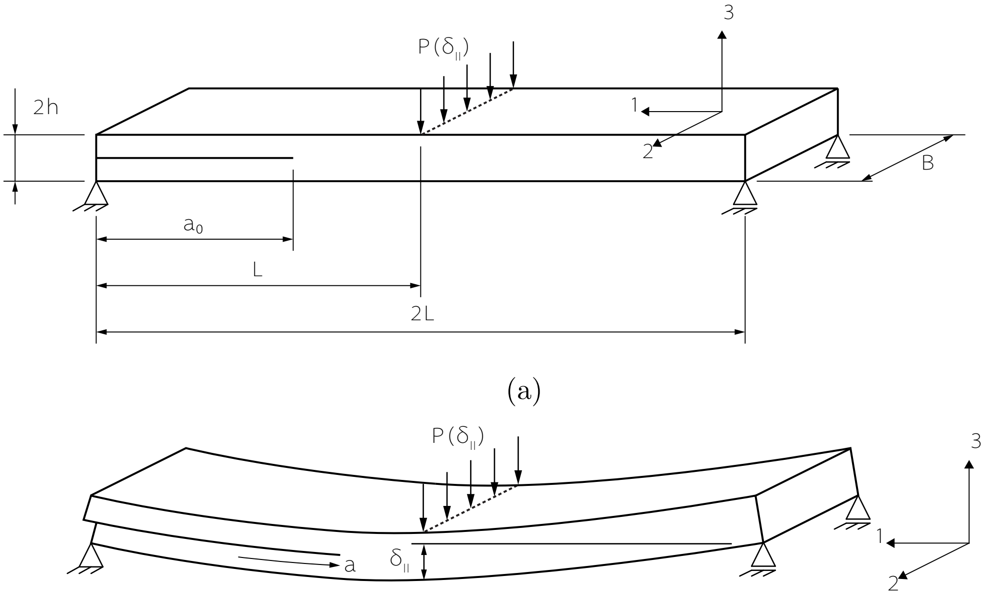

(a)

(b)

Figure 2.10: Three point End Notch Flexure test method.

The same principles applies as for the DCB test. In this case the added correction crack length is $0.42\chi\, h$ [30]. The tip displacement using the corrected beam theory is therefore given by [30] as

$$\delta_{\text{II}} = \frac{3P\,(a + 0.42\chi\, h)^3 + 2P\,L^3}{96E_{11}\,I} \quad , \tag{2.18}$$

where δ_{II} is the central displacement. The strain energy release rate for mode II can be deduced from Eq. (2.9), where for a symmetrical case, i.e. $h_1 = h_2 = h$, we have equal moments $M_1 = M_2 = -\frac{1}{4}\,P(a + 0.42\chi\, h)$ and the energy release rate is defined as

$$\mathcal{G}_{\text{II}} = \frac{3(a + 0.42\chi\, h)^2\, P^2}{64B\, E_{11}\, I} \quad . \tag{2.19}$$

Equation (2.18) gives the load-displacement relation for the elastic regime and at the point, where G_{II} meets the value of the critical energy release rate G_{II_C}, the crack starts to propagate. Again the relation in crack propagation regime can be found by combining the Eq. (2.19) and Eq. (2.18). From the Eq. (2.19) we can extract the crack length as

$$a = \frac{1}{P}\sqrt{\frac{64\mathcal{G}_{\mathrm{II}_C}\,B\,E_{11}\,I}{3}} - 0.42\chi\,h \tag{2.20}$$

and insert it into Eq. (2.18). This yields the load-displacement curve for the crack propagation (delamination).

$$\delta_{\mathrm{II}} = \frac{1}{32E_{11}\,I}\left[\frac{1}{P^2}\left(\frac{64\mathcal{G}_{\mathrm{II}_C}\,B\,E_{11}\,I}{3}\right)^{2/3} + 2L^2\,P\right], \qquad \delta_{\mathrm{II}} \geq \delta_{\mathrm{II}_C} \tag{2.21}$$

Combining Eqs. (2.18) and (2.21) gives the complete load-displacement curve for mode II fracture test as shown in Fig. 2.11.

Figure 2.12 shows the relation between crack length and central displacement by combining the elastic response and crack propagation curve, which can be found by combining Eqs. (2.21) and (2.19) with energy release rate set to the critical value of G_{II_C}. By bending the specimen, as it is the case in the ENF test, we can invoke only a certain amount of energy (that correlates to the bending curvature) before the plies failure occurs. In order to reach the critical energy for delamination, it is necessary to have a sufficient length of the initial crack length ($a_0 \approx 0.7\,L$). Note that in the case of ENF test, the correction length does not have such an effect on the energy release rate as in the case of the DCB test (see Fig. 2.9), because it needs an initial crack for delamination to start and therefore the critical energy release rate is theoretically achieved at the critical central displacement (as is the case in the simple beam theory for DCB test).

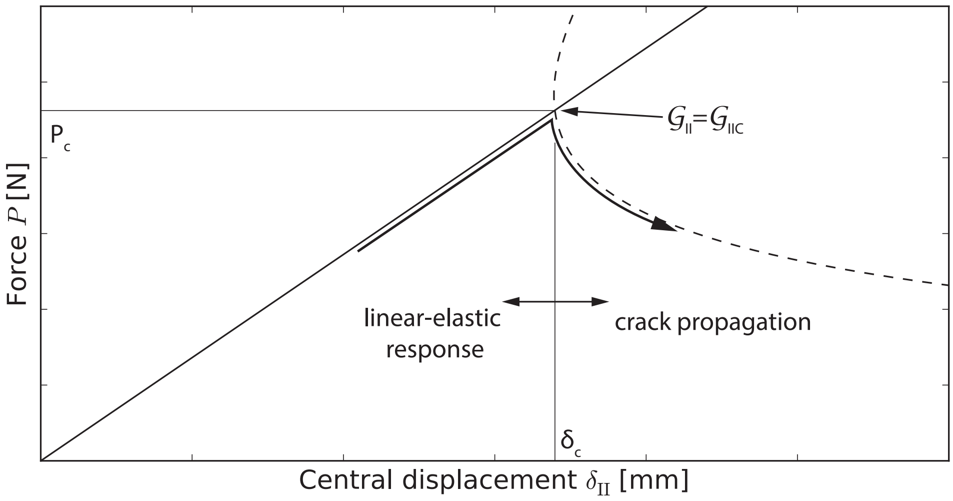

Figure 2.11: Analytical load-displacement curve for the 3 point ENF test.

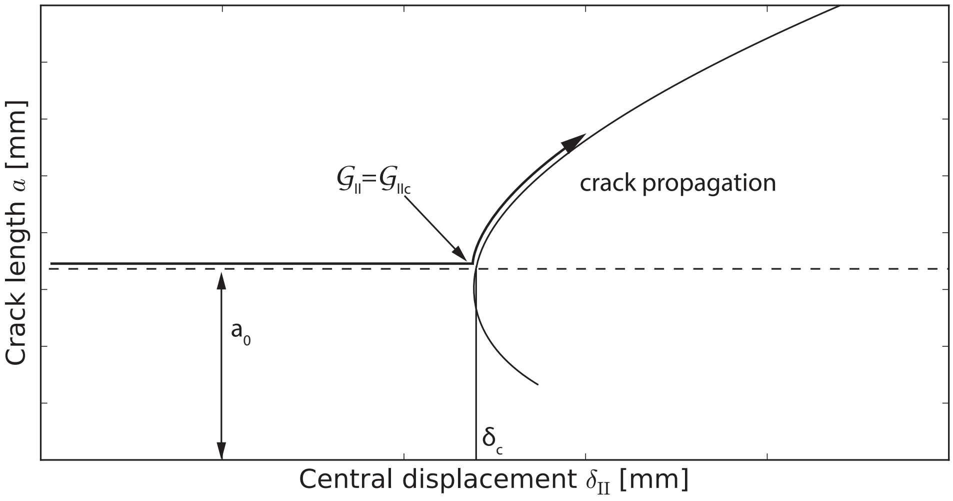

Figure 2.12: Crack length in relation to central displacement for 3 point ENF test.

3 Modelling Approach

A modelling approach for numerical simulations of delamination is set up in the framework of Finite Element Method (FEM). The main goal of the present work is to investigate the delamination process in laminated textile composites and for this reason, a simplified (homogenized) model and a more detailed numerical models with identical baseline geometry and material properties are prepared as shown on the Fig. 3.1. The same modelling approach is used in all models to simulate ply and interface behaviour, which together defines the behaviour of laminated composite. The detailed models include a textile substructure around the area of the potential crack path as an embedded domain in the basic model which enables simulating the process of delamination in greater detail with still reasonable numerical efficiency, which is what this thesis is aiming for. The homogeneous model serves as an reference to which other models are compared to.

The laminate models consist out of three main parts, i.e. the plies, interface and the

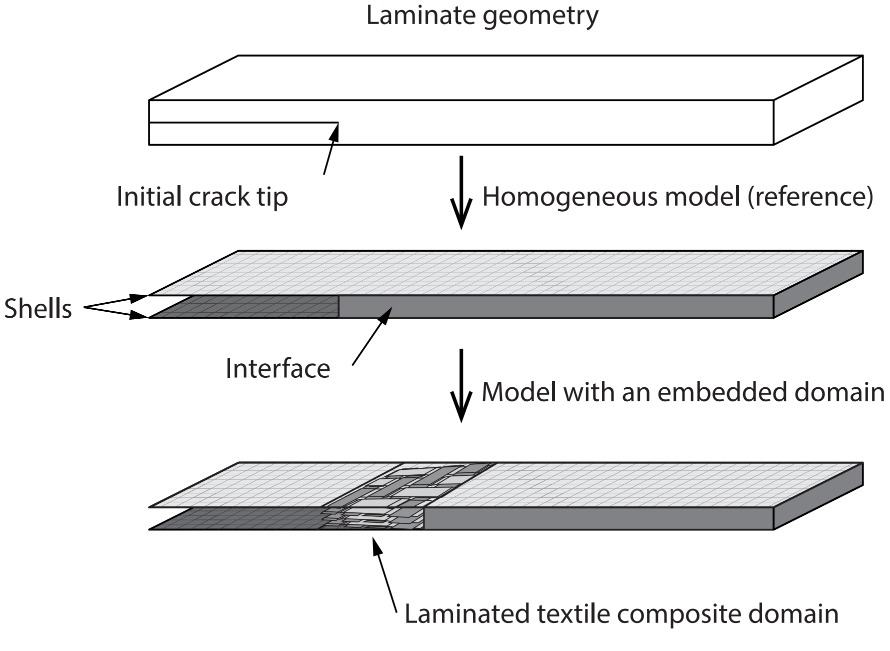
Laminate geometry
Initial crack tip
Homogeneous model (reference)
Shells
Interface
Model with an embedded domain
Laminated textile composite domain

Figure 3.1: Modelling approach in laminated composites.

embedded domain of textile composite in the detailed models. Modelling techniques of these parts are presented in this section, with emphasis on interface constitutive behaviour and model constraints when combining domains of different modelling length scale inside the model.

Definitions and explanations regarding the finite elements are mostly related to the commercial FE package ABAQUS and its helpful user manual which can be found in reference [21].

3.1 Ply Modelling

As mentioned before, laminated composites are constructed out of stacked plies of fabric embedded in a resin or matrix. The plies are generally very thin and their thickness is significantly smaller than its other dimensions. It is a common practice to use shell elements for discretization of such structures as they enable computationally less costly simulations, which is even more important with non-linear material behaviour such as delamination.

Conventional shell elements S4 are being used in the present work. The thickness of elements is defined in the section properties, whereas for continuum (solid) elements the nodal geometry defines the thickness. This way, the conventional shell elements define a structure by defining the geometry at a reference surface, which is typically the mid plane, but can also be the top or bottom surface of the structure.

Shell elements posses both translational and rotational degrees of freedom at each node to define element's deformation. For each integration point, a number of section points over the thickness can be assigned to calculate its cross-section behaviour via integration approximation methods. In Abaqus the default method for conventional shell elements is the Simpson's rule with five section points for homogeneous and three points per layer for a composite section.

The surface director definition in shell elements is important when defining coupling or contact between different shell sections. Top surface of a shell is the surface in the positive normal direction and the bottom surface is in the negative direction along the normal vector.

3.1.1 Shell Composite Section in ABAQUS

The potential delamination path, i.e. the interface where the delamination can occur, is predefined in the DCB and ENF simulations with an initial crack in the model, as discussed in Chapter 2 Therefore a few simplifications can be made when modelling the laminate. Instead of considering each ply and interface between them, they can be combined, resulting in fewer sections of the laminate that need to be modelled. For instance, only the upper and lower half of the laminate and the interface between them is modelled in the reference model. This way the upper and lower half can be individually represented with a single layer of shell elements.

Note that this is only true for the homogeneous model, as the detailed model includes an embedded domain of complex textile ply structure and matrix. However, the embedded domain is only present at a small part of the initial delamination path and the other part of the laminate is modelled the same as the homogenized model. More about the textile domain is discussed later in Section 4.2

Abaqus has a convenient way of defining laminated composites. Instead of modelling each ply and its properties separately, the Composite Section can be used. It enables stacking multiple layers of materials into a composite with individual material properties, thickness, orientation angle and thickness integration points. For the purposes of the present work this tool was used, although the mentioned parameters are not really needed, nevertheless it enabled us to orderly stack multiple layers of homogenized textile material for the upper or bottom half of the laminate on one single shell. Further details are explained in Chapter 4

3.1.2 Ply Interaction

The plies in a laminate interact through the corresponding interfaces and where there is none, i.e. where the plies are debonded, they interact through contact between their surfaces. As mentioned in the previous section for the reference model, plies above and below the interface of the initial crack are modelled with a single shell, thus there is no interaction possible between plies in each half of the laminate. In a model with a textile domain, such interaction is possible in the domain itself, but that will be discussed later. In this section, the focus is on the contact interaction. The interface behaviour between laminates is discussed in the next section.

Both parts of the laminate are bounded via the middle interface where the delamination takes part. In the ENF test, the laminate shells interact with each other as the bottom surface of the top shell and top surface of the bottom shell come into contact (shell thickness are taken into account). During delamination, the contact area between surfaces in contact is changing as the crack propagates.

Contact interaction between shells is defined as a hard contact. When surfaces are in contact, any contact pressure can be transmitted between them and when they separate, the contact pressure reduces to zero. Separated surfaces come into contact when the space between them reduces to zero. The penalty method is a stiff approximation

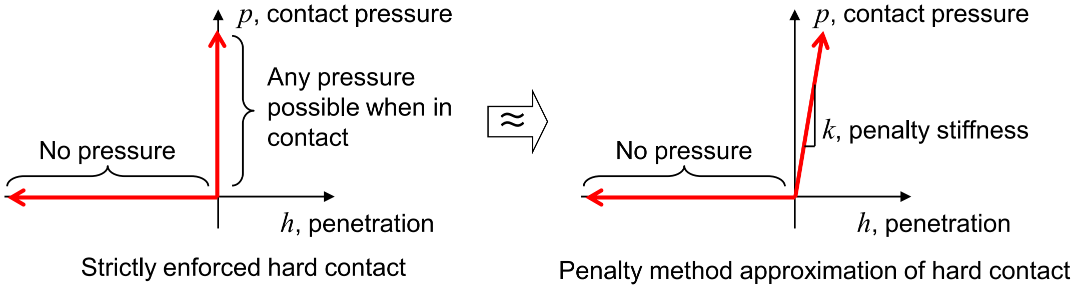

Figure 3.2: Hard contact and penalty method

of the hard contact through pressure-penetration relation. With this method the contact force is proportional to the penetration distance, so some degree of penetration will occur. The penetration distance is minimized with penalty stiffness, k, which increases the contact force with overclosure of the surfaces. The penalty method can be non-linear or linear, with the latter being the default setting in Abaqus and used for the present work. Figure 3.2 shows the penalty method approximation of hard contact.

Shear forces are not being transferred between the surfaces in contact as frictionless behaviour is being defined. Friction between the constituents can cause severe numerical difficulties. The friction is neglected to decrease computational effort of the simulations.

In Abaqus, the contact interaction can be defined via contact pairs and general contact. The contact pair method requires from the user to define master and slave surfaces in contact, whereas the general contact does it automatically. The overall trend in contact modelling is towards greater automation and general contact requires little user input compared to other methods. However, it does enable independent specification of contact interaction domain, contact properties, and surface attributes.

General contact uses finite-sliding and surface-to-surface formulation, which considers the shape of both master and slave surfaces. It enforces the contact conditions in an average sense over the contact region nearby slave nodes rather than only at individual nodes on slave surface (i.e. node-to-surface formulation). Because of that it is computationally more expensive, but it provides more accurate stress and pressure results than other formulations. Thicknesses and offsets associated with shell surfaces are accounted for automatically in general contact. By default general contact uses penalty method and initial over-closures can be adjusted in a strain-free manner. This adjustments are disabled to avoid mesh change and instead an accurate mesh is created with correct thickness assignments.

3.2 Interface Modelling

Several methods are available when it comes to delamination simulation, amongst them the Virtual Crack Closure Technique (VCCT) and the Cohesive Zone Method are the most common. VCCT was first introduced by Rybicki and Kanninen [20]. The method is based on the assumption that when a crack extends by a small amount, the energy released in the process is equal to the work required to close the crack to its original length [9]. Although VCCT method provides good results on delamination onset and stability, it has a few disadvantages. It requires a pre-existing initial delamination to predict the onset of the crack front when the local energy release rate reaches a critical value. Although we have mentioned that the interface, where the delamination takes part, is predefined, this is not entirely true for the model with the textile domain. In the present work, we are investigating the delamination process in laminated textile composites where the crack front could possibly move through the layers, which is something VCCT method does not enable (without multiple initial cracks throughout the layers of the laminate).

Instead, the Cohesive Zone Method is used to model the interface. It uses cohesive elements which are placed at the interfaces between plies.

3.2.1 Cohesive Zone Method

Cohesive elements are typically used at the interface between solid or shell elements to simulate the initiation and evolution of crack growth or delamination in resin-rich layer connecting the layers of composite materials. Firstly named decohesion elements, they were proposed by Camanho in 2002. They are based on the Dudgale-Barenblat cohesive zone approach [33,34], which can be related to the Griffith's theory of fracture when the cohesive zone size is negligible compared to characteristic dimensions [9].

Compared to other analysis techniques such as the VCCT, cohesive elements have the capability to predict both damage initiation and propagation without the requirement of an existing pre-crack, therefore cracks have the potential to propagate where ever the cohesive elements are placed at [5, 9, 21].

Cohesive elements are formulated on a continuum eight-node (for 3three dimensional simulation) element, typically with very small or zero initial thickness. In such cases the constitutive response is usually defined by a traction-separation law and they model a zero thickness interface regardless of the geometrical thickness. If the interface adhesive layer has a finite thickness and macroscopic material properties, more conventional materials models are used such as the continuum approach [21].

When modelling the interface and their neighbouring parts it is convenient to ensure they have matched meshes as shown on Fig. 3.3. This enables a straightforward way to attach cohesive elements to other parts, in this case laminates or plies, simply by sharing the same nodes. This way no additional interface definitions are needed which would required more equations to solve and slowing down the simulation.

Figure 3.3 also shows that when sharing nodes in cohesive elements between shells, the cohesive elements have a finite non-zero geometrical thickness if the mid-planes of the shells are chosen as a reference planes. However, when the response of the cohesive elements is based on a traction-separation approach, as it is the case for the present work, Abaqus assumes by default that the constitutive thickness is equal to

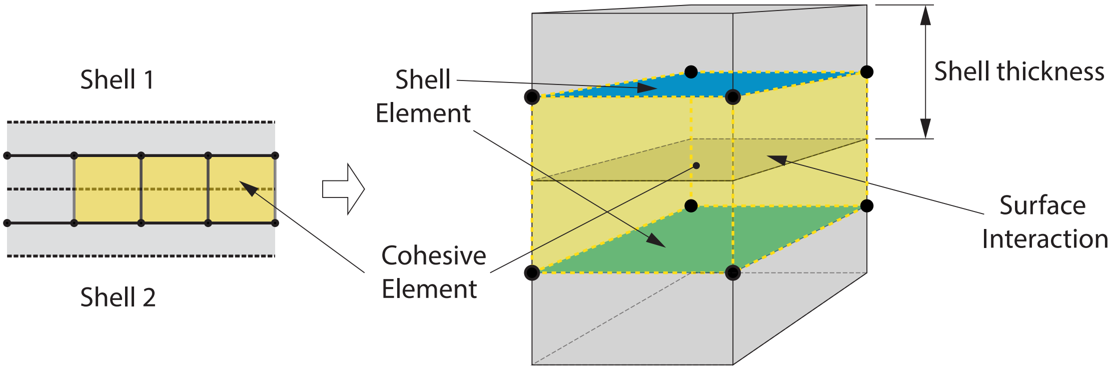

Figure 3.3: Cohesive element attached with two shells elements

one. This ensures that nominal strains are equal to the separation displacements, since the nominal strains are the separations divided by the constitutive thickness. Actually, it is typical that the constitutive thickness used for traction-separation response is different than the geometrical thickness of the cohesive elements.

Figure 3.4 demonstrates a bi-linear form of traction-separation law for individual mode of delamination, which is used in the present work and is just one of several laws for simulating the delamination process in composite structures. Other forms of the traction-separation law, e.g. exponential, can be also be implemented. It relates traction, t, to separation, δ, for individual loading mode. Mode I, II and III delamination are initiated by traction components t_n, t_s and t_t.

The initial response is assumed to be linear-elastic until the traction reaches same maximum value, t_{max}, which is the interfacial strength for the corresponding loading mode. This is the region of damage initiation, i.e. the damage is initiated when the individual traction component reaches its maximum value. The following region defines softening behaviour until the element is fully damaged and reaches zero traction, which numerically indicates debonded plies, since the cohesive element cannot carry any load. This is referred as the damage evolution. Unloading and reloading the element takes into account the scalar damage parameter d, as demonstrated in Figure 3.4. The total area enclosed by the traction-separation curve is equal to the critical energy release rate or fracture toughness of the interface.

As discussed in the previous chapter, the DCB and ENF test characterize delamination for mode I and II, respectively. However, it is common that both modes contribute to delamination. Although the simulations in the present work focus on each delamination mode separately, mixed mode delamination is not excluded between the plies in laminated textile composites. Therefore brief a description of mixed-mode delamination is presented below.

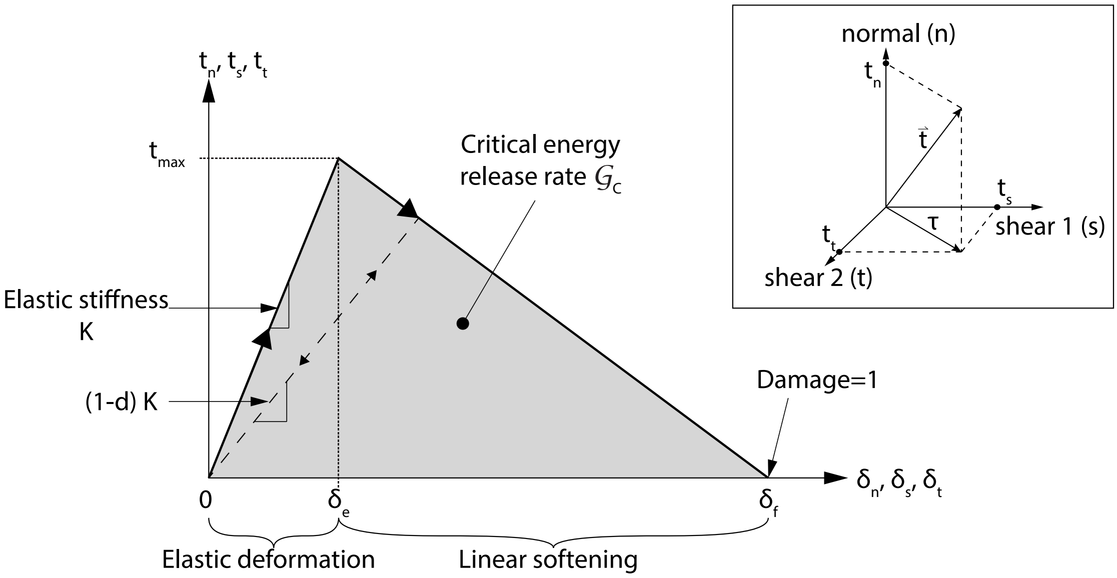

Figure 3.4: Bi-linear traction-separation law.

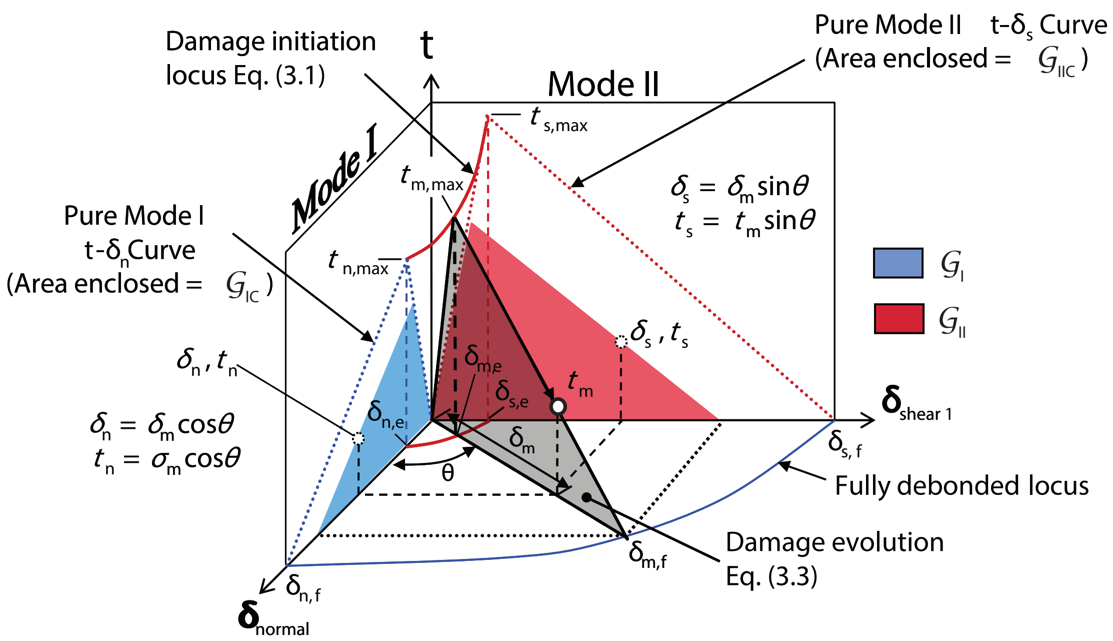
Damage initiation locus Eq. (3.1)
t
Mode II
Pure Mode II t-δ_s Curve (Area enclosed = $\mathcal{G}_{IIC}$)
Mode I
$t_{s,max}$
$t_{m,max}$
$\delta_s = \delta_m \sin\theta$
$t_s = t_m \sin\theta$
🟦 $\mathcal{G}_{I}$
🟥 $\mathcal{G}_{II}$
Pure Mode I t-δ_nCurve (Area enclosed = $\mathcal{G}_{IC}$)
$t_{n,max}$
δ_s , t_s
δ_n , t_n
$\delta_{m,e}$
t_m
$\delta_{s,e}$
$\delta_{n,e}$
$\delta_n = \delta_m \cos\theta$
$t_n = \sigma_m \cos\theta$
δ_m
θ
$\delta_{shear\ 1}$
$\delta_{s,f}$
Fully debonded locus
Damage evolution Eq. (3.3)
$\delta_{m,f}$
$\delta_{n,f}$
δ_{normal}

Figure 3.5: Bi-linear mixed-mode traction-separation law. [5]

Mixed-mode formulation is presented in Fig. 3.5, where the normal opening mode I is on the $0-t-\delta_{normal}$ plane and the transverse shear mode II on the $0-t-\delta_{shear\,1}$ plane. The triangles $0-t_{n,max}-\delta_{n,f}$ and $0-t_{s,max}-\delta_{s,f}$ are the bi-linear traction-separation laws in pure opening and pure shear loading modes, respectively. Mixed-mode displacement δ_m can be at any point on the $0-\delta_{normal}-\delta_{shear}$ plane and it contains normal and shear components.

Damage initiation for mixed-mode loading can be characterized by various parameters. The quadratic nominal stress criterion (QUADS) is commonly used, where the damage initiates when a quadratic interaction function involving the nominal traction ratios reache a value of one. The mixed-mode damage initiation displacement, $\delta_{m,e}$ in Fig. 3.5, and interfacial strength $t_{m,max}$ can be calculated using a quadratic criterion

$$\left(\frac{\langle t_n\rangle}{t_{n,max}}\right)^2 + \left(\frac{t_s}{t_{s,max}}\right)^2 + \left(\frac{t_t}{t_{t,max}}\right)^2 = 1 \quad , \tag{3.1}$$

where the subscripts n, s and t represent the normal traction component and the two shear traction components. The symbol $\langle\quad\rangle$ signifies that a compressive normal stress component does not initiate any damage. Note that the vast majority of interface failures are due to opening and in-plane sliding mode.

Damage evolution can be based on the dissipated energy during the damage process. The fracture energy is equal to the area under the traction separation curve in Fig. 3.4.

The power law criterion states that failure under mixed-mode conditions is governed by a power law interaction of the energies required to cause failure in the individual (normal and shear) modes [21]. It is formulated as

$$\left(\frac{\mathcal{G}_{\mathrm{I}}}{\mathcal{G}_{\mathrm{I}_c}}\right)^{\alpha} + \left(\frac{\mathcal{G}_{\mathrm{II}}}{\mathcal{G}_{\mathrm{II}_c}}\right)^{\alpha} + \left(\frac{\mathcal{G}_{\mathrm{III}}}{\mathcal{G}_{\mathrm{III}_c}}\right)^{\alpha} = 1 \quad , \tag{3.2}$$

where $\alpha \in (1.0, 2.0)$ is an empirical parameter from the mixed-mode test [5]. Each fraction presents a portion of each damage mode that contributes to total element damage.

The Benzeggagh-Kenane (BK) criterion is another common fracture criterion [23] and it is particularly useful when the critical fracture energies during deformation in both shear directions are the same, i.e. $\mathcal{G}_{\mathrm{II}_c} = \mathcal{G}_{\mathrm{III}_c}$. It is defined as

$$\mathcal{G}_{\mathrm{I}_c} + (\mathcal{G}_{\mathrm{II}_c} - \mathcal{G}_{\mathrm{I}_c}) \left(\frac{\mathcal{G}_S}{\mathcal{G}_T}\right)^{\eta} = \mathcal{G}_c \quad , \tag{3.3}$$

where $\mathcal{G}_S = \mathcal{G}_{\mathrm{II}_c} + \mathcal{G}_{\mathrm{III}_c}$ is the portion of energy done by shear traction and its separation. The total energy release rate $\mathcal{G}_T$ sums all the tractions and separations from each mode, i.e. $\mathcal{G}_T = \mathcal{G}_{\mathrm{I}} + \mathcal{G}_S$. The cohesive parameter η defines the influence of shear traction in the interface. For the present work the value of two was used in the simulations.

$\mathcal{G}_C$ being the total fracture energy release rate during damage process can be found for example in Figure 3.5 as the area under $0 - \sigma_{m,max} - \delta_{m,f}$ triangle.

Equations (3.2) or (3.3) corresponds to fully damaged elements or complete interface failure that occurs at the relative displacement $\delta_{m,f}$. Both criteria can determine the fully debonded locus presented on Figure 3.5.

3.3 Embedded Domain Coupling

In this section we will focus on ways to embed a more detailed model into a simpler one in order to optimize the simulation of delamination in complex composite structure with containing such domain only where it is needed.

Combining separate parts of the model in Abaqus can be achieved with surface based tie constraints. This effectively means that the translational and rotational motion as well as all other active degrees of freedom are made equal for a pair of surfaces. By default, nodes are tied only where the surfaces are close enough to one another. Similar as with the contact interaction, one surface is designated as a master surface, while the other as slave surface. Position tolerance can be set to determine the constrained nodes based on the distance between the slave nodes and the master surface. A more controlled way of defining constrained nodes is to specify a node set containing the slave nodes to be constrained regardless of their position to the master surface. This method enables a greater control and is used in the present work.

Figure 3.6 shows a few different ways of using tie constraints between shell sections. As Fig. 3.6c indicates, tie constraints enable combining separate laminate parts together in one model. Edge-based surfaces can be created to tie several parts together and embedding a textile structure into the base model. While the surface-to-surface formulation generally avoids stress noise at tied interfaces, this formulation is converted to node-to-surface when a node-based or edge-based surface is used. The surface-to-surface approach enforces the constrains in an average sense over a finite region, instead of at only discrete points as in the node-surface approach. In any case, it is important that the embedded domain is positioned in such a way, that tie constraints do not influence the accuracy of the solution.

A surface based tie constraint is also very useful for any mesh refinements as it enables transitions in mesh density within the model, as shown in Fig. 3.6b, or to merge layers of elements together - Fig. 3.6a. Tie constraint effectively kinematically links each of the slave nodes to have the same motion as the point on the master surface to which it is closest.

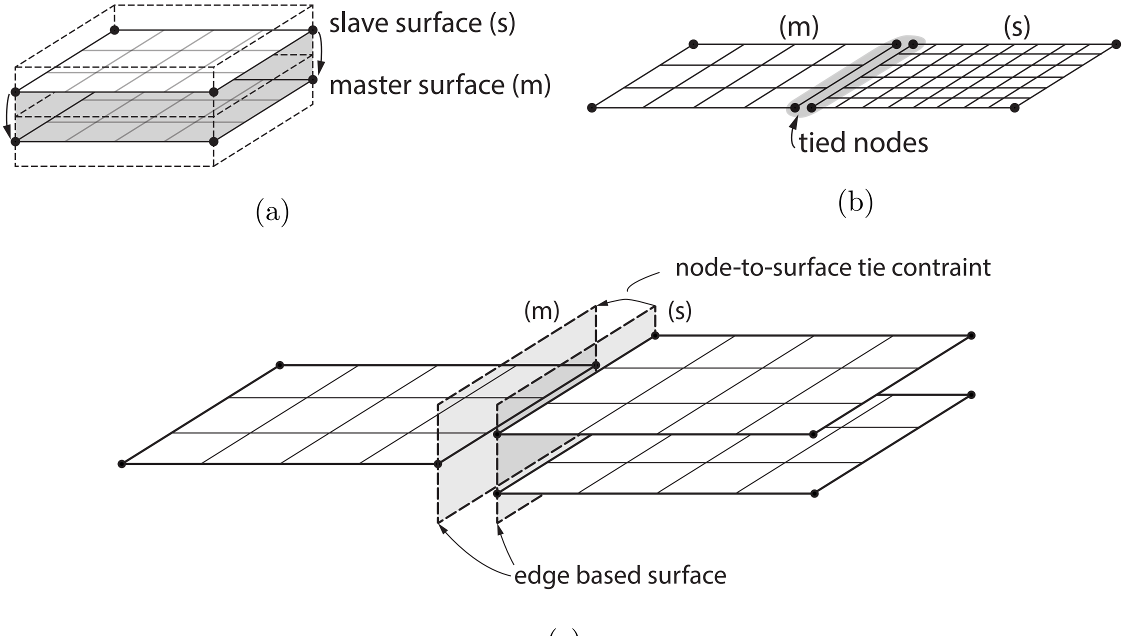

(a)

(b)

(c)

Figure 3.6: Tie constrains being applied between surfaces on various shell section combinations.

4 Laminate Geometry, Properties and Numerical Models

The basic model geometry is defined in such a way that it can easily embed a domain of a detailed textile composite substructure, which is made out of unit cells from the Institute of Lightweight Design and Biomechanical Structures, TU Wien, Vienna (from now on ILSB). The unit cell is briefly described later in Section 4.2

Figure 4.1 shows the specimen's geometry used in all of the considered models. The initial crack length a_0 is set differently for the DCB and the ENF simulations. Models in DCB simulation have $a_0 = 38,63$ mm whereas the models used in ENF simulation have $a_0 = 53,63$ mm due to recommendation in the Section 2.2. The width of the model is defined as two spans of the mentioned unit cell and similar regarding the height, which is defined as 6 layers of the unit cell. Such configuration enables a straightforward embedding of different size textile domains made out of ILSB unit cells.

Three different numerical models are investigated within this work. As a reference model, a homogeneous representation of the composite laminate is used for each half. The other two models of interest include an embedded textile domain with different number of layers, i.e. two and four layers of textile plies. Acronyms are used when referring to the models with an embedded domain. They are:

- EMB2 (model with an embedded domain containing two layers of textile plies.)
- EMB4 (model with an embedded domain containing four layers of textile plies.)

Therefore the reference and EMB2 models have one cohesive interface discretized, whereas the EMB4 model has three.

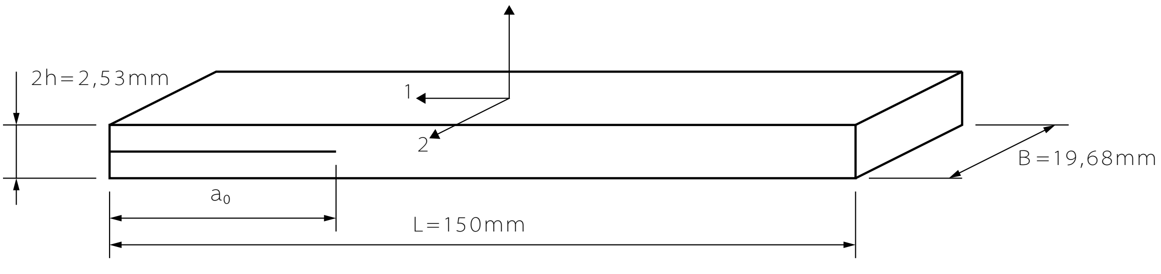

Figure 4.1: Model baseline geometry.

4.1 Reference Model

Many studies have been conducted on the analysis of delamination in composites, particularly for mode I, mode II and mixed-mode. The majority of the models used in simulations are straightforward and use material properties of a homogenized composite laminate. The aim of this work is to investigate delamination in greater detail with complex numerical models, thus it is reasonable to set a reference model to which the later results can be compared to. Therefore a homogeneous model was set up with a basic representation of the laminated composite structure.

4.1.1 Material Properties

The material used for the numerical simulations is a 2x2 twill weave carbon reinforced epoxy. The material properties in Table 4.1 are provided by ILSB, E being the Young's modulus, G the shear modulus, $\mathcal{G}$ the energy release rate, t_{max} the critical traction, ν the Poisson's ratio and K the interface stiffness prior to damage initiation. Indices 1, 2, and 3 indicate directions from Fig. 4.1. Interface properities are assigned for each mode of fracture (I and II). Lamina or ply properties are assigned to shell composite sections of the model and the interface properties to a cohesive section between the two shells.

Table 4.1: Material properties of homogenized carbon/epoxy 2×2 twill weave composite material.

Homogenized laminae properties		Interface properties	
$E_{11} = E_{22}$ (MPa)	56589.32	$\mathcal{G}_{\mathrm{I}_c}$ (N/mm)	0.9
$G_{12} = G_{13} = G_{23}$ (MPa)	4185.86	$\mathcal{G}_{\mathrm{II}_c}$ (N/mm)	2.0
ν_{12}	0.045	$t_{\mathrm{I},max}$ (MPa)	60
		$t_{\mathrm{II},max}$ (MPa)	79.289
		$K_{\mathrm{I}} = K_{\mathrm{II}}$ (N/mm^3)	10^5

4.1.2 Mesh Definition

Delamination is a non-linear phenomena which can be challenging to simulate. Different damage modes in combination with contact interaction can make the analysis computationally expensive, therefore it is important to mesh the model efficiently. In this work, the preprocessing of the models was performed in the dedicated software *HyperMesh (Altair Engineering, Troy, Michigan, USA)* with corresponding definitions of node sets, elements sets and surface definitions.

The model is composed of two reference planes which are discretized with 4 node conventional shell elements with reduced integration (in Abaqus defined as S4R).

In general, linear (first-order, 4 nodes per one shell element) elements with reduced integration are prone to the hourglass effect. It is essentially a spurious deformation mode of an element mesh, resulting from the excitation of zero-energy modes of deformation. It typically manifests as a patchwork of zig-zag or hourglass like element shapes. Abaqus offers various tools to control this effect. The default setting for the hourglass control are used. In our case, the hourglass effect is controlled by the artificial hourglass stiffness, which is associated with the drill degree of freedom (rotation about the surface normal).

Interface elements, i.e. the cohesive elements COH3D8, share nodes with shell elements from the shell reference planes. As mentioned in the previous chapter, this simplifies the coupling of the cohesive elements to attached shells.

The region of most interest is around the initial crack tip in the direction of delamination propagation. Accurate analysis of composite delamination using cohesive elements depends on having sufficient number of elements within the softening region ahead of the crack tip (cohesive zone). The number of elements inside the cohesive zone can be determined as

$$N_{el} = \frac{L_{CZ,f}}{L_{el}} \quad , \tag{4.1}$$

where the L_{el} is the element length and $L_{CZ,f}$ is the length of the cohesive zone at the point of first element failure. A fine mesh is required that can capture the cohesive zone traction distribution. In [5] a value of $N_{el} \geqslant 3$ is proposed as a conservative approach. Traction distribution over cohesive elements is also important to track the numerical representation of a crack tip, i.e. where the elements fail and can no longer hold any load or contain tractions. For that reason the element length is set to 0.5 mm in the finer region. On the other hand, there is no need for a refined mesh further away from the delamination process thus the element length is 1 mm. Figure 4.2 shows the mesh of the reference model, where different mesh densities can be found. Along the width of the model the mesh distribution is 20 elements for the half-width, since the model uses symmetry boundary conditions. More about boundary conditions follows in Section 4.1.4

4.1.3 Section Definition

In Abaqus, the section assigned to elements defines their behaviour, i.e. a section invokes corresponding material and mechanical properties.

A composite section that was discussed in Section 3.1.1 is assigned to the top and bottom shells with 3 layers of composite material (see Table 4.1) oriented in the same direction. This essentially behaves as a single layer with the thickness of 3 layers. However, assigning a composite section enables greater options for changing the layers that might be simulated in further work beyond this thesis. Figure 4.3 shows the shell composite section. Each layer has a thickness of 0.4216 mm, totalling in 2.5296 mm for the laminate model of total six layers.

Abaqus also enables a straightforward way to define the constitutive response of cohesive elements that can be found in the interface of the model. The cohesive section

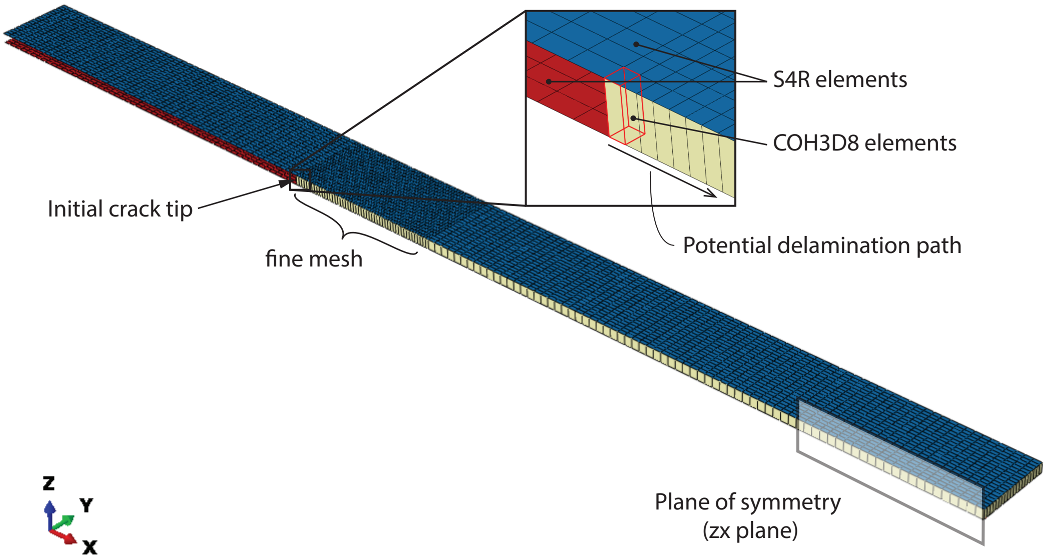
S4R elements
COH3D8 elements
Initial crack tip
fine mesh
Potential delamination path
Plane of symmetry
(zx plane)
Z
Y
X

Figure 4.2: Mesh discretization of the reference model.

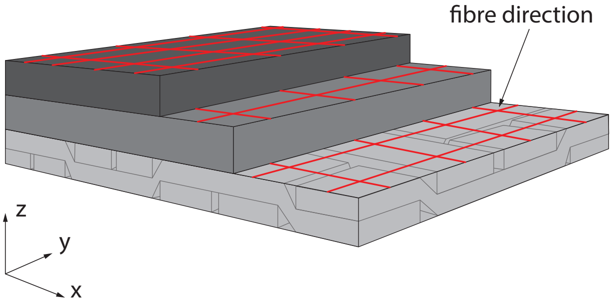
fibre direction
z
y
x

Figure 4.3: Shell composite section in Abaqus with three layers of homogenized textile composite material.

offers multiple settings for the behaviour of cohesive elements. The traction-separation law with energy based mixed-mode definition is chosen for the cohesive elements, thus following the definition in Section 3.2.1 and interface properties from Table 4.1.

4.1.4 Boundary and Loading Conditions

Although the results from this work are not being compared to any experimental results, it is still important that the simulation physically represents the delamination tests that are described in the standards, mentioned in Chapter 2. The model's mesh and section definitions define its response regarding to the boundary conditions and loading applications. Therefore to simulate the delamination tests, boundary and loading conditions have to physically represent the experiment through the kinematics of constrained nodes.

Referring back to Fig. 2.2 and 2.3 it is clear that the loading on the specimen is being transferred through loading blocks or objects that transfer the load over a certain area, rather than over one point as it is considered in the analytical approach. While the simulated boundary and loading conditions could be introduced in such way, this would increase computational time and effort with little advantages over the simplified way, i.e. constrained set of nodes at the load introduction.

Boundary conditions on a single node or set of nodes prescribe their displacements u_i and rotations ϕ_i, also called the degrees of freedom. In three dimensional space there are three translational and three rotational degrees of freedom, a pair for each of the axes (*x, y, z,* or 1, 2, 3, - the orientation nomenclature is presented in most figures).

For a better presentation, the boundary and loading conditions are presented schematically on Figs. 4.4 and 4.5 for the DCB and ENF simulation set-up, respectively Note that the load is being introduced as a displacement of the corresponding nodes. In case of DCB simulation, the displacement u_3 on the edge nodes on the reference planes is being applied gradually. Similar goes for the ENF simulation where the displacement is applied on the central nodes on the top layer. Therefore the simulations are displacement controlled.

It is a good practice to make use of symmetry boundary conditions whenever it is possible. This is a convenient way of increasing computational efficiency without compromising the results. Even more so, at the expense of decreasing the number of elements, one can afford denser mesh in the region of interest, thus improving resolution of stress distribution over that area. Symmetry boundary conditions ($u_2 = \phi_1 = \phi_3 = 0$) are being used on all nodes alongside one of the long free edge, as shown on Fig. 4.6. Consequently, only half width of the specimen is modelled. This also constrains the model in y or 2 direction, therefore no free movement of the model is allowed. To represent the whole width, the model can be mirrored over the constrained nodes.

The ENF model includes a general contact between the top and bottom shells with frictionless hard contact formulation, whereas the contact inclusion is not necessary in the DCB model, making the simulation faster to converge.

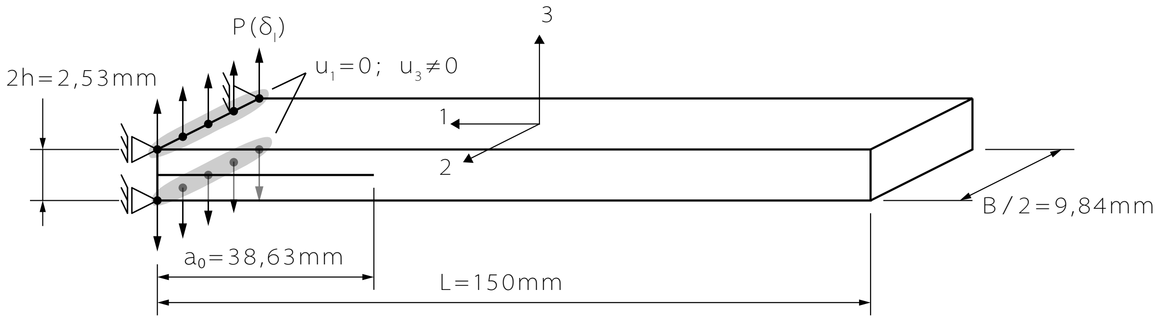

Figure 4.4: DCB homogenized model with geometry, boundary and loading conditions. The model is constrained in the direction 2 with symmetry boundary conditions (Fig. 4.6).

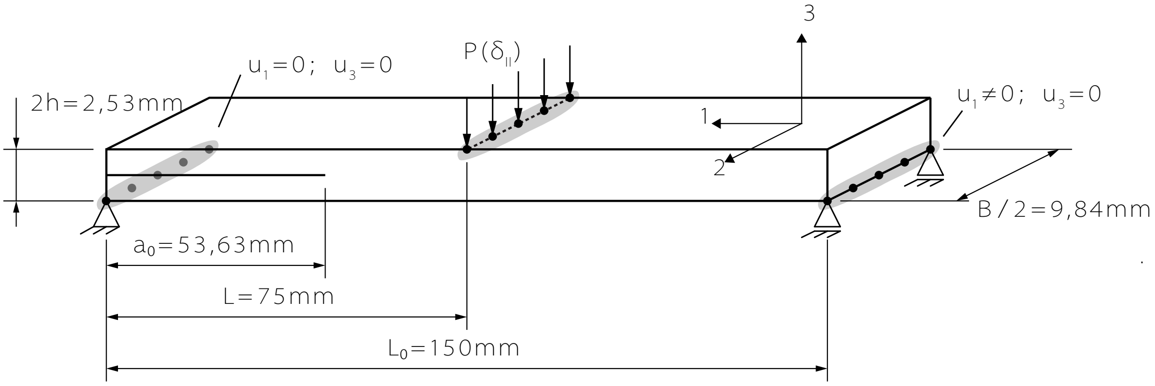
3
$u_1=0;\ u_3=0$
$P(\delta_{II})$
$u_1\neq0;\ u_3=0$
2h=2,53mm
1
2
B/2=9,84mm
a_0=53,63mm
L=75mm
L_0=150mm

Figure 4.5: ENF homogenized model with geometry, boundary and loading conditions. The model is constrained in the direction 2 with symmetry boundary conditions (Fig. 4.6).

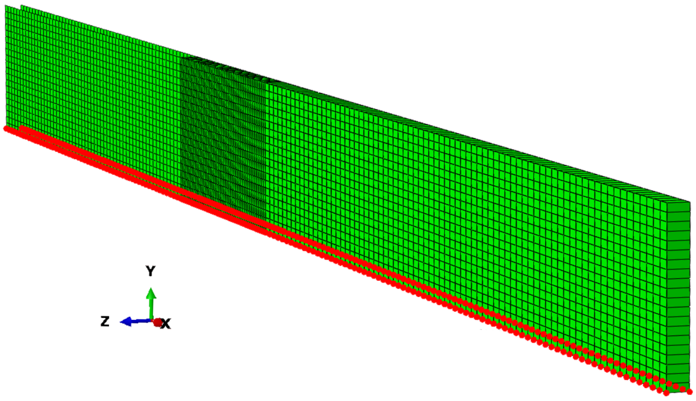

Figure 4.6: Symmetry boundary conditions over the $x - z$ plane are applied on highlighted nodes.

4.2 Models with an embedded textile domain

The discussed homogeneous model is used as a reference, providing a response in good agreement with the analytical results. The next step is changing the topology of the model by setting up a structure that mimics the textile topology at tow level. Instead of having a very simple structure with homogenized properties, a physically more representative model can be made, i.e. with complex topology and material properties for each of its component (tows and matrix). With unidirectional sets of fibres that are a few micrometers thick, woven into a textile ply and merged in a epoxy matrix, the model can become very complex and computationally very challenging. In order to make the model manageable, a few simplifications have to be made.

At the ILSB a special textile unit cell has been developed, firstly used for the purposes of numerical homogenization of textile composites based on shell element discretization (see [8]). The unit cell is a single layer textile composite model, with a periodically repeating geometry pattern. This enables the set-up of bigger models of fabrics. The unit cell is defined with an automated model generator programmed in Pyhton, that is capable of creating different weaving patterns and periodically sizes and layers of fabric. Besides geometrical parameters, the material and interface properties are defined for each of its components. This approach presents a powerful tool, that is capable of simulating textile composites in setting up details. Damage and failure can be accounted for in every of its components, providing an advanced model when simulating failure of composite materials.

Before further model description, a short discussion about the ILSB unit cell [8] follows in the next section.

4.2.1 ILSB Textile Unit Cell

The discretization of the ILSB textile unit cell geometry is based on shell elements (S4). A single layer of fabric consists of tows and unreinforced matrix. The corresponding shell elements are addressed as matrix and tow shells, respectively. The individual tows are treated as uni-directional (UD) laminae represented by shell elements. Their reference planes are defined as the mid-surface of the tows, as sketched in Fig. 4.7. Shell thickness and direction are also visualized on the same figure with dotted arrows. Modelling of the unreinforced matrix (shaded area in Fig. 4.7) is more challenging. Complex matrix geometry is attained by placing a uniform matrix shell reference plane at the top and bottom surfaces of the unit cell (thick dashed line in Fig 4.7). To fill the matrix areas according to the local geometry, a variable shell thickness is applied. A matrix pocket is formed over areas with no tow reinforcement. The thickness variation and direction of the matrix shells is presented by solid arrows in Fig. 4.7. Circles represent featured edges (not nodes) of tows. Elsewhere the matrix thickness is effectively non existent (order of 10^{-5} mm). Such discretization enables coupling between tows and matrix that resembles fibre tows reinforcing the surrounding matrix, e.g. epoxy. Additionally stacking multiple layers of unit cells can be done by coupling the matrix reference planes between the layers and the interface represented by inter-layer cohesive elements.

The Fig. **??** shows tows and matrix reference planes in three dimensional space. Tow and matrix shells are not connected directly, therefore additional links are required. In the unit cell, two tows are modelled as touching each other at the overlapping areas without any additional layer of matrix in between. At the overlapping areas, the adjacent tow surfaces are coupled via the inter-tow cohesive elements, as seen in Fig. 4.8 and Fig. 4.11. The same principle applies as in the reference model, i.e. the nodes of cohesive elements and tows are shared, therefore no additional coupling is required. Tie constraints are used to kinematically link the matrix shells to tows and matrix shells (at the other layer) at the corresponding locations, as shown in the Fig. 4.8 where the ties are illustrated with double sided solid arrows.

The unit cell comprising a single layer of fabric is modelled as a plane periodically repeating geometry pattern [8]. Figure 4.9 illustrates the unit cell cross section with dimensions in mm. For the purposes of this work, a 2/2 Twill Weave pattern was used with 2 × 2 periodicity of the unit cell, which creates a textile domain with size of 19.68 mm×19.68 mm. The height of the domain depends on how many layers of textile are considered, each layer being 0,4216 mm thick. A model with two layers of textile plies is used for DCB and ENF simulations. Additionally a four layer model is investigated in the ENF test. These textile domains were provided by the ILSB.

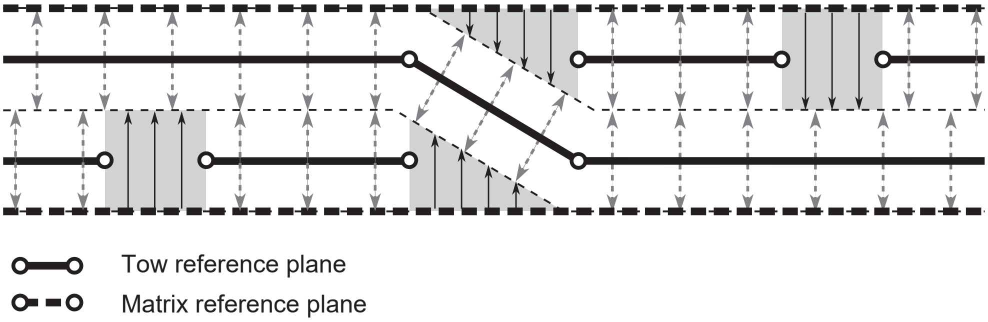

Figure 4.7: Cross section of a 2/2 Twill Weave indicating the shell reference planes, shell offset, and shell thickness. [8]

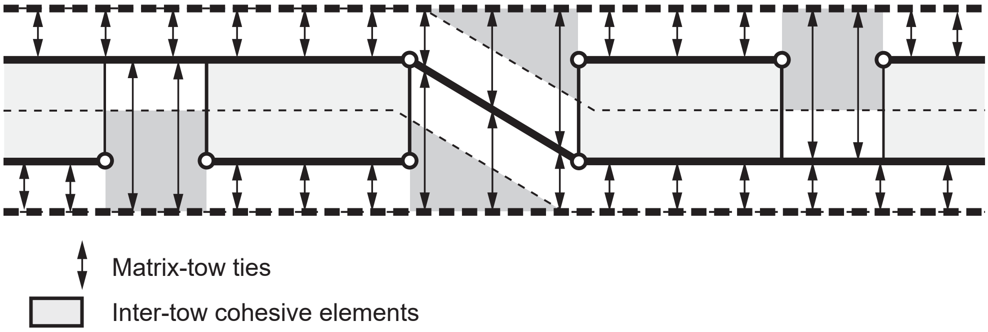

Figure 4.8: Cross section of a 2/2 Twill Weave indicating tie constrains between matrix and tows. [8]

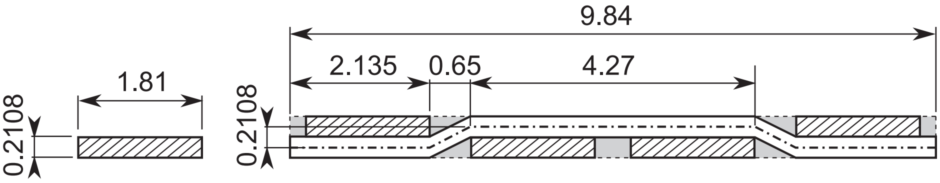
9.84
2.135
0.65
4.27
1.81
0.2108
0.2108

Figure 4.9: Cross section of the 2/2 twill weave showing the piecewise linear ondulation path and rectangular tow cross sections (hatched) with dimensions in mm. [8]

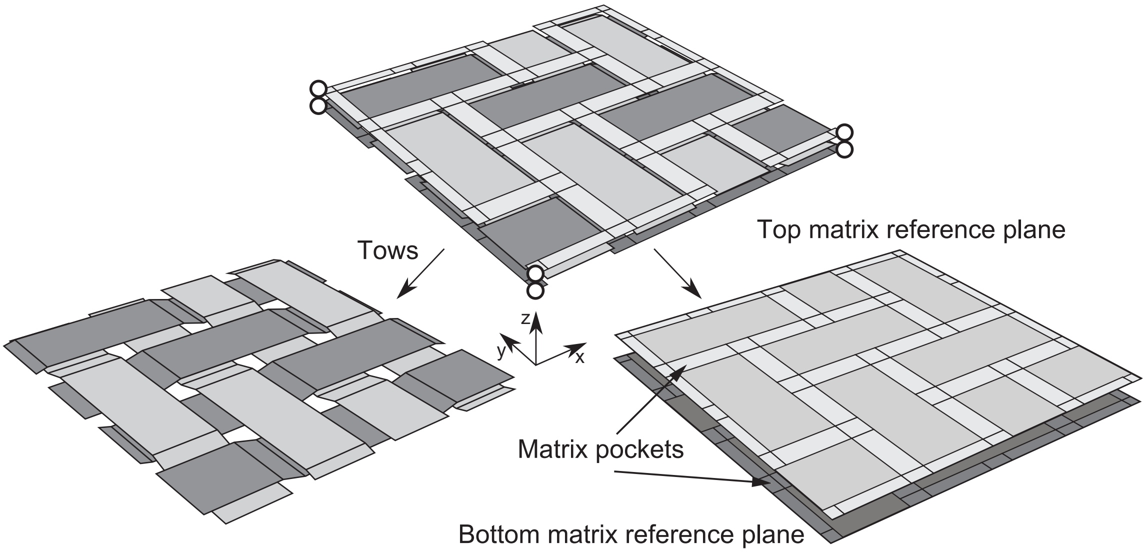
Tows
Top matrix reference plane
z
y
x
Matrix pockets
Bottom matrix reference plane

Figure 4.10: Shell element based unit cell assembled (top) and disassembled into tow reference planes (left) and matrix reference planes (right) for the 2/2 twill weave unit cell. [8]

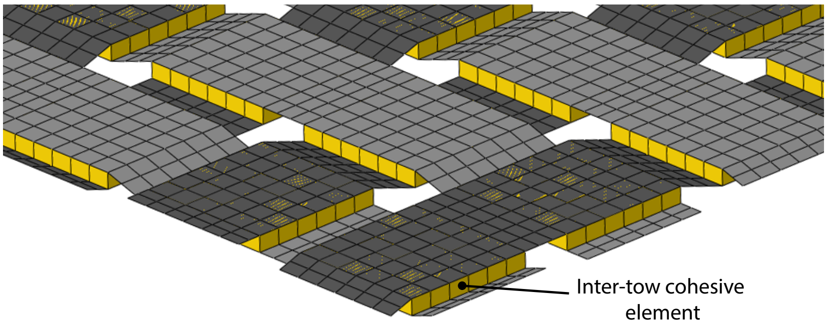
Inter-tow cohesive element

Figure 4.11: Inter-tow cohesive elements for 2/2 twill weave unit cell.

4.2.2 Material Properties

Homogeneous shells are assigned with material properties from the Table 4.1, which are acctually obtained from homogenization of the unit cell properties from Table 4.2. The material properties for each component in the model are provided by the ILSB. Note that damage is included only in the interface between plies for the present properties, thus no interface properties beside stiffness are presented for the interface between tows.

Table 4.2: Material properties of carbon/epoxy 2x2 twill weave composite material

Tows			
E_{11} (MPa)	142176.97	ν_{12}	0.23
E_{22} (MPa)	13819.56	$G_{12} = G_{13} = G_{23}$ (MPa)	6251.81
Matrix			
E (MPa)	3250	ν	0.37
Interface between tows			
		$K_{\mathrm{I}} = K_{\mathrm{II}}$ (N/mm^3)	10^5
Interface between plies			
$t_{\mathrm{I},max}$ (MPa)	60	$K_{\mathrm{I}} = K_{\mathrm{II}}$ (N/mm^3)	10^5
$t_{\mathrm{II},max}$ (MPa)	79.289	$\mathcal{G}_{\mathrm{I}_c}$ (N/mm)	0.9
		$\mathcal{G}_{\mathrm{II}_c}$ (N/mm)	2.0

4.2.3 Model Input Structure

As mentioned before, the textile domain is generated in the preprocessing stage using a Python script. The input is user-defined and the output is an Abaqus input file, that includes material and other properties of the domain. The individual model definitions are partitioned into corresponding files, which enables greater overview and simpler altering of the model. These files are then joined in a master input file, that includes all the necessary definitions to run the simulation. The input structure is shown in Fig. 4.12 where the shaded area is automatically created for the textile domain from the Python generator. For the homogeneous shells around the domain, the mesh definition and the corresponding element and node sets, surface definitions and coupling between the shells are created in Hypermesh. Additionally, the boundary conditions, output requests, contact interaction, etc. are defined for each simulation, respectively.

Consistent notations and nomenclature is essential for integration of the textile domain and homogeneous shells, which enables simulations for different loading applications and purposes in one model without any additional work. To achieve this, the organizational logic from the unit cell was followed in other parts of the model (as indicated in Fig. 4.12).

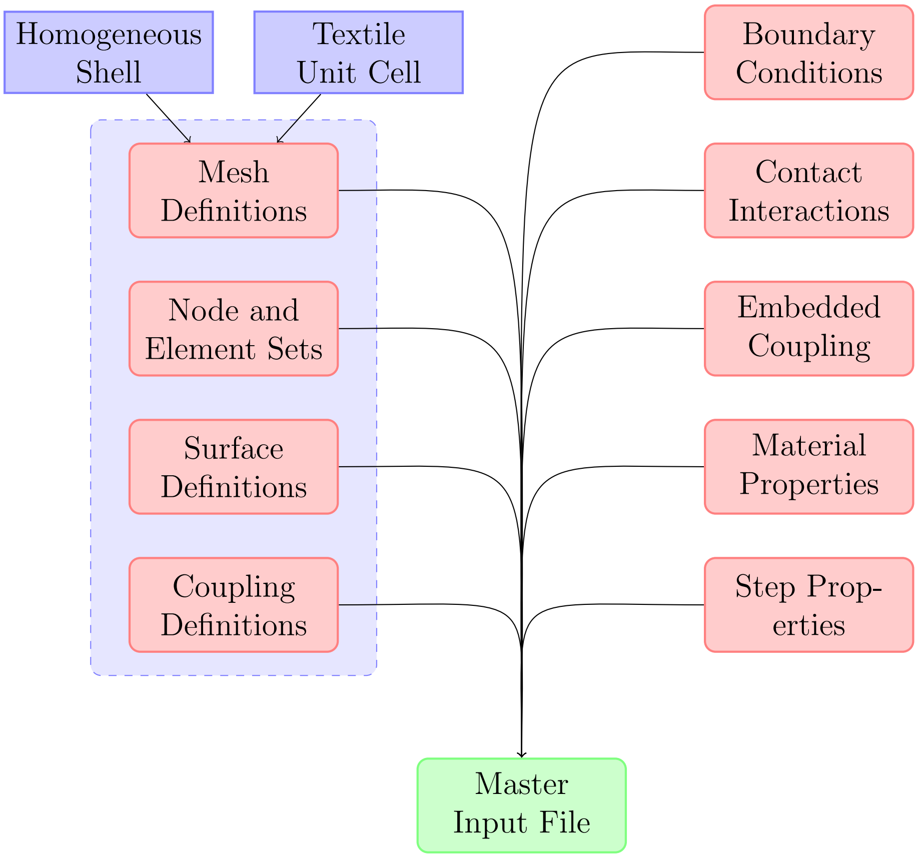
Homogeneous Shell
Textile Unit Cell
Mesh Definitions
Node and Element Sets
Surface Definitions
Coupling Definitions
Boundary Conditions
Contact Interactions
Embedded Coupling
Material Properties
Step Properties
Master Input File

Figure 4.12: Abaqus master input file structure of the models with an embedded domain.

4.2.4 Model Assembly and Mesh Definition

This section covers the positioning of the textile domain within the model, mesh discretization of homogeneous shells and coupling between the textile domain and homogeneous domain. The principle shown here applies for all models including a textile domain, i.e. the model with an embedded domain of two or four layers.

The laminate structure with a homogeneous representation is build around the textile domain which is present only at the region of interest, i.e. where the delamination takes place regarding the introduced loading conditions. As illustrated in Fig. 4.13 and 4.14, the initial crack reaches into the textile domain. The crack tip is placed one and a half tow width (3.63 mm) from the edge of the domain to minimize any influence by mesh change and coupling between the domain and surrounding homogeneous domain. The rest of the model is identical to the reference model in terms of geometry, boundary and loading conditions that were discussed in Section 4.1.4 and can be seen on Fig. 4.13 and 4.14.

The model is built around the textile domain. All shell elements in the homogeneous domain have a reduced integration form (noted as S4R elements). The main criterion when constructing and positioning shells around the domain is following a consistent embedding approach. The laminate is divided in three main areas, i.e. in front of,

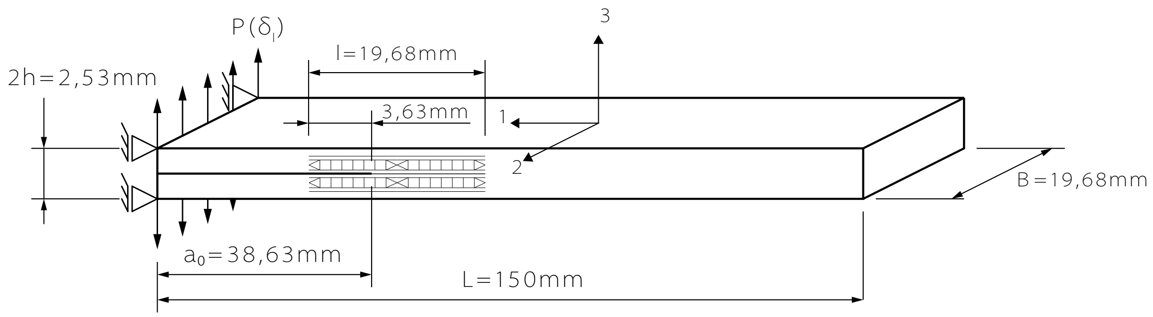

Figure 4.13: Double Cantilever Beam embedded domain model geometry, boundary and loading conditions (not to scale).

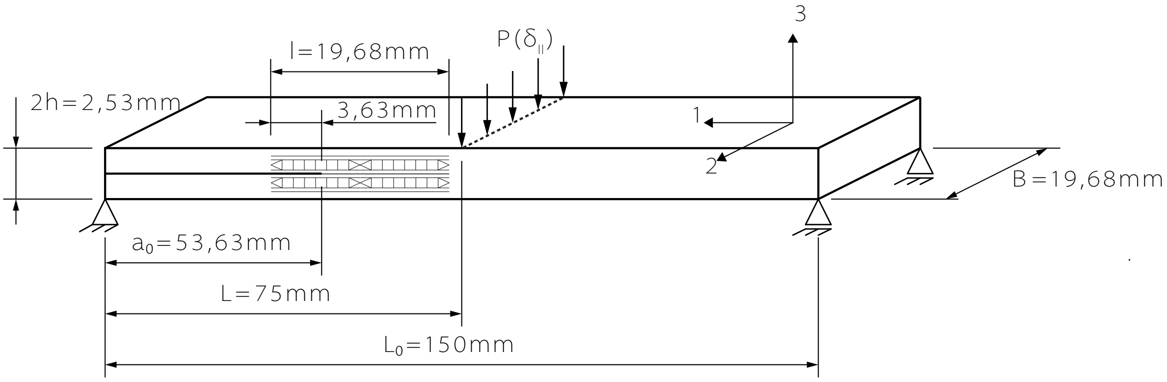

Figure 4.14: Three point End Notch Flexure embedded domain model geometry, boundary and loading conditions (not to scale).

at the and behind the textile domain. At each area a corresponding number of shell reference planes is placed due to boundary conditions and coupling between the textile domain and the homogeneous domain. Note that boundary and loading condition can only be applied at nodes which are not defined as slave nodes in any of coupling definition, as they are already linked to the corresponding master nodes. The same applies for nodes that are in tie constrains or nodes in contact interaction.

Above and below the textile domain there are two shell reference planes, each on one side. Depending on the number of layers within the textile domain, they are assigned with two or one unit cell thickness, resulting in total laminate thickness of 6six plies. The number of elements in the homogeneous domain in width is set to match the textile domain mesh density. In this area it is important to have similar mesh in homogeneous domain and textile domain's matrix, which are tied together, due to the stress distribution over different section in the model.

The area right from the textile domain (in Fig. 4.14) is discretizied with three equal shell reference planes with matching meshes. The number of elements across the width of the model is set to 20 and across the length of 80. The middle shell is assigned as the master surface in tie constraint relation to the top and bottom shells.

Modelling the area in front of the textile domain takes a different approach as it has greater influence on the response of the laminate. Since in this area there is an initial crack the upper and lower part of the laminate are modelled separately. Two shell layers are set to discretizate an individual half of the laminate, one is aligned with the homogeneous shell layers above the textile domain and another that is aligned with the tow layer of the textile domain, as can be seen on Fig. 4.15 where the shell thickness assignments of the homogeneous domain are illustrated with dashed arrows. Note that in case of the EMB2 model, the inner homogeneous shell layer in front the textile domain is aligned with a pair of tow layers. In fact, the placement and thickness assignments of all homogeneous shell layers are slightly different in the models with a two and a four layer textile domain, while the mesh discretization remains the same. Circles in Fig. 4.15 represent section edges not nodes. The outer homogeneous shell layers in front of the textile domain are meshed with 40 elements in width and 100 elements in length, whereas the inner homogeneous shell layers have a coarser mesh of 20 elements in width and 50 in length. Note that contact is established between the inner shells in the ENF simulation, making a significant computational effort to the solution. Additionally, the contact between the inner bottom homogeneous shell layer and the matrix shell from the textile domain is formed when the plies slide over each other. The more refined surface (matrix shells) should act as a slave to ensure better performance and accuracy (which is another reason for a coarser mesh in the inner homogeneous shell layers). All contacts are formulated as frictionless hard contact (see Section 3.1.2).

Edge-based surfaces are generated for each homogeneous shell layer as well as for each layer in the textile domain. Aligned features are coupled via these surfaces as node-to-surface tie constraints, constrained with only the corresponding edge nodes from each feature. In Fig. 4.16 they are illustrated as rounded rectangles. Parallel planes are coupled via surface-to-surface tie constraints between the rest of the corresponding nodes (double sided arrows in Fig. 4.16), an exception is the inner homogeneous shells in front of the textile domain, which interact through contact.

The EMB2 model is presented in Fig. 4.17, with an enlarged side view of the embedded domain. Note that shell's thickness is rendered only in the homogeneous domain to give a better presentation of the mesh discretization. Identical as in the reference model, homogeneous shell layers are assigned with composite shell section, where the number of layers is set accordingly.

Even with the embedding approach and other efforts to make the model numerical efficient, the size of it is still significant in terms of computational power required to run a simulation. Table 4.3 shows a comparison between all three models for the ENF simulation in terms of number of elements and degrees of freedom.

Table 4.3: Mesh size comparison - ENF simulation

Model	**Elements**	**DOFs**
Reference	9700	118806
EMB2	70985	547260
EMB4	119375	831156

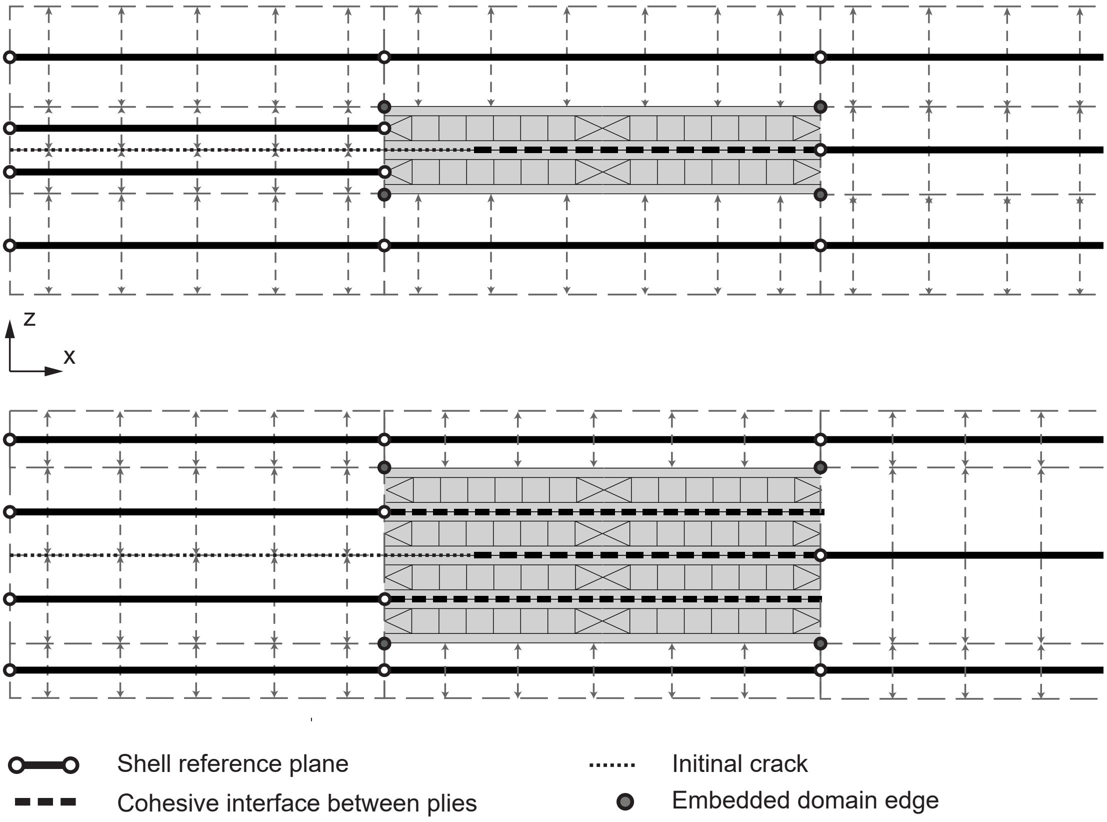
z
x
Shell reference plane
Cohesive interface between plies
Initinal crack
Embedded domain edge

Figure 4.15: Cross section of a EMB2 (top) and EMB4 (bottom) model showing shell reference plane layout and their thicknesses. Homogeneous shell thicknesses are indicated with dashed arrows.

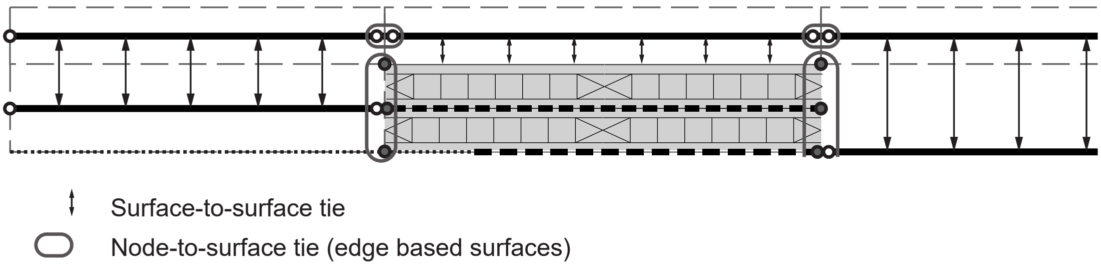
Surface-to-surface tie
Node-to-surface tie (edge based surfaces)

Figure 4.16: Cross section of a EMB4 model showing the embedding approach.

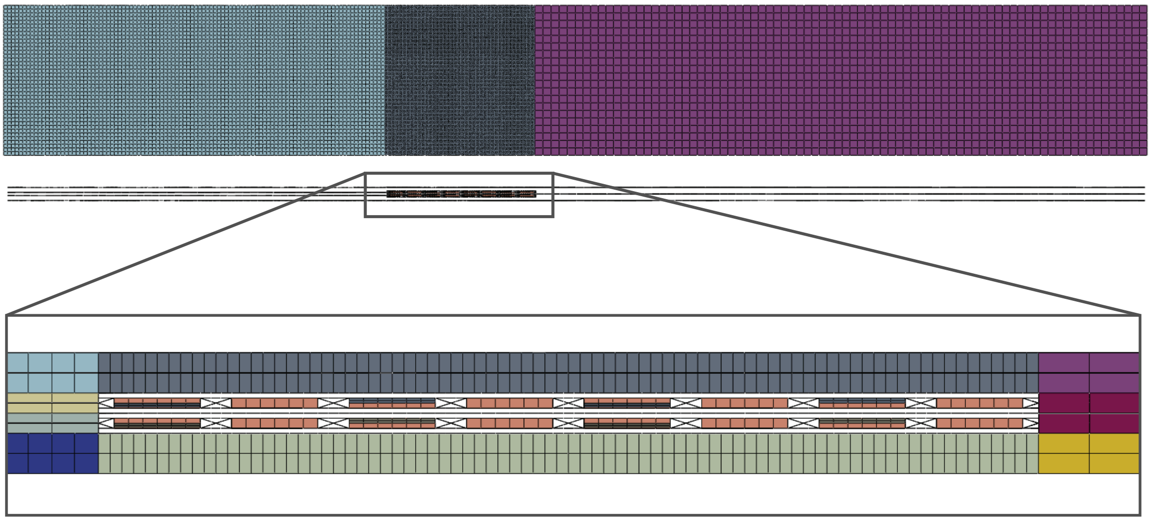

Figure 4.17: Mesh discretization of the EMB2 model. In the bottom figure the shell thickness is rendered only for the homogeneous domains.

4.3 Analysis Control

Non-linear FEM analyses are often challenging to perform and are associated with convergence issues. Material models including softening behaviour can cause convergence difficulties in the analysis. This is the case with the damage modelling in cohesive elements. Several methods can be used to minimize these effects. Viscous regularization of the constitutive equations (assigned to cohesive elements) causes the tangent stiffness matrix of the softening material to be positive definite for a sufficiently small time increment. It effectively permits the stress to be outside the limits defined by the applied traction-separation law. Using viscous regularization with small value of the viscosity parameter μ (small compared to the characteristic time increment) improves convergence in the softening stage, without compromising results.

The viscous parameter (i.e. the relaxation time) was set to $\mu = 10^{-6}$ s for most of the simulations. The accuracy of the solution with viscous regularization can be checked by comparing the viscous dissipation energy (in Abaqus defines as ALLCD) and recoverable strain energy (ALLSE) that is stored in the model. If the viscous dissipation energy is significantly smaller than the recoverable strain energy in the model, the accuracy of the solution is not effected by the viscous regularization.

In strongly non-linear problems the Newton algorithm used in implicit analysis may diverge during equilibrium iteration. The line search algorithm helps to improve robustness of the Newton or quasi-Newton method. During equilibrium iterations where residuals are large, the line search algorithm scales the correction to the solution, which helps to prevent divergence [21]. The line search algorithm is activated in models with an embedded domain, where the delamination process is highly non-linear.

5 Computational Results

In the present chapter, the results of FEM simulations are presented. Numerical results of models with an embedding textile domain are compared to simulation results of the reference model and analytical results for mode I and II load cases. For each simulation, the load-displacement response is investigated with emphasis on the delamination progress. The delamination process is reviewed step by step and correlations with the topology of the models are made.

Postprocessing of the simulation was done using Abaqus Viewer and Python scripts developed in course of this work.

5.1 Double Cantilever Beam Simulations

The results of the mode I load case, i.e. the DCB simulation, are presented as load-displacement curves in Fig. 5.1. The EMB2 model is compared to the reference model and the analytical solution given by the corrected beam theory (CBT). The initial response before the delamination propagation shows that the numerical models are behaving less stiff than the analytical prediction. The effect can be attributed to the fact, that cohesive elements by their bi-linear constitutive law actually deform prior to the damage evolution. This can be seen in Fig. 3.4 as the elastic deformation δ_e at which the maximum traction t_{max} is achieved. The reference model predicts the initial stiffness in better agreement with the analytical solution than the EMB2 model due to its absence of coupling between different model domains and the fact that the analytical solution is considered for a UD composite material.

Both the reference and the EMB2 models predict the behaviour during the delamination in a good agreement with the corrected beam theory. While the reference model slightly over-predicts the reaction force in this regime compared to the analytical solution, the EMB2 model shows an interesting result, which indicates that the delamination process in woven composites is not a steady phenomena, as the value of the reaction force has significant drops at certain displacements. This can be clearly seen on enlarged sub-figure in Fig. 5.1.

The EMB4 model is not included in Mode I load case comparison due to the fact that it is not expected that having additional parallel interfaces in the model would have a significant influence on the response of the model during the mode I load case. The

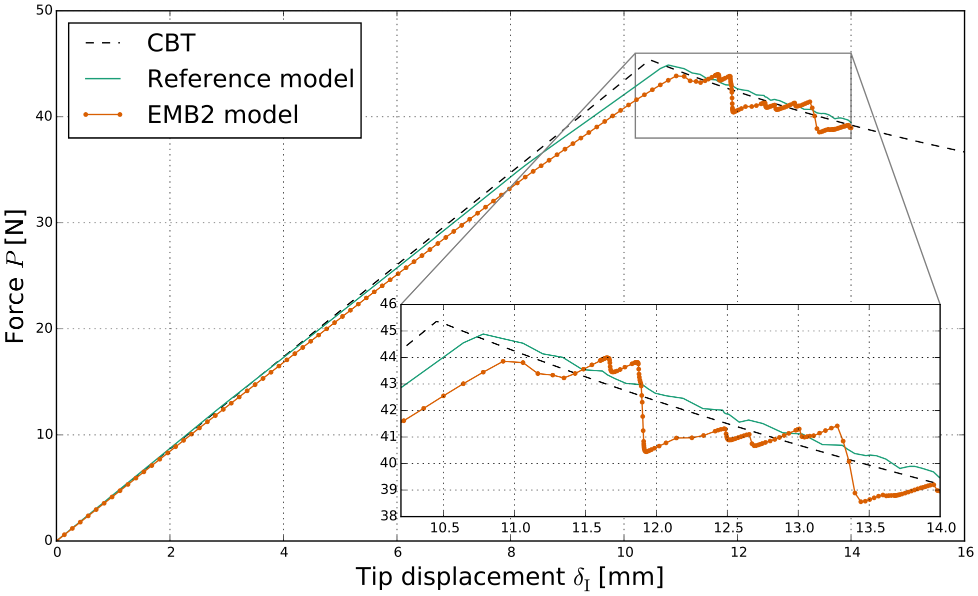

Figure 5.1: Load-displacement curves for the DCB simulation. An enlarged view of the delamination onset is presented in the bottom right corner.

reason why, is that for mode I load case, the traction in cohesive elements only reaches a critical value in the interface where the initial crack lies (considering the material properties use in this work). However this is only true as long as there are no damage parameters in other components of the model (e.g. tows and matrix).

Evaluating the reaction force and the tip displacement is straightforward, but for further analysis the crack growth is of particular importance. Thus, evaluating the crack length is discussed in the next section, where the delamination onset is described in greater detail.

5.1.1 Crack Front Propagation Evaluation

In the DCB experiments, the crack length is usually measured by means of high speed camera and a measuring tape. In FEM simulations it can be evaluated via the damage parameters that are presented in Section 3.2.1

From the numerical perspective, a crack in a laminate would exist anywhere in the interface, where the interface integration points are fully damaged and cannot hold any load. In Abaqus the SDEG parameter stands for scalar stiffness degradation which represents the degradation parameter d. It takes values between 0 and 1, the latter being a completely damaged integration point. For individual mode I or mode II load case this happens when the degradation parameter reaches value of 1, thus resulting in total stiffness degradation $(1-d)\,K=0$ (see Fig. 3.4). In a mixed-mode load case this would be the fully debonded locus that is illustrated on Fig. 3.5, which represents Eq. (3.3) when the Benzeggagh-Kenane criterion is used, as is the case in the present work.

A completely damaged cohesive element contains only integration points, that are completely degraded. In Abaqus these elements can be deleted or removed to indicate the prediction of the crack front. Figure 5.2 shows the damage initiation criterion QUADSCRT and damage evolution criterion SDEG in the interface of the reference model. Note that the model is mirrored over the symmetry plane to give a full width presentation. On the side of each figure there is a presentation of the bilinear traction-separation law with indications where each of the damage criterion takes minimum and maximum values.

The completely damaged elements have been deleted, which indicates that the delamination front takes shape of a slight arc, rather than a straight line. Crack length is determined by means of counting the number of completely damaged centroids (a virtual point in the centre of the element that takes an average value of all element's integration points) and dividing it with the number of elements in width, which gives us an average value of the crack length. Such an approach gives a prediction in good agreement with the corrected beam theory, which can be seen on Fig. 5.3 where the

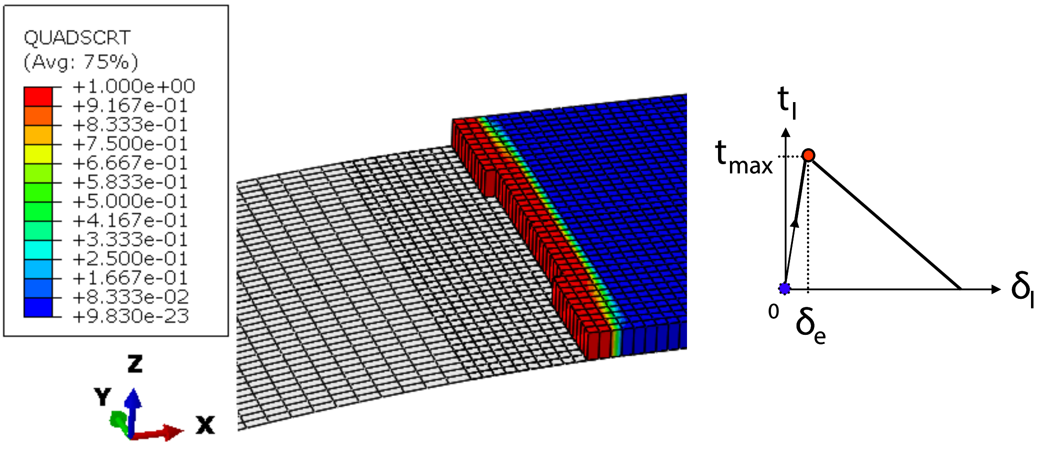
QUADSCRT
(Avg: 75%)
+1.000e+00
+9.167e-01
+8.333e-01
+7.500e-01
+6.667e-01
+5.833e-01
+5.000e-01
+4.167e-01
+3.333e-01
+2.500e-01
+1.667e-01
+8.333e-02
+9.830e-23
Z
Y
X
t_I
t_{max}
δ_I
0
δ_e

(a) Damage initiation criterion - QUADSRT.

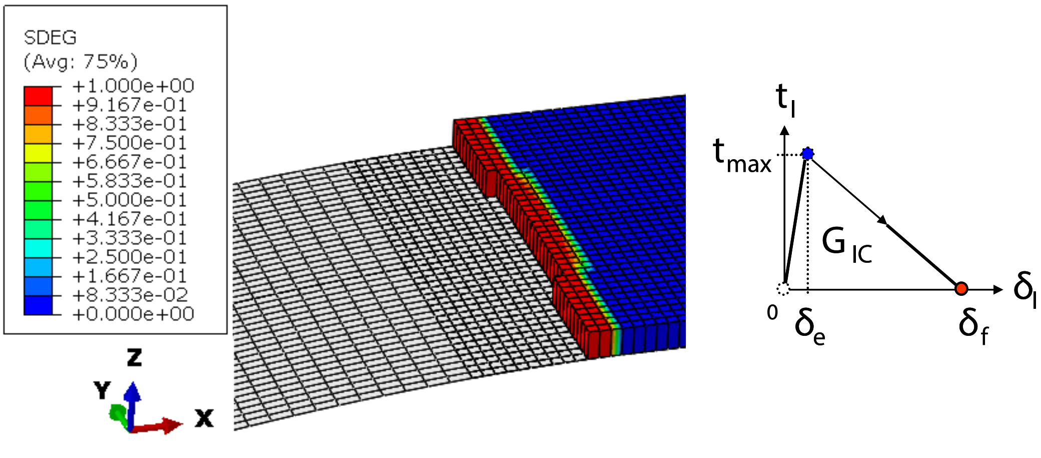
SDEG
(Avg: 75%)
+1.000e+00
+9.167e-01
+8.333e-01
+7.500e-01
+6.667e-01
+5.833e-01
+5.000e-01
+4.167e-01
+3.333e-01
+2.500e-01
+1.667e-01
+8.333e-02
+0.000e+00
Z
Y
X
t_I
t_{max}
G_{IC}
δ_I
0
δ_e
δ_f

(b) Damage evolution criterion - SDEG.

Figure 5.2: Damage criterion for the reference model in the DCB simulation at tip displacement of 14 mm. The QUADSCRT parameter is presented by Eq. (3.1) and the SDEG parameter by Eq.(3.3). Fully damaged elements are deleted.

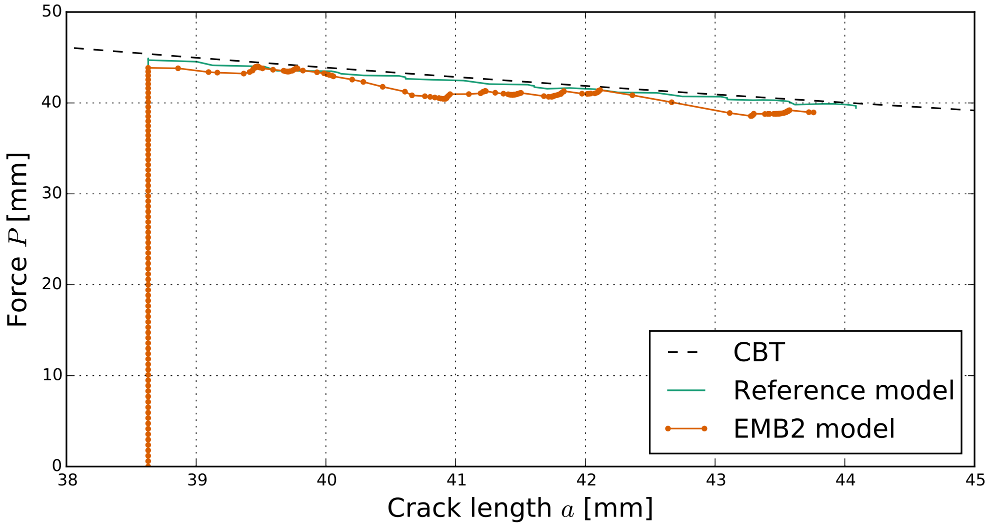

Figure 5.3: Load versus crack length relation in the DCB simulation.

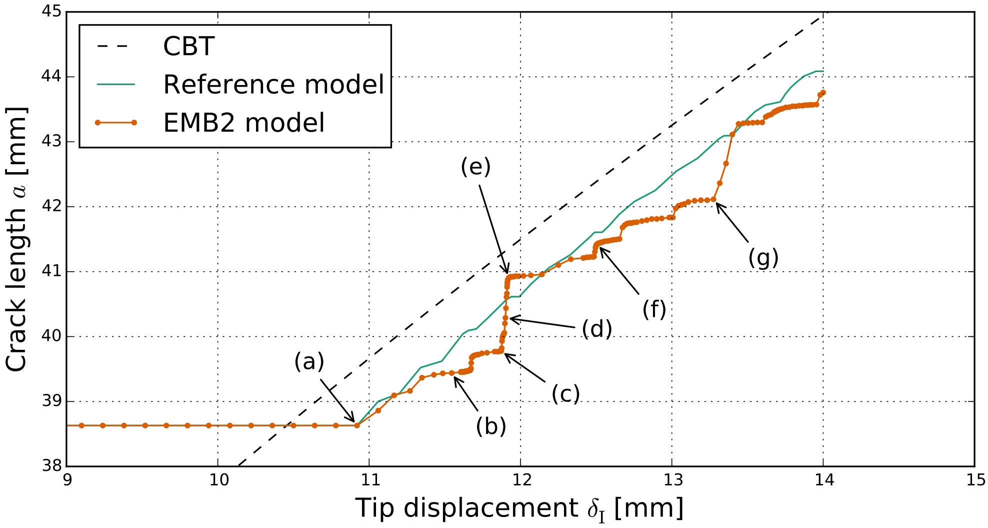

Figure 5.4: Crack propagation in relation to the tip displacement in the DCB simulation.

load versus crack length relation is presented for both the reference model and the EMB2 model.

A better presentation of the crack propagation is given in Fig. 5.4, where the crack length a is plotted in relation to the tip displacement δ_I. Since the DCB simulation is displacement controlled this gives us a good indication of crack propagation speed during the delamination. Both models develop damage evolution at slightly higher value of tip displacement than the analytical model. In the reference model the crack is progressing in a constant manner, whereas in the EMB2 model, the crack is propagating in steps. This indicates that there are different crack propagation speeds over certain areas in the model. To identify the key points in the crack propagation, several annotations are added to Fig. 5.4, which are correlated to Fig. 5.6 showing delamination progress during the DCB simulation in the EMB2 model.

For a better presentation, let us first define two different areas in plies which have an important role when discussing delamination in woven laminates. Figure 5.5 shows the definitions for the area of tows (coloured with blue) and the area of matrix pockets (coloured with red). The area of tows is the region where individual ply is reinforced with tows throughout the area, while the rest of the ply have areas with matrix pockets. The interface which is laid between two plies is influenced by these areas, which is demonstrated next.

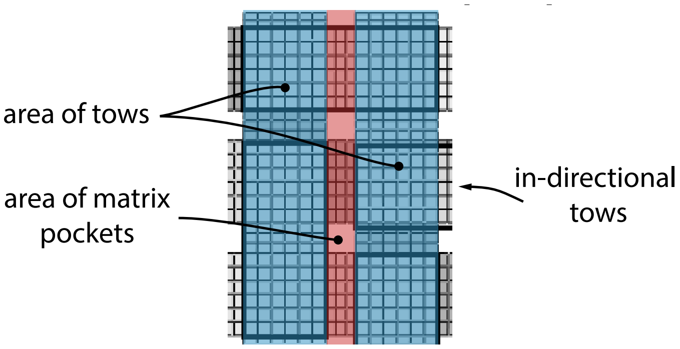

Figure 5.5: Area definition in the EMB2 model. The blue area represents the area of tows and the red one the area of matrix pockets.

Figure 5.6 shows a sequence of damage initiation (QUADSCRT) in the interface of the EMB2 model for each step that is annotated in Fig. 5.4. Only the completely damaged elements are removed to give an approximate representation of the crack front at each tip displacement step. Note that the elements on the crack front are partly damaged, i.e. the nodes on the crack front are completely degraded while others are not. Additionally, for each step a tip displacement and an average crack length is noted. In each figure the horizontal sections of tows in the first (bottom) layer that are adjacent to the interface are illustrated by thick black rectangles. The same concept is used for all simulation results.

Similar to the reference model, the delamination front is shaped in a slight arc. The sub-figures in Fig. 5.6 shows how the damage initiation is influenced by the model's textile topology. Figure 5.6h illustrates the pattern of horizontal tow sections adjacent to the interface. The first layer is below the interface and the second is above it. Tows within a single textile ply have two levels, to which they change at the intersections, creating the woven topology. The effects of such structure are most visible in Fig. 5.6a, where the damage initiation tends to developed faster over the areas where tows of either layer are next to the interface rather than over the area of matrix pockets, however the differences are quite small (1 element's length). The damage evolution on the other hand is not affected in the same scale as can be seen by the shape of the crack front. The largest jump in the crack length (Fig. 5.6) happens from point (*c*) to point (*e*). These points are presented in Figs. 5.6c and 5.6e, respectively.

The correlation between these figures indicates that the delamination process propagates quickest over the area of tows. Figure 5.6c, representing the start of the crack jump, shows that the damage initiation is already present in the interface area of tows

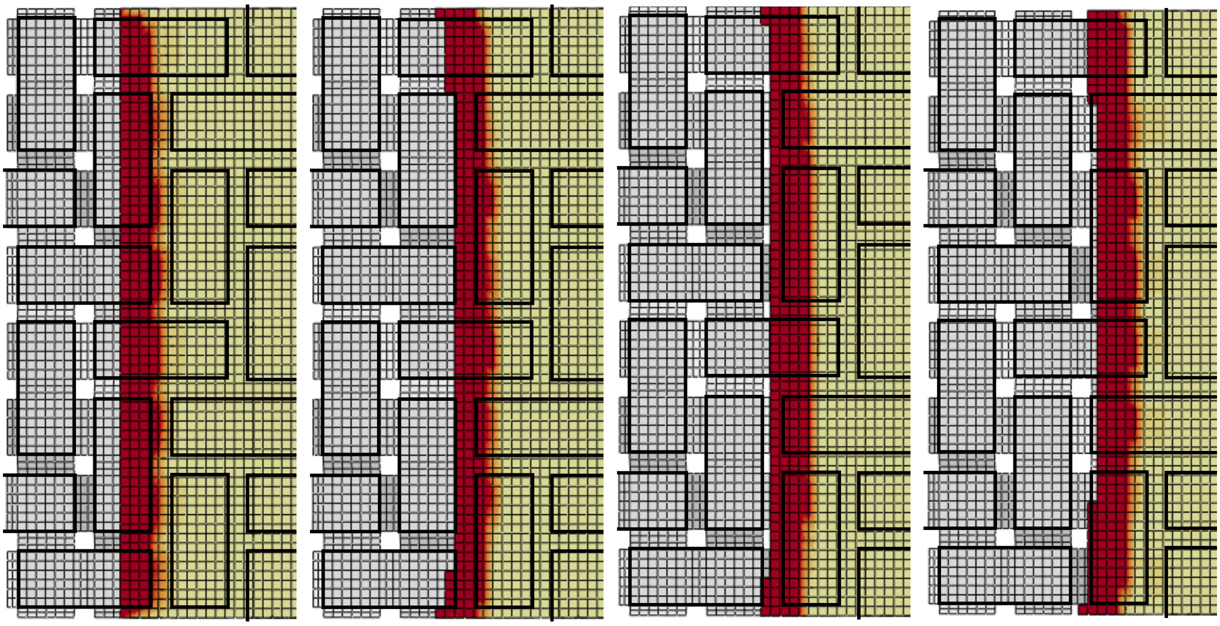

(a) δ_{I} =10.92 mm
a =38.63 mm

(b) δ_{I} =11.55 mm
a =39.44 mm

(c) δ_{I} =11.87 mm
a =39.78 mm

(d) δ_{I} =11.90 mm
a =40.29 mm

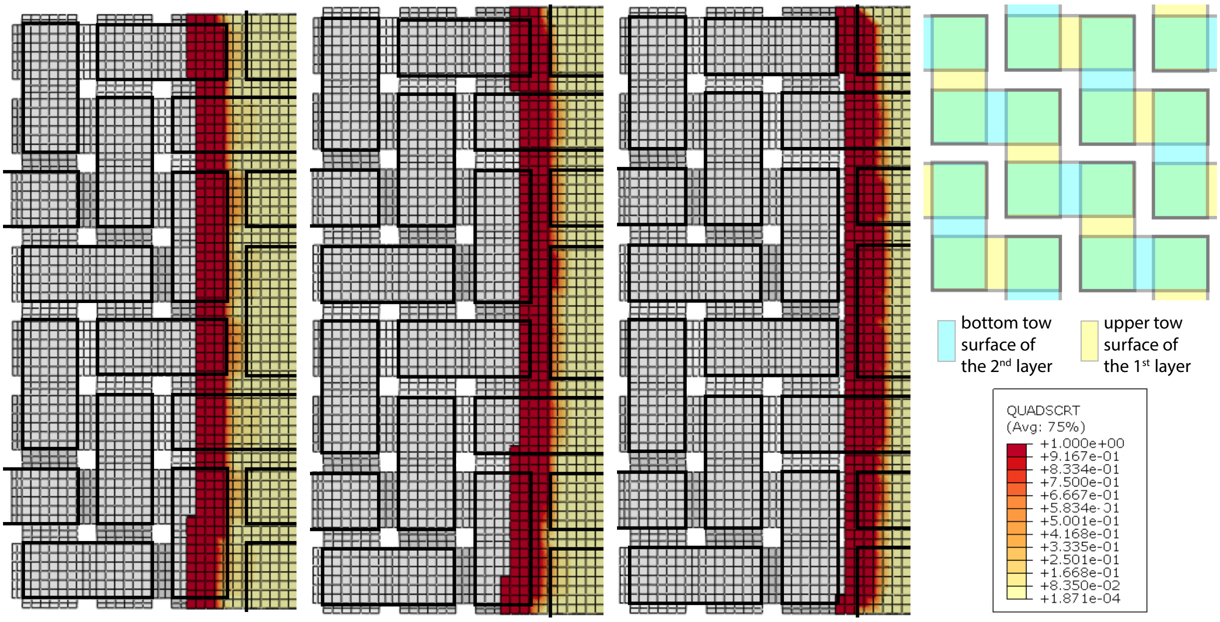

(e) δ_{I} =11.92 mm
a =40.9 mm

(f) δ_{I} =12.51 mm
a =41.43 mm

(g) δ_{I} =13.28 mm
a =42.11 mm

(h)

Figure 5.6: Delamination progress during the DCB simulation in the interface of the EMB2 model. Horizontal sections of the first layer's tows adjacent to the interface are illustrated with outlined rectangles.

and the element degradation is very close to the edge of it (the edge of the interface already represents completely degraded nodes). After this point the delamination process moves quickly over almost the whole of the area of tows, stopping at the point where the damage initiation reaches the next area of matrix pockets - Fig. 5.6e. This area has a significantly lower stiffness, due to the lack of the reinforcing tows and the matrix having lower Young's modulus than the reinforcing phase, i.e. tows (see Table 4.2). Consequently this area of matrix pockets elastically deforms more than the area surrounded by tows under the same load. Therefore a larger part of the external energy goes into elastically deforming the laminate over this areas. Similar effect is repeated at the next area of tows - Fig. 5.6g, which indicates that the delamination process in woven laminates is influenced by the local stiffness inside the laminate.

Although the DCB test is designed to measure mode I delamination (in UD composites), the mixed-mode delamination onset is not entirely excluded in textile laminates because of their woven ply topology. Figure 5.7 shows mode mix ratio during the damage initiation (MMIXDMI) and evolution (MMIXDME) at a tip displacement of δ_{I} =11.55 mm. Both parameters are defined as $1 - m_1$, where m_1 stands for the contribution of mode I damage initiation or evolution to the total damage initiation or evolution, respectively. This means that pure mode I delamination takes value of 0. Prior to any damage initiation or evolution the integration points take value of -1. From Figure 5.7a we can see that over the areas where both the first and second layer tows change their level, a mixed-mode damage initiation occurs. At these elements, the integration points take values up to 0.5, which means only half of the damage initiation is contributed by mode I. Since the interface strength and critical energy release rate of mode II delamination have higher values than mode I, this also means that these elements have a higher value of traction than others where there is no mixed-mode damage initiation. The cohesive zone method, implemented in the Abaqus/Standard processor, takes the mixed-mode critical energy release rate, which is higher than in pure mode I, for the evaluation of the damage evolution. This effect additionally slows down the delamination process in areas of matrix pockets (crack front in Fig. 5.6c) where tows from the first and second layer change their level. At these local areas the interface has a higher critical energy release rate than in the interface area surrounded only by tow sections, because of the mix-mode damage initiation.

However, Fig. 5.7b shows that the damage evolution over the whole interface is effectively caused by mode I delamination only. Note that the MMIXDME parameter in the process zone changes during the delamination. Although Fig. 5.7b indicates slight mix mode damage evolution in a couple of areas, the values before total stiffness degradation indicate that the damage evolution is caused by mode I delamination.

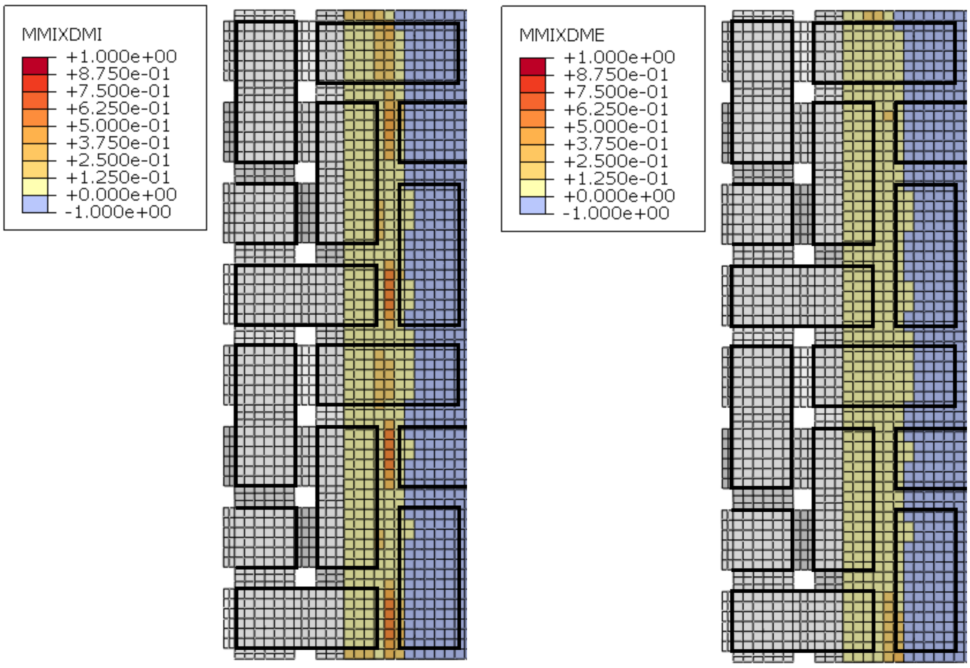
MMIXDMI
+1.000e+00
+8.750e-01
+7.500e-01
+6.250e-01
+5.000e-01
+3.750e-01
+2.500e-01
+1.250e-01
+0.000e+00
-1.000e+00
MMIXDME
+1.000e+00
+8.750e-01
+7.500e-01
+6.250e-01
+5.000e-01
+3.750e-01
+2.500e-01
+1.250e-01
+0.000e+00
-1.000e+00

(a) Mode mix ratio during damage initiation.

(b) Mode mix ratio during damage evolution.

Figure 5.7: Mode mix ratio during the delamination in DCB simulation of the EMB2 model at δ_{I} =11.55 mm. Values are set to -1.0 prior damage initiation or evolution.

5.1.2 Fracture Resistance Curve (R-Curve)

Resistance to the delamination in laminated composites is measured in terms of energy released per unit crack growth, i.e. energy release rate. There are several data reduction techniques to evaluate the energy release rate. A brief comparison between the common ones can be found in Appendix 8.1. For the purposes of this work, the corrected beam theory approach is used as described in Chapter 2.

Figure 5.8 shows the R-curve for both the reference and the EMB2 model. On the right side a part of the load-displacement curve (Fig. 5.1) is presented for a better representation of the annotation points for the EMB2 model. Both models predict the energy release rate during delamination in a good agreement with the defined critical energy release rate of the interface in mode I as $\mathcal{G}_{I_c} = 0.7\,\mathrm{N/mm}$.

In the EMB2 model, the energy release rate gradually drops during the crack propagation from point (*c*) to point (*e*). This is the area where the crack propagates the fastest regarding to the tip displacement increase. Referring back to the area definition of the energy release rate (Fig. 2.4 in Chapter 2), the gradual drop of the energy release rate can be correlated to the load displacement curve in Fig. 5.8. The area that defines the energy release rate is getting smaller for each consecutive increment in this region, however this can only be an assumption, because for defining the area of the energy release rate, the model would have to be loaded and unloaded at each increment or for certain value of crack growth.

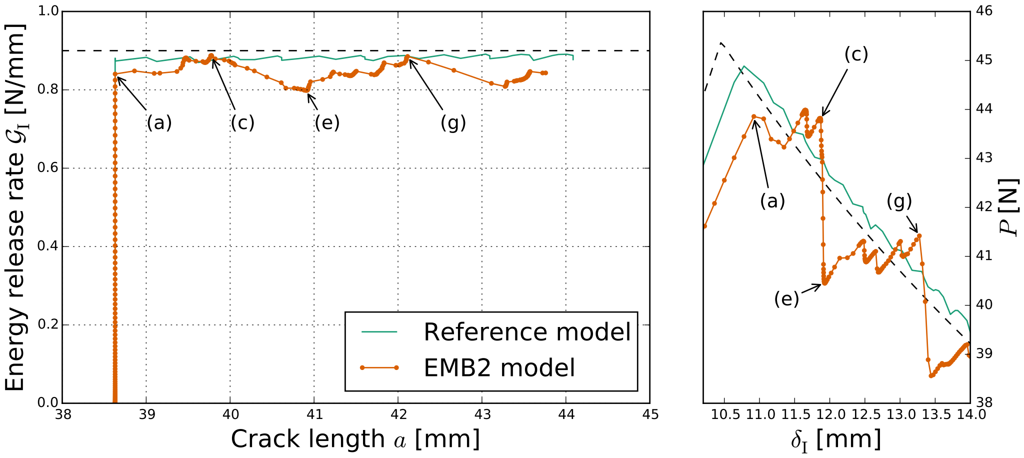

Figure 5.8: Fracture resistance curve (R-curve) for mode I delamination. The right figure shows the delamination regime in the load-displacement curve (detail from Fig. 5.1).

As discussed in the previous section, the crack front propagates faster over the area without matrix pockets. In this region, a higher share of the external work goes into damaging the cohesive elements in the interface and less into locally deforming tows in the textile domain than otherwise. When the critical energy is achieved, the measured energy release rate has a smaller share of the strain energy release rate from the locally deformed tows and matrix (both of them having only linear elastic material properties) compared to the crack front propagation over the area of matrix pocket, where more energy from the external work goes into elastically deforming the matrix. Thus, the energy release rate is gradually rising in this region (from point (e) to point (g)). The process is repeated when the delamination front continues to propagate through the textile domain.

5.1.3 Energy Balance Analysis

Local mechanisms that governs the delamination process in the DCB simulations can be observed by energy-based analysis.

The total amount of energy supplied via the boundary conditions is transferred into internal recoverable energy, damage dissipation energy and energy associated with viscous damping. In Abaqus, the internal recoverable energy is associated with the output variable ALLSE (recoverable strain energy), damage dissipation energy with ALLDMD and energy dissipated by viscous damping with ALLCD and there abbreviations are used in the following figures.

Figure 5.9 shows the energy balance in the EMB2 model regarding the tip displacement (Fig. 5.9a) and crack length (Fig. 5.9b). As mentioned before in Section 4.3, viscous regularization is applied in all simulations. The dissipated energy due to viscous regularization are of order of 10^3 times smaller than the energy dissipated by damage. Therefore the effects of the viscous regularization on the accuracy of the solution can be neglected.

In Fig. 5.9b, the shape of the recoverable strain energy is very similar to the energy release rate in Fig. 5.8. Note that the simulation is tip displacement controlled, which results in uneven crack growth and while the damage dissipation energy grows linearly in relation to crack length, the data points are not distributed evenly. Obtaining the energy release rate from Eq. (**??**) means differentiating a signal with varying differences between the data points, which gives a solution with high gradients.

There is another way of comparing the data reduction techniques with the direct energy output of the material model. The energy release rate evaluated using the corrected beam theory (Fig. 5.8) can be integrated and than compared with the damage dissipation energy distribution with respect to the crack surface. Figure 5.10 compares the damage dissipation energy obtained directly from the EMB2 model with the dissipated energy evaluated by the corrected beam theory. The offset between the two curves is a result of the way the crack length is being evaluated (Section 5.1.1). Only fully damaged centroids (or for that matter elements) are taken into account when evaluating the crack length, while the partly damaged integration points are not. However, they do contribute to the damage dissipation energy. Elements with partly damaged integration points ahead of the crack front can be seen in Fig. 5.2b for the reference model, where the stiffness degradation parameter evaluates how damaged are the integration points. The same is true for the EMB2 model, where the partly damaged integration points ahead of the crack tip (Fig. 5.6) are contributing to the damage dissipation energy. The slope of both curves in Fig. 5.10 represent the rate of change in dissipated energy, which is actually the energy release rate. They are slightly different, the one from the dissipation energy, evaluated with the corrected beam theory, being slightly less steep. Assuming that the area of partly damaged integration points ahead of the crack front (from now on called the process zone) stays the same during the delamination, the slight difference between slopes of the curves reflects the energy release rate

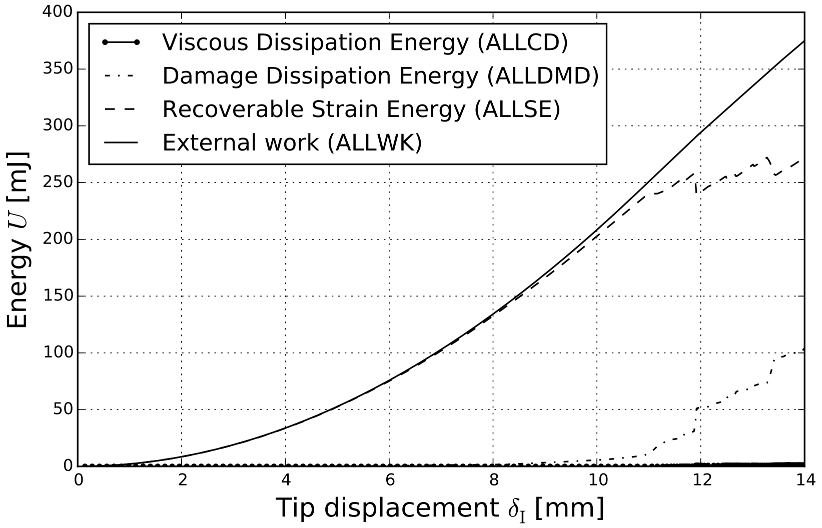

(a)

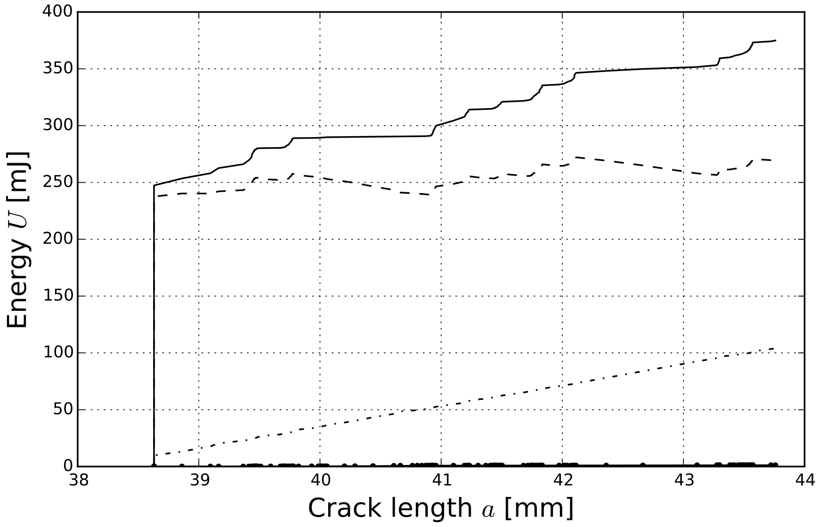

(b)

Figure 5.9: Energy balance of the DCB simulation for the EMB2 model. The top figure shows strain energy and dissipation energy distributions in relation to the tip displacement. The bottom shows the same energies in relation to the crack length.

evaluated by CBT being, in average, slightly lower than the nominal one (black dashed line in Fig.5.10), which should be represented, in average, by the direct energy output ALLDMD. In addition the damage dissipation energy evaluated by the Irwin-Kies (IK) approach (Eq. 8.3) is compared in Fig. 5.10, which gives, in average, a higher energy release rate than the CBT approach.

Additionally, the process zone is slightly changing in shape and size during the delamination. However, this has a small effect on the ALLDMD energy output. The process zone is very challenging to define and quantify, therefore for the purposes of this work it is not investigated in greater details.

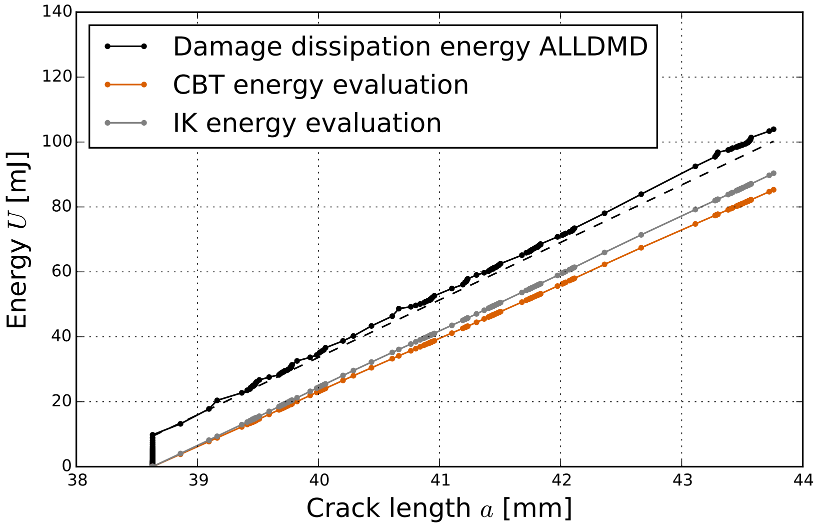

Figure 5.10: Comparison between the damage dissipation energy from the EMB2 model and the damage dissipation energy evaluated by the corrected beam theory (CBT) and the Irwin-Kies (IK) approach in the DCB simulation.

5.2 Three Point End Notched Flexure Simulations

The results of the ENF simulation are presented on Fig. 5.11, where the EMB2 and the EMB4 model are compared to the reference model and the analytical solution for the load-displacement relation. All models have a similar elastic response, which are in a good agreement with the analytical solution given by the corrected beam theory.

The prediction of the delamination onset is slightly different for each model (see the enlarged figure in Fig. 5.11). The prediction of the reference model comes very close to the analytical solution. Note that the transition from the elastic regime to the softening stage (delamination propagation) is quite sudden in a sense that the load drops by a large margin compared to the central displacement increase. Here are the models most effected by the viscous regularization, which enables a converging solution during this highly non-linear transition. Both models with an embedded domain predict the delamination onset at a slightly smaller central displacement δ_{II}. However during the delamination, both models predict similar response, which indicates the mode II delamination in woven laminates is govern by the local effects, similar as is the case in the DCB simulation.

Note that from $\delta_{\mathrm{II}} \geq 17.5$ mm, the predictions from both the EMB2 and EMB4 models take similar values. This is due to the fact that the delamination process is close to the edge of the textile domain, which means the results are heavily influenced by the

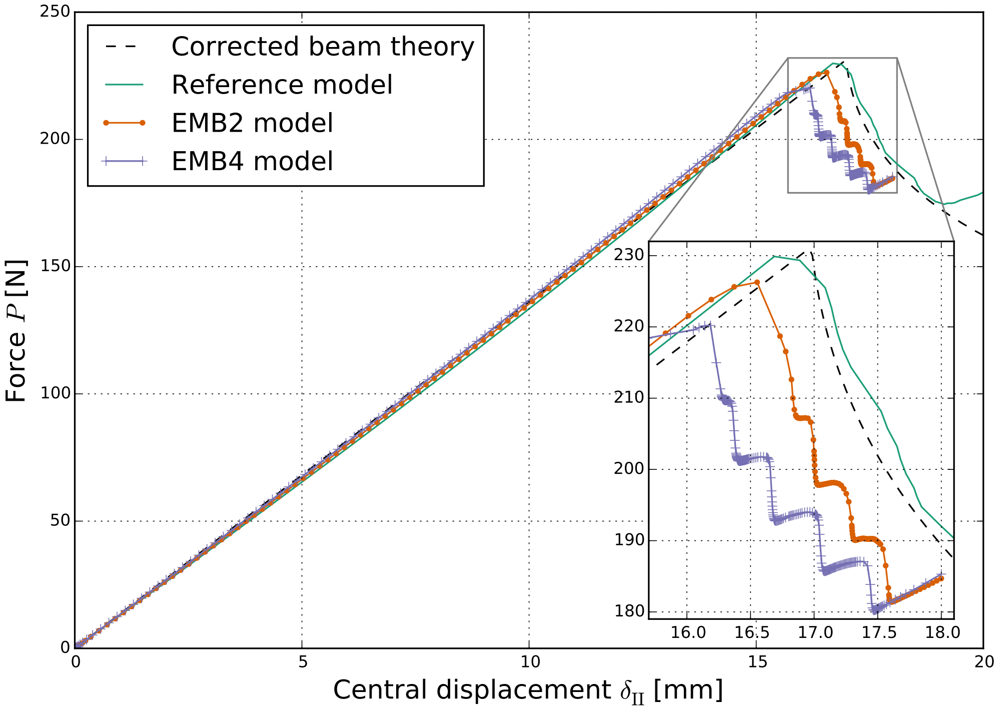

Figure 5.11: Load-displacement curves for the ENF simulation. An enlarged view of the delamination onset is presented in the bottom right corner.

embedding of the domain. Thus, the analysis of the delamination is only done in the region, where the delamination is not significantly influenced by the embedding. More on this is discussed in the next section.

5.2.1 Crack Front Propagation Evaluation

The crack growth is evaluated by the same technique as in the DCB simulation (see the Section 5.1.1).

A prediction of the load versus crack length is given by the Fig. 5.12 for each numerical model. The figure shows that the crack measuring technique, used in the present work, gives a suitable representation of the crack length compared to the one from the corrected beam theory.

Since the ENF test is displacement controlled, the relation between the central displacement and the crack length, given by the Fig. 5.13, reveals more interesting results. From this figure it can be evaluated that the delamination onset in the EMB4 model happens at approximate 0.5 mm lower values of central displacement than in the EMB2 model. Again, the crack length prediction from $\delta_{\mathrm{II}} \geq$17.5 mm on equals for both models, which is caused by the fact that the damage initiation reaches the edge of the textile domain and the crack front propagation is slowed down it until eventually stops towards the edge of the interface. The results from the enlarged section in Fig. 5.13 are not significantly influenced by this edge effect, as the delamination process is still far enough from the edge of the textile domain. The key points in the crack propagation for both the EMB2 and EMB4 are identified with annotation points, which are correlated with the Fig. 5.14 and Fig. 5.16, respectively. At both models the annotation points correlate to the similar crack front position regarding the surrounding tows in the textile domain.

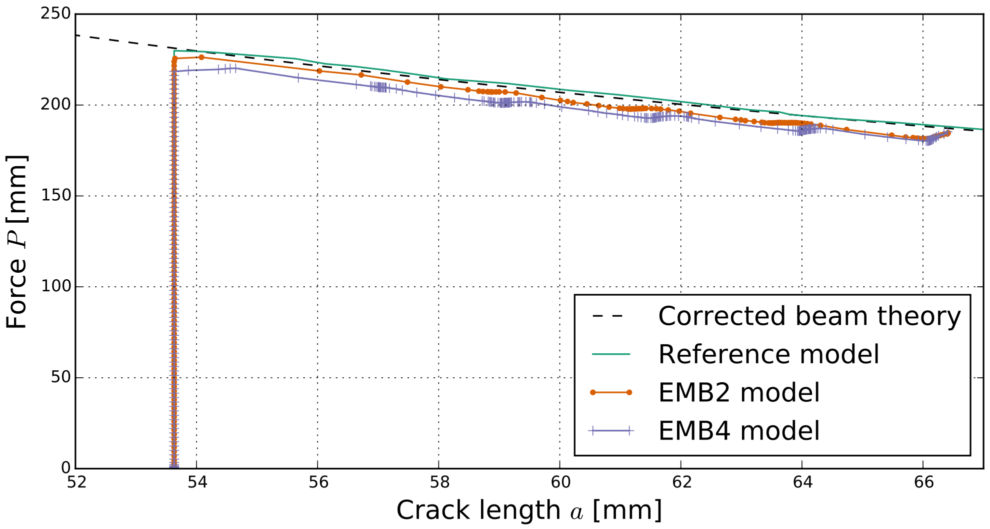

Figure 5.12: Load versus crack length relation in mode II delamination for the reference, EMB2 and EMB4 model.

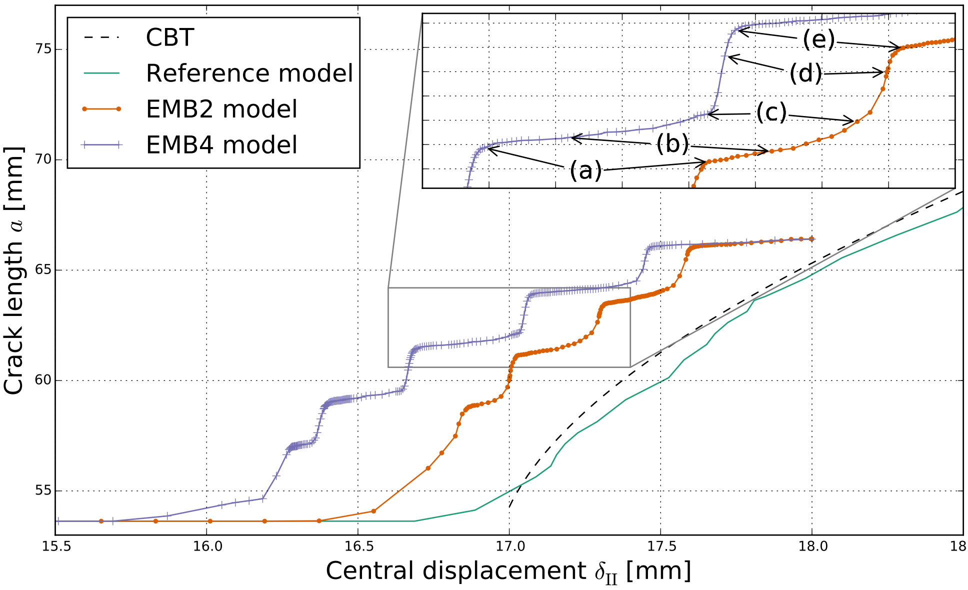

Figure 5.13: Crack propagation in relation to central displacement for mode II delamination. The reference, EMB2 and EMB4 models are compared.

The crack front propagation evaluation is first presented for the EMB2 model and then for the EMB4 model, where the differences regarding the crack front propagation between both models are also discussed.

5.2.1.1 EMB2 model

Figure 5.14 shows a sequence of the damage process in the interface of the EMB2 model during the ENF simulation. The sub-figures are correlated to the annotation points in Fig. 5.13 for the EMB2 model.

During the mode II delamination, the process zone in the interface changes in shape and size. The influence of tows layout on damage initiation is quite significant, which is illustrated in Fig. 5.14 by the shape of the damage initiation (QUADSCRT) area. Note that the thick rectangles outline the tow surfaces of the bottom ply, which are adjacent to the interface. The tow surfaces from the upper ply are shifted by a distance of two tows width and two matrix pockets width (see Fig. 5.6h). The EMB2 model predicts that the damage in the interface is initiated faster in the area, where the tow surfaces in the direction of delamination onset, from either layer, are adjacent to the interface. This areas have a higher local stiffness compared to the remaining ones, due to the higher tow's Young's modulus, which transfers more energy into deforming the interface, rather than the surrounding material. This corresponds to the conclusions made for the DCB simulation, where the delamination is influenced by the local geometry and stiffness.

The shape of the crack front is not effected in the same manner as the damage initiation. A plausible explanation would be, that the differences in local stiffness are very small.

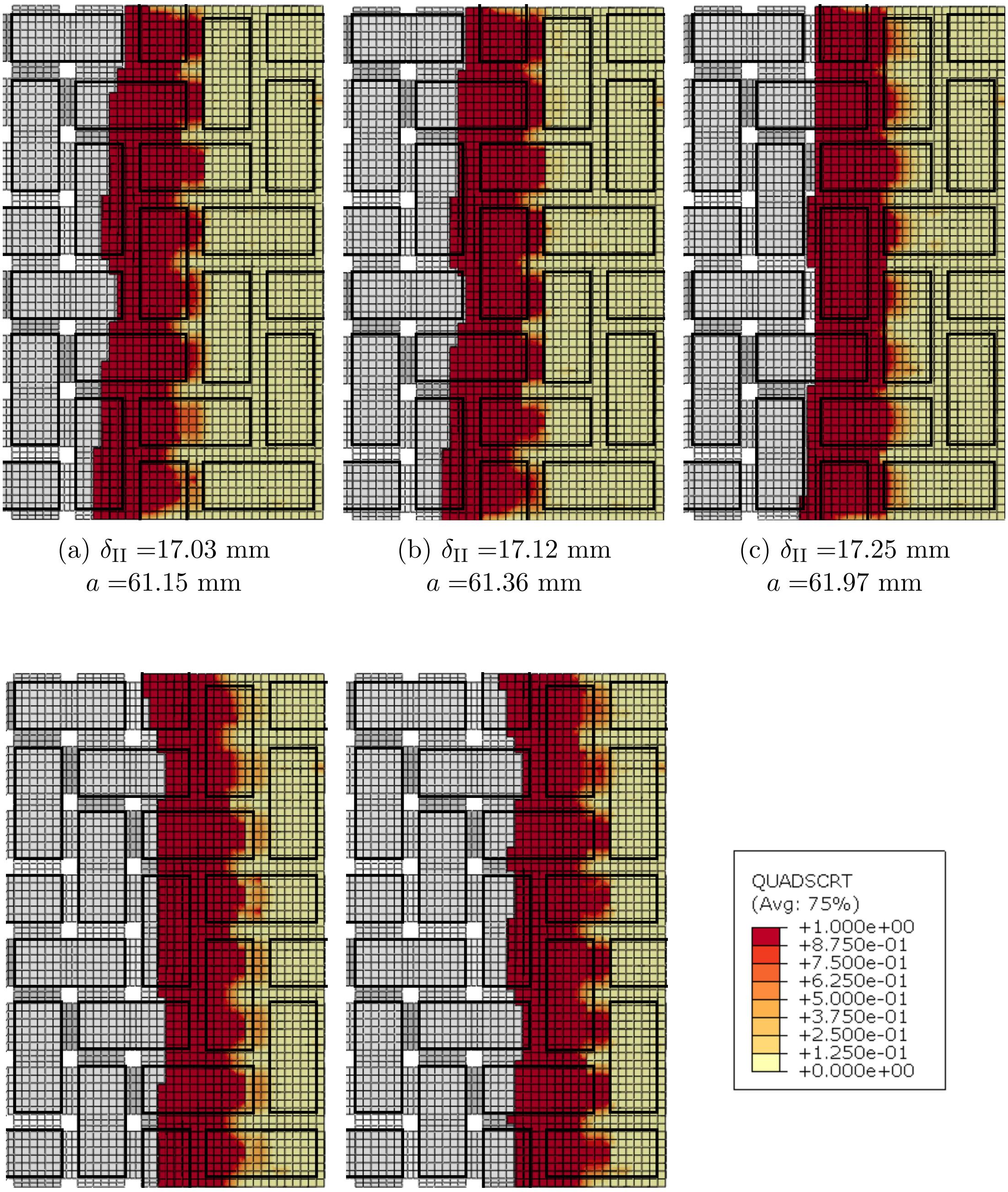

(a) δ_{II} =17.03 mm
a =61.15 mm

(b) δ_{II} =17.12 mm
a =61.36 mm

(c) δ_{II} =17.25 mm
a =61.97 mm

(d) δ_{II} =17.30 mm
a =62.99 mm

(e) δ_{II} =17.32 mm
a =63.49 mm

Figure 5.14: Delamination sequence during the ENF simulation in the interface of the EMB2 model. Horizontal sections of first layer's tows adjacent to the interface are illustrated with outlined rectangles. Figures are correlated with the annotations in Fig. 5.13

This results in small differences in separation at integration points, which still has a big influence on the damage initiation, where the maximum traction is reached at relative small separation due to high interface stiffness ($K = 10^5$), while the damage evolution takes place over a much larger values of separation. Thus, any differences in separation have a smaller effect on damage evolution compared to the effects on damage initiation.

The results from the Fig. 5.13 show that the crack is growing in steps. The annotation points (*c*) and (*e*) indicate the beginning and the end of a chosen crack jump. These points are represented by Fig. 5.14c and Fig. 5.14e, respectively. At Fig. 5.14c the crack front, in average, reaches the area of matrix pockets. At this stage the damage initiation is already at the beginning of the next consecutive area of tows. After this, the delamination process moves very quickly up to the point (*e*) (Fig. 5.14e). During this jump, the crack front moves through the interface at area of tows. The delamination process is slowed down again by the influence of matrix pockets, where the lack of the reinforcing phase results in more energy being transformed into elastically deforming the matrix. The process is being repeated throughout the interface.

The presence of the mode mix delamination in the interface of the EMB2 model is presented in Fig. 5.15, where the MMIXDMI and MMIXDME parameters are shown over the whole interface area at central displacement δ_{II} =17.32 mm. Similar as in the DCB simulation, the damage is initiated by both shear and opening mode of delamination at certain individual regions. These regions occur in the interface where tows in the direction of delamination onset change their level from the top to the bottom one (see the enlarged section in Fig. 5.15a) in both layers simultaneously, which creates a pattern of diagonally placed mix mode areas. The damage evolution in these same areas is also a result of mix mode delamination, where the MMIXDME parameter reaches values down to 0.75. This means roughly one quarter of the damage

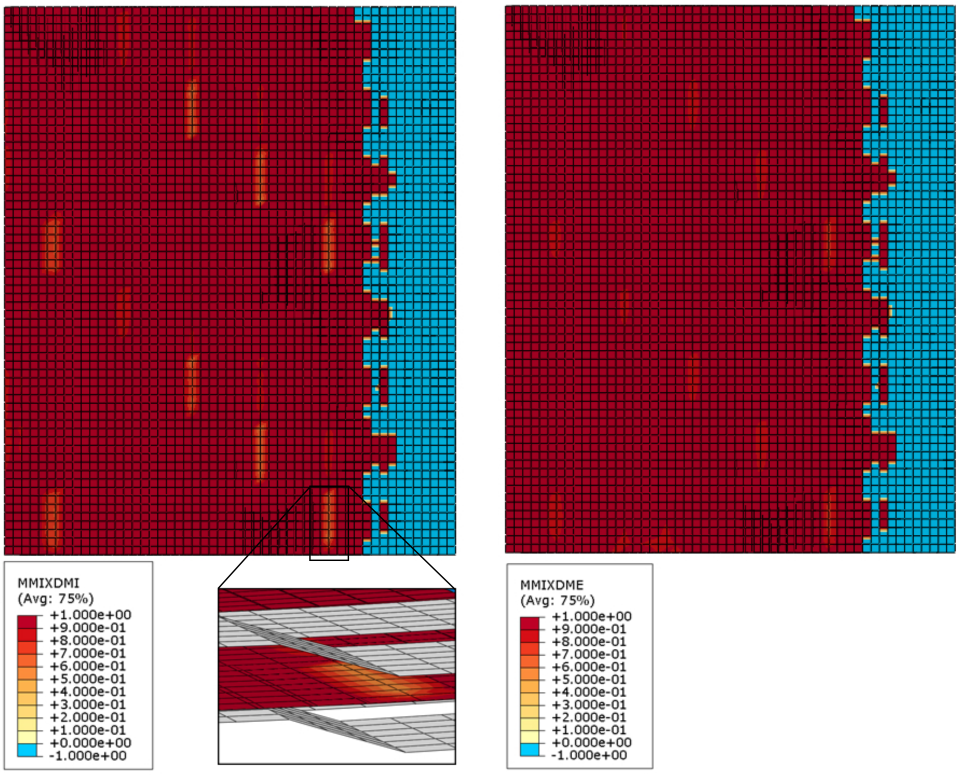
MMIXDMI
(Avg: 75%)
+1.000e+00
+9.000e-01
+8.000e-01
+7.000e-01
+6.000e-01
+5.000e-01
+4.000e-01
+3.000e-01
+2.000e-01
+1.000e-01
+0.000e+00
-1.000e+00
MMIXDME
(Avg: 75%)
+1.000e+00
+9.000e-01
+8.000e-01
+7.000e-01
+6.000e-01
+5.000e-01
+4.000e-01
+3.000e-01
+2.000e-01
+1.000e-01
+0.000e+00
-1.000e+00

(a) (b)

Figure 5.15: Mode mix ratio in the ENF simulation of the EMB2 model at δ_{II} =17.32 mm. Variables are set to -1 prior to damage initiation or evolution. The enlarged section shows a 3 dimension view with in-directional tows.

dissipation energy is contributed by mode I delamination in this particular regions. Note that in this case the mixed mode critical energy release rate is smaller compared to mode II. The effects these mix mode regions have on the delamination could explain the delamination front being slightly tilted. This can be seen from the sequence in Fig. 5.14, where the crack front, in average, propagates with a slight angle, that is changing throughout the process. Due to a lower value of critical energy release rate in regions with mix mode damage initiation, the crack front there propagates faster. Moreover, as the crack propagates in the interface, these mix mode regions are changing position relative to the crack front, which results in the changing angle of the crack front. However, in order to give a conclusive explanation, more simulations with different weaving patterns needs to be investigated.

5.2.1.2 EMB4 model

The Figure 5.16 shows a sequence of the damage process in the middle interface of the EMB4 model during the ENF simulation. The sub-figures are correlated to the annotation points in Fig. 5.13 for the EMB4 model.

Again, the effects of the surrounding in-directional tows on the middle interface are clearly visible from the shape of the damage initiation. Comparing to the EMB2 model, the pattern in the EMB4 model is more defined regarding to the in-directional tows. The EMB4 model has three cohesive interfaces with 4four textile plies (see Fig. 4.15). This means that the textile domain is twice as thick compared to the EMB2 mode. Consequently, the changes in the local stiffness surrounding the interface are slightly higher (compared to the EMB2 model), which results in a bigger difference between the damage initiation in the interface surrounded by in-directional tows, compared to the remaining areas.

On the right side of each sub-figure in Fig. 5.16 some damage is being initiated on a couple of integration nodes next to the edge of the textile domain. On this edge, all four ply layers of the textile domain are tied to the middle homogeneous section (see Fig. 4.16). The damage initiation at this edge is induced by the node-surface tie constraints. However, these integration points do not reach the maximum traction in either mode, which would result in stiffness degradation. This effect is fairly localized and small, therefore it does not have a big influence on the behaviour of the laminate or the interfaces in the textile domain. However, in order to quantify it, a longer textile domain should be used.

The crack front propagation, seen as the edge of the damage initiation area in Fig. 5.16, moves through the interface very similarly to the crack front in the EMB2 model. Annotation points (c) and (e) from Fig. 5.13 mark the crack jump, which can be seen as the crack length difference between the Fig. 5.16c and Fig. 5.16e. It indicates that the crack front propagation is govern by the same mechanisms described in the crack propagation of the EMB2 model. However, the crack propagation sequence takes place at a slightly lower values of central displacement, as seen from Fig. 5.13. The textile domain in the EMB4 model occupies more of the total laminate's thickness, compared to the EMB2 model, which results in bigger local stiffness differences between the area of matrix pockets and remaining more reinforced regions due to in-phase stacking of

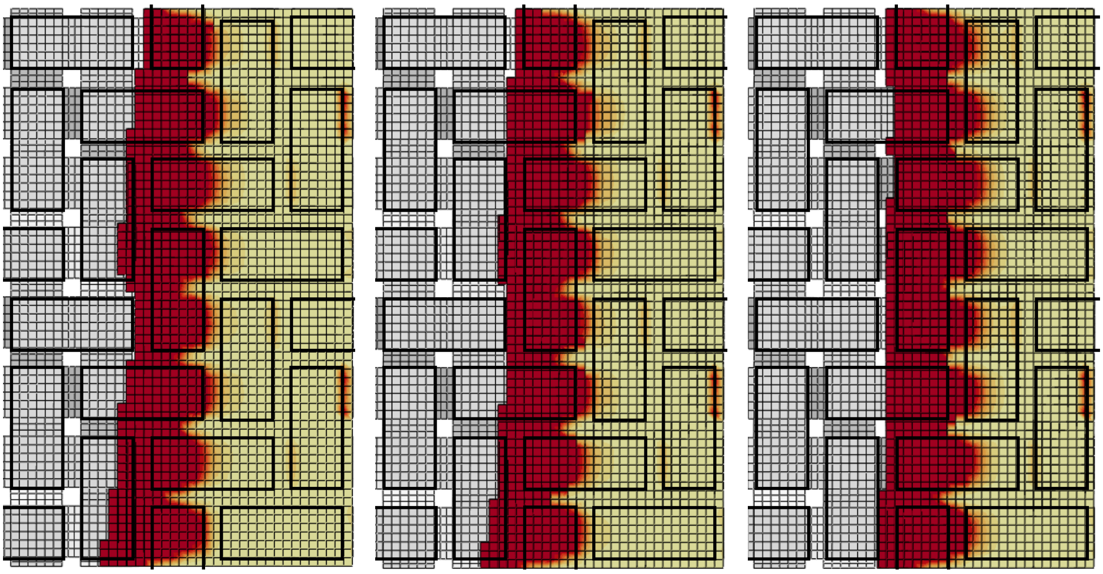

(a) δ_{II} =16.69 mm
a =61.43 mm

(b) δ_{II} =16.82 mm
a =61.64 mm

(c) δ_{II} =17.02 mm
a =62.12 mm

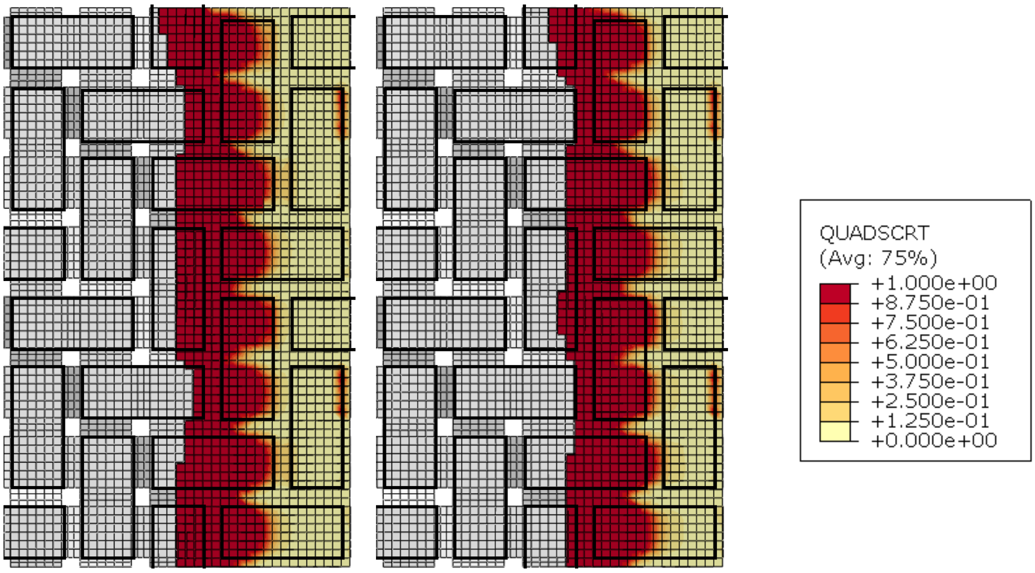

(d) δ_{II} =17.05 mm
a =63.32 mm

(e) δ_{II} =17.07 mm
a =63.85 mm

Figure 5.16: Delamination progress during the ENF simulation in the interface of the EMB4 model. Figures are correlated with the annotations in Fig. 5.13

the plies. Moreover, at the middle interface, the areas parallel to tows initiate damage quicker due to higher local stiffness compared to the EMB2 model at the same areas. In this case the same amount of energy in the interface, compared to EMB2 and reference model is locally reached at lower central displacements. As the crack propagates when a certain amount of energy is introduced locally (which is equal in all cases, i.e. $\mathcal{G} = \mathcal{G}_c$), the crack onset is predicted earlier in the case of the EMB4 model, because this certain amount of (local) energy is reached already at lower central displacements.

The EMB4 model has three individual cohesive interfaces in the textile domain. Figure 5.17 shows the damage process in both adjacent interfaces next to the middle one, where the crack propagates. From the damage initiation criterion in both interfaces (Fig. 5.17a and 5.17b) it can be seen that the damage initiates at certain areas, which corresponds to the location, where the in-direction tows change their level (in both the top and bottom adjacent ply layer relative to each interface). At the same location a small amount of damage evolution occurs, however the stiffness degradation remains small at these integration points. This means no crack opening or high damage in these interfaces are predicted. However, the EMB4 model predicts that interfaces adjacent to the middle one, where the initial crack lies, are effected by the delamination process which seems to be govern by the weaving pattern. Again, more simulations with different weaving patterns need to be conducted in order to investigate the correlation between the delamination in the middle interface and damage in adjacent interfaces.

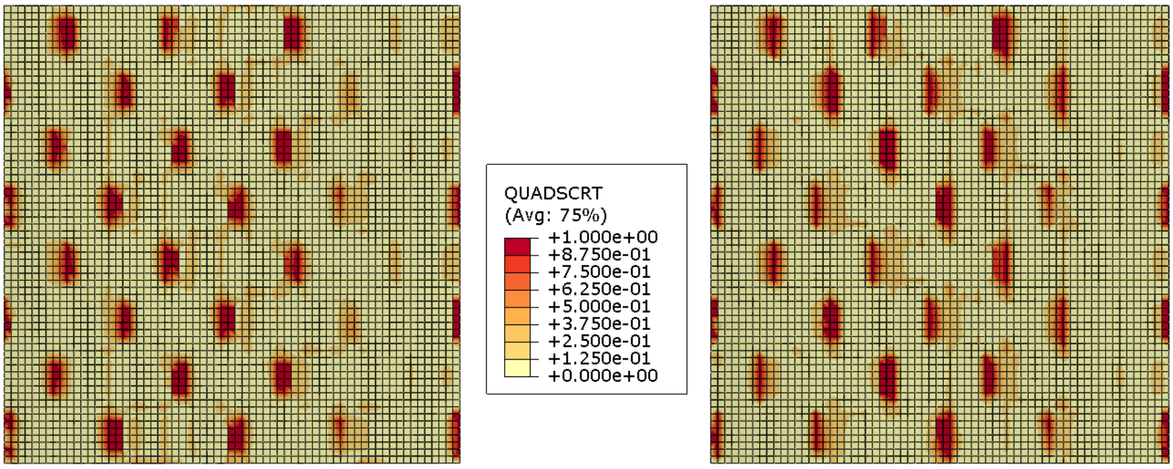

(a) Damage initiation in the bottom interface.

(b) Damage initiation in the top interface.

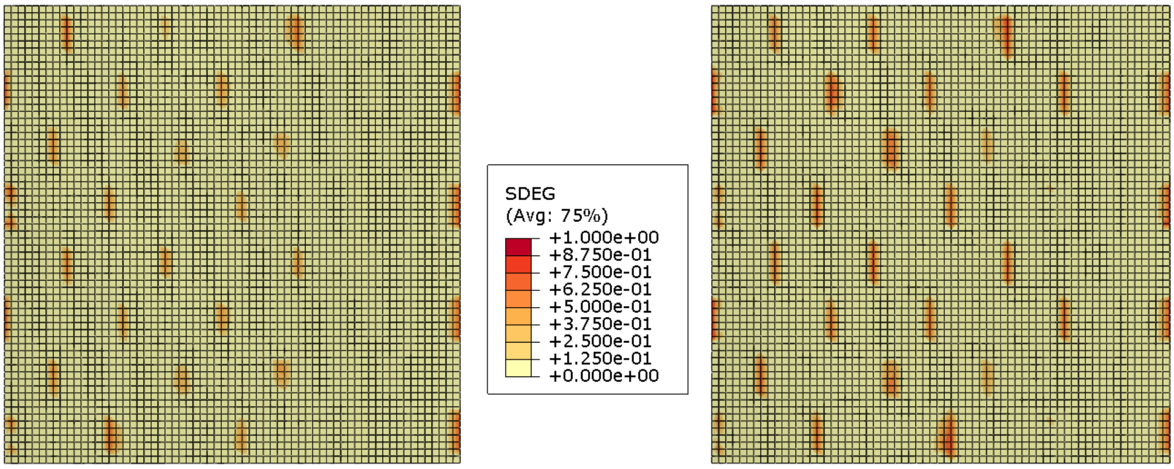

(c) Damage evolution in the bottom interface.

(d) Damage evolution in the top interface.

Figure 5.17: Damage initiation and evolution in the bottom and top interface at central displacement δ_{II} =17.07 mm of the EMB4 model.

5.2.2 Fracture Resistance Curve (R-Curve)

All three, the EMB2, EMB4 and the reference model, are compared in Fig. 5.18. Similar as with the DCB test, several evaluation methods are available, but for the purposes of this work the corrected beam theory approach is used for energy release rate evaluation. Again, the notations in this figure are correlated with the delamination process in Fig. 5.16. The comparison shows that the energy release rate from the EMB4 model is smaller during the whole process compared to the EMB2 and the reference model. The difference can be attributed to the fact that the EMB4 model predicts delamination onset at smaller central displacements, and thus smaller central reaction force (see Fig. 5.11 and Fig. 5.12) which, by the corrected beam theory, evaluates smaller energy release rate (see Eq. 2.19) compared to the EMB2 model. Note that the energy release rate in the middle interface still reaches the pre-set critical value but at lower central displacement compared to other models, which results in lower energy release rate (evaluated by CBT).

The same assumptions can be made for the varying of the energy release rate during the delamination progress over the area of tows (from point (c) to point (e)) and over the area of matrix pockets (from point (a) to point (c)) as in the case of the DCB simulation, where the evaluated energy release rate is influenced by the local mechanical properties of the textile domain.

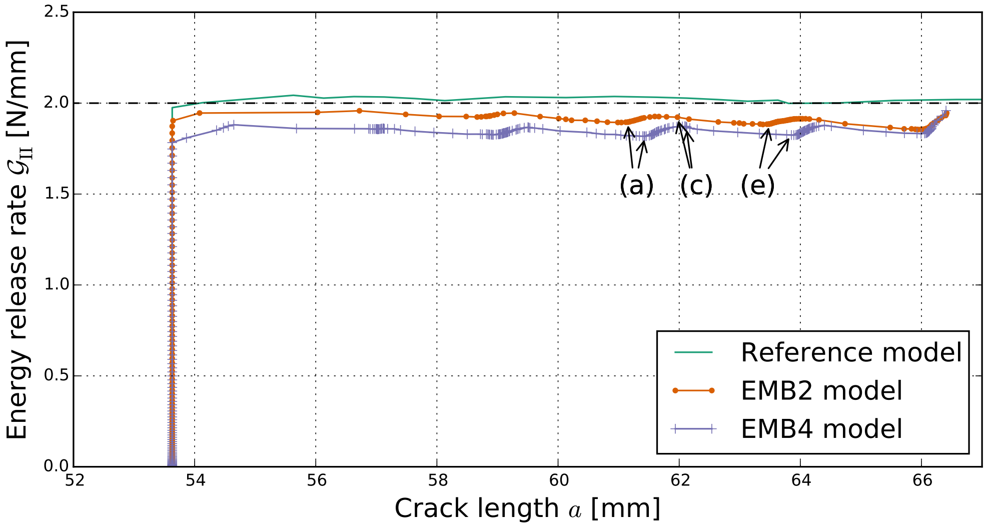

Figure 5.18: Fracture resistance curves (R-curves) for mode II delamination.

5.2.3 Energy Balance Analysis

The energy release rate from the numerical model can be obtained directly from the energy output variables in Abaqus, as discussed previous in the results of the DCB simulation.

Figure 5.19 shows the energy output variables in the EMB2 model relative to the central displacement and evaluated crack length. The viscous dissipation energy (U_v ; ALLCD) is significantly smaller compared to the strain energy, therefore the effect of viscous damping on the accuracy of the solution can be neglected.

The damage dissipation energy from Fig. 5.19b is compared to the dissipated energy evaluated with the corrected beam theory in Fig. 5.21. As expected from the results depicted in Fig. 5.18 the slope of the energy curve evaluated with the CBT is slightly lower that the direct damage dissipation energy output for the EMB2 model. The offset between the curves is caused by partly damaged nodes, which are not considered in the crack length evaluation in the CBT approach.

Figure 5.20 shows the energy balance in EMB4 model relative to the central displacement and evaluated crack length. Similar as with other models, the effects of viscous damping on the accuracy of the solution can be neglected due to small viscous dissipation energy in the model.

Figure 5.22 compares the damage dissipation energy from Fig. 5.20b to the dissipated energy evaluated with the CBT. The slope of the energy curve, which represents the energy release rate, evaluated with the CBT is slightly lower than the direct damage dissipation energy output for the EMB4 model due which corresponds to the R-curves in Fig. 5.18.

The energy release rate evaluated with the CBT from Fig. 5.18 predicts a lower energy release rate for the EMB4 model. Figure 5.23 compares the damage dissipation energy output and damage energy evaluated by the CBT between the EMB2 and EMB4 model. Similar to the R-curves, the damage dissipation energy for the whole EMB4 model is slightly smaller compared the the EMB2 model. Note that the damage dissipation energy is evaluated for the entire models, therefore in the case of the EMB4 model, for all three interfaces in the textile domain. As shown in Fig. 5.17, there is some dissipated energy from the top and bottom cohesive interface which contribute to the damage dissipation energy output in the EMB4 model. However, compared to the dissipated energy in the middle interface, these contributions are small, since the damage does not evolve severely. This is confirmed by comparing the dissipated energy (EMB4-ALLDMD in Fig. 5.23) with the black dashed line in Fig. 5.23, which represents the theoretical dissipated energy from the critical energy release rate for a single interface, as the measured dissipated energy is not significantly different from the theoretical one. Also the difference between the measured dissipated energy of the EMB2 and EMB4 model in Fig 5.23 indicates that the dissipated damage in the top and bottom interface is significantly small.

The comparison between the damage dissipation energies for both, the EMB2 and EMB4 models, shows the obtained results are in agreement with the difference in energy release rates from Fig. 5.18 which was already discussed previously.

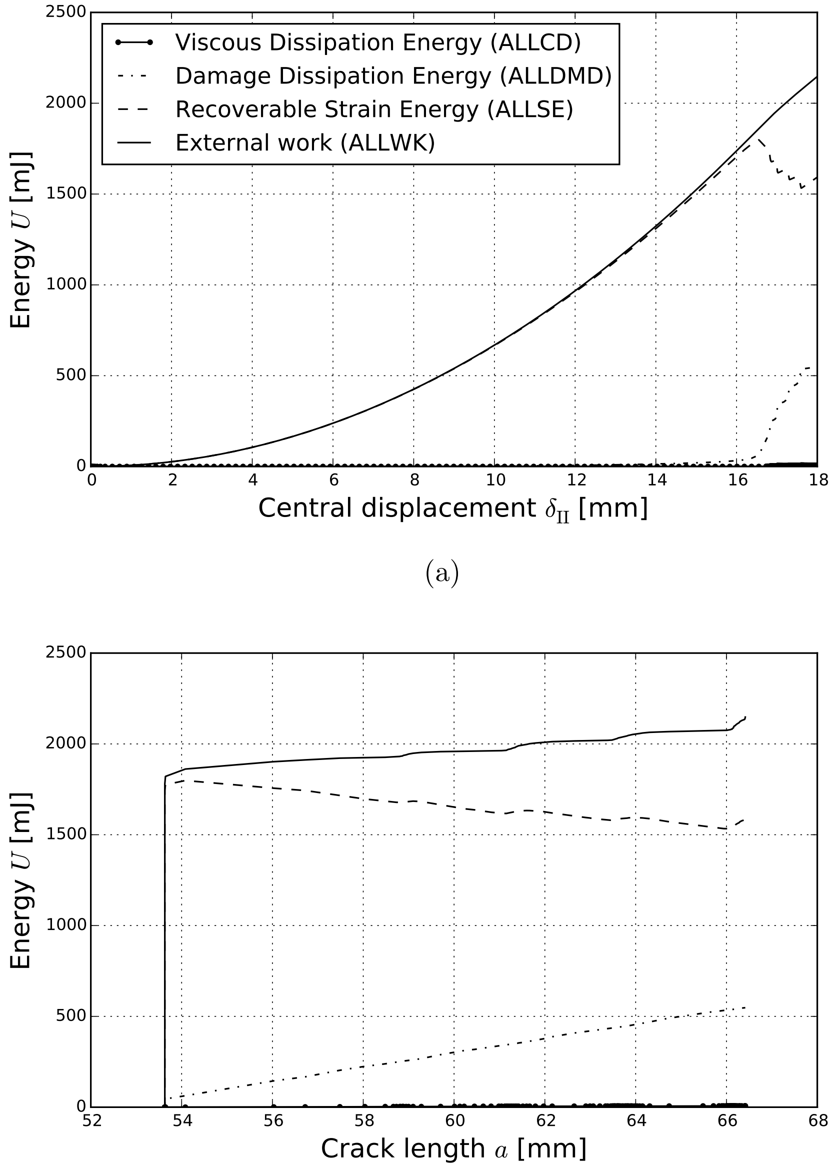

(a)

(b)

Figure 5.19: Energy balance of the EMB2 model during the mode II simulation. The top figure shows strain energy and dissipation energy distributions in relation to the central displacement. The bottom shows energies in relation to the crack length.

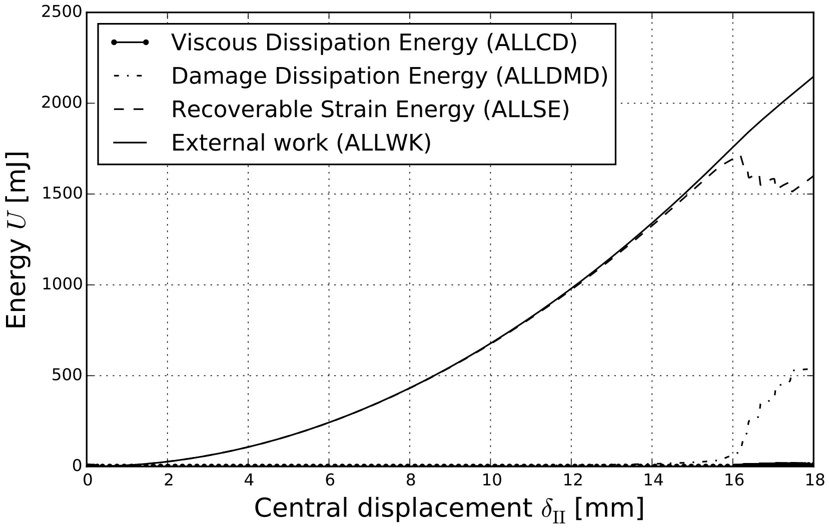

(a)

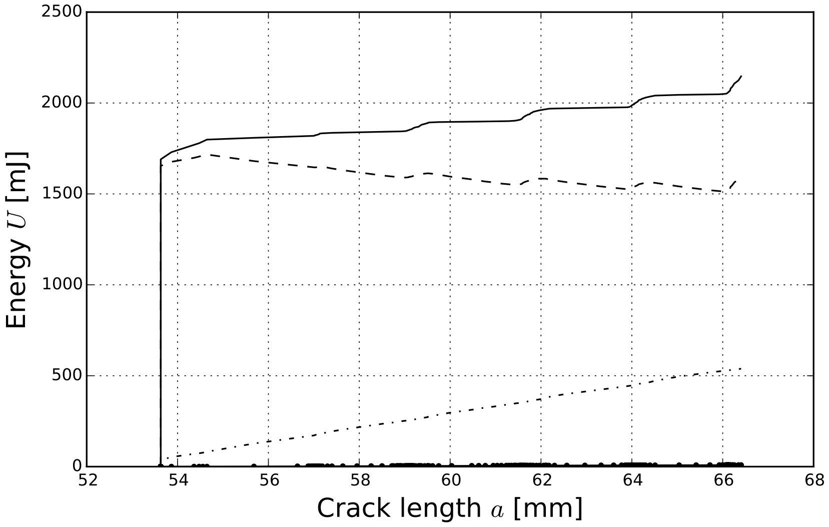

(b)

Figure 5.20: Energy balance of the EMB4 model during the mode II simulation. The top figure shows strain energy and dissipation energy distributions in relation to the tip displacement. The bottom shows energies in relation to the crack length.

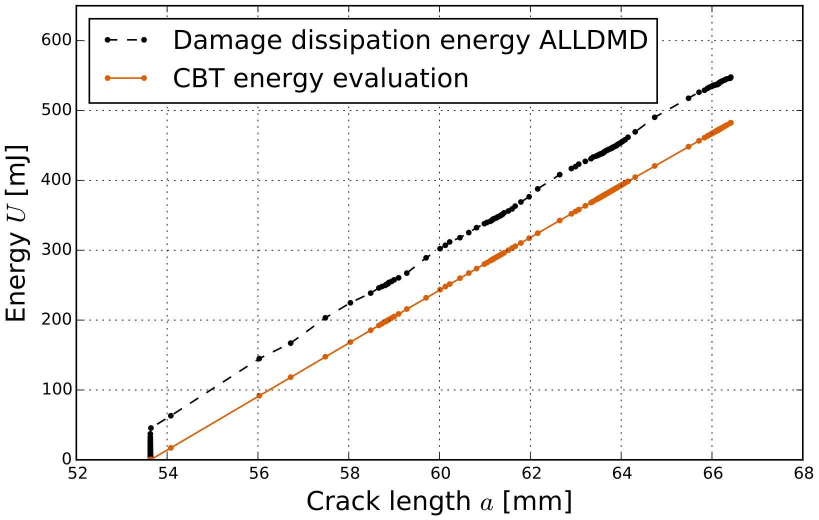

Figure 5.21: Comparison between the damage dissipation energy from the EMB2 model and the damage dissipation energy evaluated by corrected beam theory in the ENF simulation.

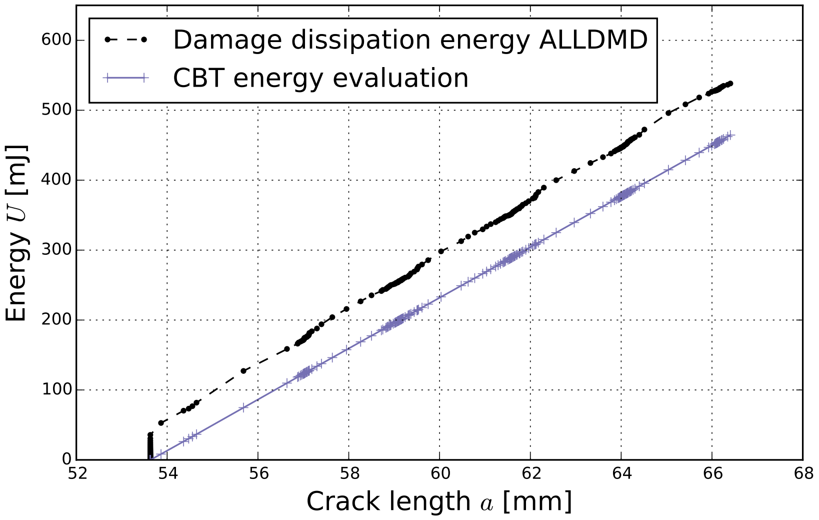

Figure 5.22: Comparison between the damage dissipation energy from the EMB4 model and the damage dissipation energy evaluated by corrected beam theory in the ENF simulation.

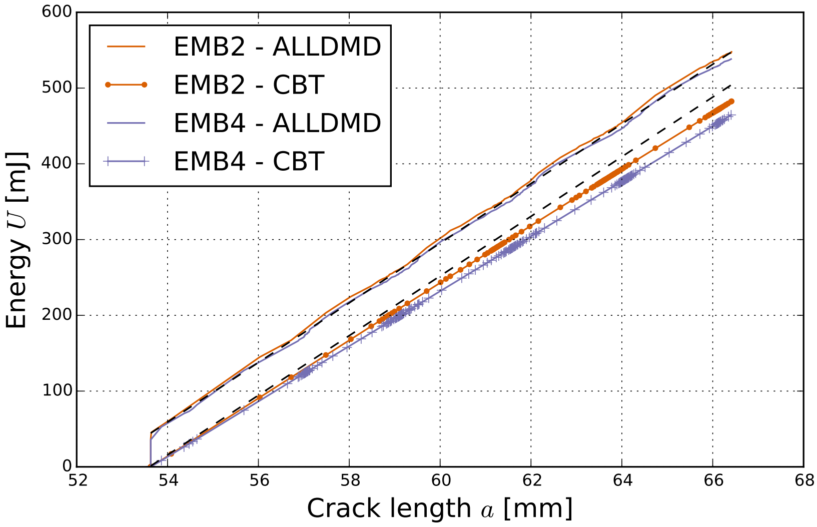

Figure 5.23: Comparison between the damage dissipation energy output variable and the dissipation energy evaluated with the CBT for the EMB2 and EMB4 model in the ENF simulation.

6 Conclusions

The main goal of the present work is the investigation of the delamination process in woven composites. For that reason, we presented efficient numerical models with an embedded domain of detailed textile structure.

Finite Element Method simulations predict the highly nonlinear load displacement curves while the overall delamination grow takes place. The predictions are in good agreement with the analytical solutions and the expected results. Exceeding the global response, local effects in the textile domain are taken into account and localized patterns of the various nonlinear mechanisms are predicted. The response is also evaluated in terms of dissipated energies attributed to these local mechanisms. This gave us a detailed insight into the global delamination behaviour as well as the locally involved mechanisms. Simulations predict that delamination is influenced by the topology of the composite structure and the variations in local stiffness and geometry effect the propagation of crack front in the interface.

An embedded approach enables us to run multi-scale simulations, which computational efforts can be processed by a standard desktop computer hardware. Double Cantilever Beam test and three point End Notch Flexure test, which are used to evaluate the two main modes of delamination, are simulated with this approach. Convergence challenges that come with such nonlinear simulations are resolved with viscous damping and other analysis controls, with negligible effects on accuracy of the solution which is promising for further line of work using these models.

The work done in this thesis proves that the unit cell approach, developed at the ILSB, is an efficient and powerful tool when it comes to simulations of delamination in laminated woven composites and shows great potential for further delamination investigation.

While the presented models gave very interesting results, they are still quite simplified regarding to the actual nature of such structures. Further work can be done in comparing different types of weaving patterns which, as shown in this work, have an impact on the local mechanisms during delamination. Additionally, damage modelling can be assigned to other constituents inside the textile domain, i.e. tows, matrix and inter-tow cohesive elements. Because of the weaving topology, the interfaces in reality do not have an uniform mechanical properties as the fibres run in different directions, thus here is a lot of room for further improvements which also bring new challenges in obtaining an efficient solutions.

Povzetek dela v slovenščini

Glavni cilj te magistrske naloge je podrobno raziskovanje delaminacijskega procesa v pletenih kompozitnih laminatih. V ta namen smo predstavili učinkovite numerične modele z integrirano domeno podrobne tekstilne stukture.

Simulacije z metodo končnih elementov napovejo močno nelinearen odziv laminata med delaminacijo. Rezultati simulacij zelo dobro ujamejo z analitičnimi izračuni na poenostavljenih modelih. Poleg globalnega odziva so upoštevani tudi lokalni efekti znotraj tekstilne domene, ki napovedo vzorce številnih lokaliziranih nelinearnih mehanizmov znotraj strukture. Odziv laminata je ovrednoten z vidika sproščanja energije med nastajanjem poškodbe oziroma delaminacije, del katere je tudi pripisan lokalnim mehanizmom. To nam omogoča podrobni vpogled tako v globalni odziv, kot v lokalne pojave med delaminacijo. Simulacije nakazujejo, da je rast razpoke med posameznimi plastmi laminata odvisna od topologije kompozitne strukture ter variacij v lokalni togosti in geometriji znotraj modela.

Pristop integriranja domen omogoča večstopenjske simulacije, ki pa so računsko še obvladljive s standardnimi namiznimi računalniki. Za namene te naloge sta simulirana standardizirana testa za dva različna načina delaminacije v laminatih z enosmernimi vlakni, i.e. test dvojno vpete konzole (Double Cantiliever Beam test) ter tritočkovni upogib nosilca (three point End Notch Flexure test). Konvergenčni izzivi, ki smo jih srečali v nelinearnih simulacah, rešujemo z uporabo viskoznega dušenja ter ostalih namenskih orodij. Njihov vpliv na točnost rezultatov pri tem ostaja minimalen, kar tudi potrjuje primernost predstavljenih numeričnih modelov za nadaljno uporabo na tem področju.

Pokazali smo, da uporaba integriranja osnovnih celic (t.i. Unit cell), ki so bile razvite na inštitutu za lahko-gradnjo in strukturno bio-mehaniko oziroma ILSB na dunajski tehnični univerzi, predstavlja učinkovit način raziskovanja delaminacij v laminatih ter kaže velik potencial za nadaljno delo na področju simulacij delaminacij v kompleksnih strukturah (kot so pleteni kompozitni laminati).

Za podrobnejšo analizo vpliva topologije na delaminacijo bi bilo potrebno izvesti simulacije modelov z različnimi vzorci pletenja ojačitvene faze kompozita (npr. ogljikovih vlaken). Naslednji korak je v vključevanju poškodbenih mehanizmov v ostalih sestavnih delih tekstilne domene, kot so matrica, snopi ojačitvenih vlaken ter kohezivni elementi med njimi. Veliko prostora za izboljšave je tudi v samem sloju med plastmi laminata. Snopi vlaken, ki so različno usmerjena zaradi pletene topologije, imajo vpliv na mehanske lastnostni v kohezivnem sloju in bi bilo potrebno določiti lastnosti le tega glede na vzorec pletenja. Poleg dodatnih, podrobnih opisov mehanskega odziva, vsaka nadgradnja modelov prinaša nove izive v zagotovitvi časovno učinkovite numerične rešitve.

7 Bibliography

[1] "Composites in Airbus." `https://www.airbusgroup.com/dam/assets/airbusgroup/int/en/investor-relations/documents/2008/presentations/GIF2008/gif2008_workshop_composites_hellard.pdf`. viewed: November 2016.

[2] S. Hashemi, A. Kinloch, and J. Williams, "The analysis of interlaminar fracture in uniaxial fibre-polymer composites," *Proceedings of the Royal Society of London. Series A*, vol. 427, pp. 173–199, 1990.

[3] G. B. Murri, "Effect of Data Reduction and Fiber-Bridging on Mode I Delamination Characterization of Unidirectional Composites." `http://ntrs.nasa.gov/archive/nasa/casi.ntrs.nasa.gov/20110015832.pdf`. viewed: September 2016.

[4] T. K. O'Brien, W. M. Johnston, and G. J. Toland, "Mode II Interlaminar Fracture Toughness and Fatigue Characterization of a Graphite Epoxy Composite Material ." `http://ntrs.nasa.gov/archive/nasa/casi.ntrs.nasa.gov/20100031113.pdf`. viewed: September 2016.

[5] P. W. Harper and S. R. Hallet, "Cohesive zone length in numerical simulations of composite delamination," *Engineering Fracture Mechanics*, vol. 75, pp. 4774–4792, 2008.

[6] J. A. Nairn, "Analytical and Numerical modeling of R Curves for Cracks with Bridging Zones," *International Journal of Fracture*, vol. 5, no. 2, pp. 167–181, 2009.

[7] E. Barbero, P. Lonetti, and K. Sikkil, "Finite element continuum damage modeling of plain weave reinforced composites," *Composites: Part B*, vol. 37, pp. 137–47, 2006.

[8] J. Gager and H. Pettermann, "Numerical homogenization of textile composites based on shell element discretization," *Composites Science and Technology*, vol. 72, pp. 806–812, 2012.

[9] P. Camanho, C. Davila, and M. D. Moura, "Numerical Simulation of Mixed-mode Progressive Delamination in Composite Materials," *Journal of COMPOSITE MATERIALS*, vol. 37, no. 16, pp. 1415–1438, 2003.

[10] M. F. de Moura, "Interlaminar Mode II Fracture Characterization." Faculdade de Engenharia da Universidade do Porto, Portugal. Available at: `http://paginas.fe.up.pt/~mfmoura/Livro2.pdf`. viewed: 18. 4. 2016.

[11] M. Moslemi and M. Khoshravan, "Cohesive Zone Parameters Selection for Mode-I Prediction of Interfacial Delamination," *Journal of Mechanical Engineering*, vol. 61, no. 9, pp. 507–516, 2015.

[12] Jang-Kyo Kim and Man-Lung Sham, "Impact and delamination failure of woven-fabric composites," *Composite Science and Technology*, vol. 60, pp. 745–761, 2000.

[13] R. M. Jones, *Mechanics of Composite Materials, Second Edition.* Philadelphia, PA, USA: Taylor & Francis Inc., 1999.

[14] J. Williams *International Journal of Fracture*, vol. 36, pp. 101–119, 1988.

[15] S. Hashemi, A. Kinloch, and J. Williams *Journal of Materials Science*, vol. 8, pp. 125–129, 1989.

[16] H. Hadavinia and H. Ghasemnejed, "Effects of Mode-I and Mode-II interlaminar fracture toughness on the energy absorption of CFRP twill/weave composite box sections," *Composite Structures*, vol. 89, pp. 303–314, 2009.

[17] W. Bascom, J. Bitner, R. Moulton, and A. Siebert, "The interlaminar fracture of organic-matrix, woven reinforcement composites," *Composites*, vol. 11, no. 1, pp. 9–18, 1980.

[18] DIN EN 6033:2016-02, "Aerospace series - Carbon fibre reinforced plastics - Test method - Determination of interlaminar fracture toughness energy - Mode II - G_{IC}."

[19] DIN EN 6034:2013-07, "Aerospace series - Carbon fibre reinforced plastics - Test method - Determination of interlaminar fracture toughness energy - Mode II -."

[20] E. Rybicki and M. Kanninen, "A Finite Element Calculation of Stress Intensity Factors by a Modified Crack Closure Integral," *Engineering Fracture Mechanics*, vol. 9, pp. 931–938, 1977.

[21] "Abaqus 6.14 documentation." `https://www.ilsb.tuwien.ac.at/v6.14`. viewed: March - August 2016.

[22] A. Turon, P. Camanho, J. Costa, and J. Renart, "Accurate simulation of delamination growth under mixed-mode loading using cohesive elements: Definition of interlaminar strengths and elastic stiffness," *Composite Structures*, vol. 92, pp. 1857–1864, 2010.

[23] M. Benzeggagh and M. Kenane, "Measurement of Mixed-Mode Delamination Fracture Toughness of Unidirectional Glass/Epoxy Composites with Mixed-Mode Bending Apparatus," *Composites Science and Technology*, vol. 56, pp. 439–449, 1968.

[24] A. Arrese, N. Carbajal, G. Vargas, and F. Mujika, "A new method for determining mode II R-curve by the End-Notched Flexure test," *Engineering Fracture Mechanics*, vol. 77, pp. 51–70, 2010.

[25] V. A. Franklin and T. Christopher, "Generation and Validation of Crack Growth Resistance Curve from DCB Specimens: An Experimental Study," *Strength of Materials*, vol. 45, no. 6, pp. 674–683, 2013.

[26] R. Gutkin, M. Laffan, S. Pinho, P. Robinson, and P. Curtis, "Modelling the R-curve effect and its specimen-dependence," *International Journal of Solids and Structures*, vol. 48, pp. 1767–1777, 2011.

[27] B. N. Rao and A. Acharya, "Evalution of Fracture Energy G_{IC} using a double cantilever beam fibre composite study," *Engineering Fracture Mechanics*, vol. 51, pp. 317–322, 1995.

[28] G. R. Irwin, *Encyclopedia of Physics (Handbuch der Physic)*, vol. VI, ch. Fracture, pp. 551–590. Springer Verlag, 1958.

[29] A. C. Fischer-Cripps, *Introduction to Contact Mechanics*, ch. Linear Elastic Fracture Mechanics, pp. 31–48. Springer, 2007.

[30] J. R. Reeder, K. Demarco, and K. S. Whitley, "The use of doubler reinforcement in delamination toughness testing," *Composites: Part A*, vol. 35, pp. 1337–1344, 2004.

[31] L. Carlsson, J. Gillespie, and R. Pipes, "On the analysis and design of the end notched flexure (ENF) specimen for mode II testing," *Journal of Composite Materials*, vol. 20, pp. 594–604, 1986.

[32] P. Davies, P. Casari, and L. Carlsson, "Influence of fibre volume fraction on mode II interlaminar fracture toughness of glass/epoxy using the 4ENF specimen," *Composites Science Technology*, vol. 65, pp. 295–300, 2005.

[33] G. Barenblatt, "Mathematical Theory of Equilibrium Cracks in Brittle Failure," *Advances in Applied Mechanics*, vol. 7, 1968.

[34] D. Dudgale, "Yielding of Steel Sheets Containing Slits," *Journal of Mechanics and Physics of Solids*, vol. 8, pp. 100–104, 1960.

[35] V. A. Franklin and T. Christopher, "Fracture energy estimation of DCB specimens made of glass/epoxy: an experimental study," *Advances in Materials Science and Engineering*, pp. 1–7, 2013.

8 Annex A

8.1 Energy Release Rate $\mathcal{G}_{\mathrm{I}}$ Evaluation

As already mentioned in the introduction chapter, there are several proposes on how to evaluate energy release rate during delamination of laminates. Here is a brief overview of the most common ones:

- With measurement of reaction force, tip displacement and crack length for each increment of the simulation we can easily find the energy release rate with corrected beam theory (see Eq. (2.15)).
- The generalized Irwin-Kies equation for strain energy release rate of DCB specimen is given by [25]:

  $$\mathcal{G} = \frac{P^2}{2B}\frac{\partial C}{\partial a} \tag{8.1}$$

  Considering the root rotation, the compliance C is also given by [27]:

  $$C = \frac{\delta}{P} = \frac{2\,a^3}{3\,E_{11}\,I_a} + \frac{2}{K_{\mathrm{I}}}\,a^2. \tag{8.2}$$

  Eliminating K in Eq. (8.2), the fracture toughness can be evaluated from the simulation data as [35]:

  $$\mathcal{G}_{\mathrm{I_c}} = \frac{P^2\,a^2}{3\,B\,E_{11}\,I_a} + \frac{P\,\delta}{B\,a} \tag{8.3}$$

  .
- The author from [6] proposes a revised area method which is shown on Figure 8.1A. The procedure is as follows:
  1. Measure force and crack length as a function of load-point displacement - $P(\delta)$ and $a(\delta)$.
  2. Cumulative released energy per unit thickness (”Cumulative Area” in Fig. 8.1A) can be found by following equation:

     $$U(\delta) = \frac{1}{B}\left(\int_0^{\delta} P(x)\,dx - \frac{\delta}{2}P(\delta)\right) \tag{8.4}$$

3. Cumulative energy $U(\delta)$ can be replotted as a function of crack length $U(a)$ by combining $U(\delta)$ and $a(\delta)$ as parametric functions. See the Fig. 8.1B.
4. By energy analysis, R is the first derivative (slope) of $U(a)$ therefore $R = U'(a)$. The slope calculation my benefit from smoothing by spline fits of running-regression methods.

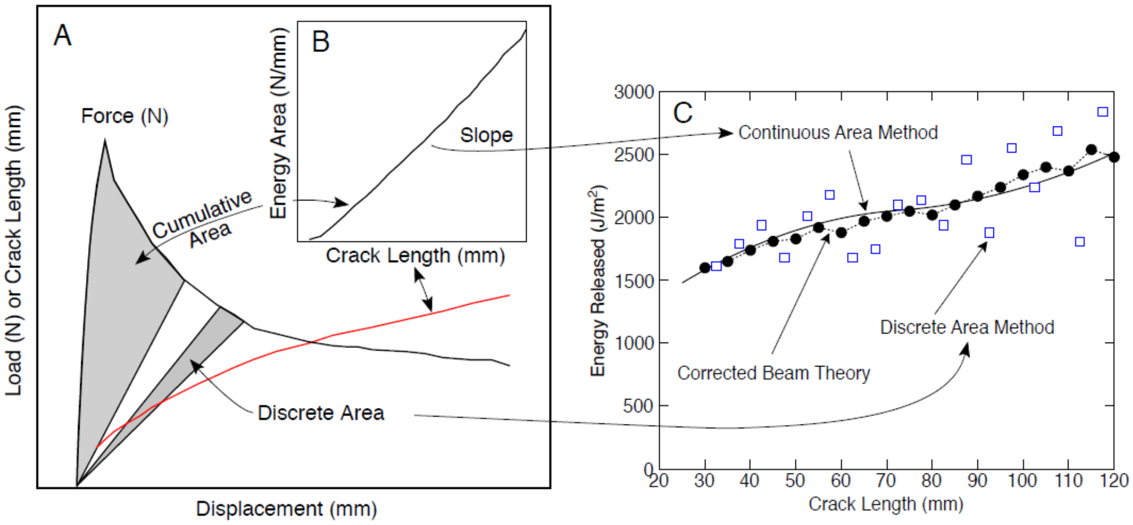

Figure 8.1: Continuous area method for crack growth fracture curve [6]

All of the above described methods are compared in Fig. 8.2 for the DCB simulation of the EMB2 model, where the energy release rate varies during the delamination. Discrete area approach requires subtraction of nearly equal values, which makes this method unreliable. The proposed revised method, i.e. Continuous area method, gives better results but it is heavly influenced by the smoothing of the spline. Also it does not represent any measuring data points but instead gives only an approximation of the values. Energy evaluation with corrected beam theory and generalized Iwrin-Kies approach shows more promising results, that can be used to investigate delamination process in a woven laminate. For the purposed of this work the corrected beam theory approach is used. More is disscued in Chapter 2.

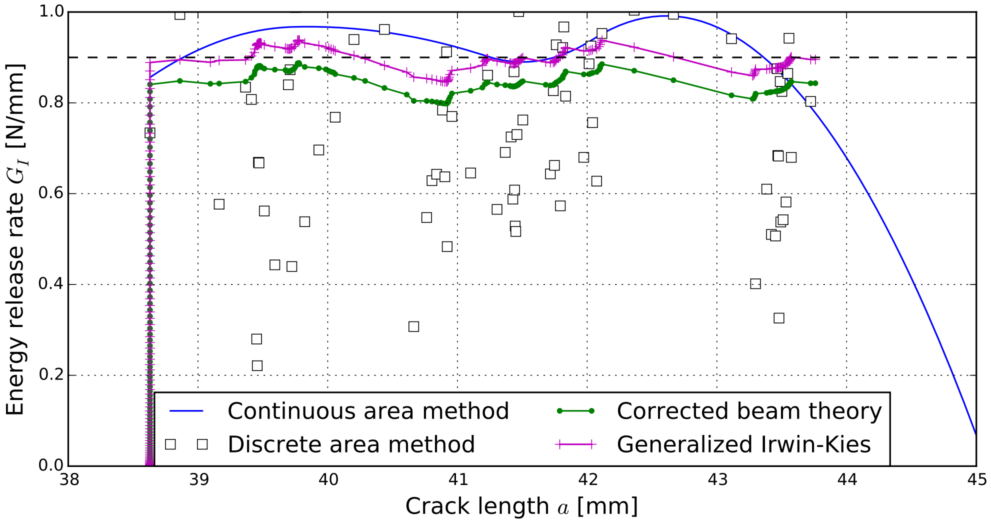

Figure 8.2: Comparison of energy release rate evaluation approaches for mode I of model with a 2 layer embedded domain.